Nano Semiconductor Hybrid Materials for Energy and Environmental Applications

Thesis submitted
to the University of Calicut for the
award of

DOCTOR OF PHILOSOPHY IN CHEMISTRY

JITHESH K.

DEPARTMENT OF CHEMISTRY
UNIVERSITY OF CALICUT
KERALA- 673635
INDIA
NOVEMBER-2019

CERTIFICATE

This is to certify that the thesis entitled **"Nano Semiconductor Hybrid Materials for Energy and Environmental Applications"** submitted by Mr. Jithesh K to the University of Calicut for the award for the degree of Doctor of Philosophy in Chemistry, is a record of precise research work carried out at the Department of Chemistry, University of Calicut under my guidance and supervision. The contents of the thesis have been checked for plagiarism using the software 'Urkund' and similarity index falls under permissible limit. I further certify that the thesis or part has not previously formed the basis for the award of any degree, diploma or associateship of any other university or institute.

Calicut University **Dr. Pradeepan Periyat**

November-2019

DECLARATION

I hereby declare that the matter embodied in the thesis is the result of studies carried out by me at the Department of Chemistry, University of Calicut, under the supervision of Dr. PradeepanPeriyat, Assistant Professor, Department of Chemistry, University of Calicut and the same has not previously formed the basis for the award of any degree or diploma. Whenever the work described or cited is based on the findings of other researchers, due acknowledgement is made in keeping with the general practice of reporting scientific observations.

Calicut University
November-2019

Jithesh. K

ACKNOWLEDGEMENT

First of all, I would like to sincerely thank Dr. Pradeepan Periyat, my thesis supervisor, for suggesting the research problem and for his guidance, support, encouragement and help throughout my research career which lead to the successful completion of this work.

I would like to thank Dr. Yahya A Ismail (Head, Department of Chemistry), Dr. P. Raveendran, Dr. K. Muraleedharan and Dr. V. M. Abdul Mujeeb (former Head, Department of Chemistry) for providing me the necessary facilities to carry out this research work. I also thank all other faculty members, non-teaching staffs, technical assistant and librarian of the Department of Chemistry for their timely help and support.

I sincerely thank Dr. R. B. Rakhi, DST-Ramanujan Fellow, CSTD, NIIST (CSIR) and her research students Mrs. Anjana and Mr. Manu for the collaborative work on electrochemical characterization of supercapacitor devices. I extend my thanks to Dr. Shahin Thayyil, Department of Physics, Calicut University and his research scholar Mrs. Shabeeba for their collaboration in supercapacitor research.

I am thankful to Central Sophisticated Instrument Facility (CSIF), Department of Nanotechnology, Department of Physics of University of Calicut and Sophisticated Test and Instrumentation Centre, CUSAT for material characterization. I gratefully acknowledge Faculty Development Programme of UGC, Govt. of India for the financial support.

I thank Dr. Govindraj, Dr. Ratheesh Krishnan, Dr. M. V. Vinayak, Dr. Biju francis, Dr. C. R. Sinu, Dr. G. Kalaprasad for their guidance, help and support throughout my research career.

I am thankful to Dr. V. Kumar, Dr. P. A. Joy, Dr. S. N. Potty, Dr. Jose James (late), Dr. M. T. Sebastian, Dr. Baiju Vijayan, Dr. K. G. Nishanth. Mr. C. Chandrakanth and Mr. Pakia Selvam for being a source of inspiration and motivation.

I am happy to acknowledge Dr. Sivadasan Thirumangalath (Principal, Sree Narayana College, Kannur), faculty members of the Department of Chemistry and all other faculty members of SN College Kannur for their encouragement and support.

Many thanks and gratitudes to my research group colleagues Dr. Sanjay, Dr. Binu noufal, Dr. Shahnas, Dr. Jijil, Mr. Dinesh, Ms. Anjitha and a special thanks to Mr. Deepak for designing my thesis cover page. With a great appreciation I would like to acknowledge all the research scholars of the Chemistry Department for their help and support.

I owe a lot to my family members and friends who encouraged and helped me at every stage of my personal and academic life, and longed to see this achievement come true.

Jithesh Kavil

CONTENTS

Abstract

The field of nano hybrid materials has witnessed an exponential development due to the demand for functional materials, especially in the field of energy storage and environmental remediation. Hybrid materials are combination of two or more materials, assembled in such a way as to have attributes not offered by the individual material alone.

In the present thesis graphitic carbon nitride (g-C_3N_4), titanium dioxide (TiO_2) and iron oxide (Fe_2O_3) based nano hybrid structures were explored. These materials have been investigated in energy storage applications and/or environmental remediation process.

In Chapter 3, a series of hybrid material from g-C_3N_4 and TiO_2 nanotubes were prepared *via* hydrothermal method by adding different weight percentage of TiO_2 nanotubes in g-C_3N_4 matrix by keeping g-C_3N_4/ TiO_2 ratio as 1:0, 1:1, 1:2 and 1:4. These nanohybrid systems were employed for the fabrication of symmetric supercapacitor devices and the results were compared with the individual component. The composite electrode material with g-C_3N_4/TiO_2 ratio 1:4 exhibited a remarkable increase in specific capacitance; which is attributed to the increase in surface area of the composite due to the spacer effect of one dimensional TiO_2 in the two dimensional network of g-C_3N_4.

In Chapter 4, pseudocapacitive transition metal oxides such as MnO_2 and SnO_2 were separately grown on the two dimensional network of g-C_3N_4 in an attempt to fabricate g-C_3N_4/MnO_2 and g-C_3N_4/SnO_2 nanohybrid structures. The materials were employed as supercapacitor

electrodes in symmetric two electrode configurations and the results were compared with the bare g-C_3N_4 electrodes. A remarkable increase in specific capacitance was obtained for g-C_3N_4/MnO_2 electrode (174 Fg^{-1}) than that of g-C_3N_4/SnO_2 (64 Fg^{-1}) and g-C_3N_4 (50 Fg^{-1}). The improvement in the electrochemical performance of g-C_3N_4/MnO_2 electrode can be attributed to the increase in surface area and the pseudocapacitive contribution from MnO_2 nanoflakes.

In Chapter 5, Metal oxide dispersed graphitic carbon nitride hybrid nanocomposites (g-C_3N_4/CuO and g-C_3N_4/Co_3O_4) were prepared via direct precipitation method. The materials were used as electrode material in symmetric supercapacitors. The g-C_3N_4/Co_3O_4 electrode based device exhibited a specific capacitance of 201 Fg^{-1} which is substantially higher than g-C_3N_4/CuO (95 Fg^{-1}) and bare g-C_3N_4 electrodes (72 Fg^{-1}). At a constant power density of 1 $kWkg^{-1}$, the energy density given by g-C_3N_4/Co_3O_4 and g-C_3N_4/CuO devices is 27.9 $Whkg^{-1}$ and 13.2 $Whkg^{-1}$ respectively. The enhancement of electrochemical performance in hybrid material is attributed to the pseudo capacitive nature of the metal oxide nanoparticles incorporated in g-C_3N_4 matrix.

In Chapter 6, a multifunctional nano hybrid material; Fe_2O_3@carbon nano structures were prepared from discarded razor blades and glucose solution *via* hydrothermal method. The main objective of the work is based on the concept of 'regenerative economy' with an aim to minimize the environmental pollution and depletion of the resources by Reducing Reusing and Recycling (3R) of the waste material. The energy storage and environmental applications of the hybrid material

was studied by successfully employing it as an electrode in symmetrical supercapacitor devices and also as adsorbent material for the removal oil-spill from water. At a constant current density of 1 Ag^{-1}; the Fe_2O_3@carbon samples exhibit a highest specific capacitance of 285. 6 Fg^{-1} which is almost two-fold the specific capacitance of the as-synthesized Fe_2O_3 sample (122.7 Fg^{-1}).

The final part of the thesis was based on the environmental objective of the research work, in which cadmium sulphide (CdS) sensitized TiO_2 nano hybrid materials were fabricated *via* simple hydrothermal route. Different weight percentage (0, 1, 5 and 10) of CdS nano particles was introduced into the TiO_2 system inorder to enhance the visible light absorption capability of TiO_2. The photocatalytic activity of the composite samples was compared with bare TiO_2 and CdS. Among the synthesized catalyst materials, TiO_2 loaded with 10 weight percentage of CdS (TiO_2-CdS10) have shown excellent photocatalytic activity for the degradation of methyl orange dye. The degradation rate of the active material was found to be $2.8x10^{-2}$ min^{-1} which is about 3.5 times faster than the rate of bare TiO_2 catalyst. The BET studies and the photoluminescence (PL) studies indicated that the enhancement in photocatalytic activity exhibited by TiO_2-CdS10 can be attributed to the high surface area and the effective charge separation possessed by the composite sample.

Chapter One

Introduction

Contents

Population explosion and industrial growth have created serious implications on the energy crisis and pollution of the ecosystem. Clean energy technology and a clean environment are inevitable for the sustainable development of the society. During the last few decades researchers and policy makers were searching for functional materials that can be used for renewable energy conversion, energy storage and environmental remediation. Nano-semiconductor hybrid materials have been received a great deal of attention as they can be used for both energy storage and environmental applications, owing to its better charge carrier mobility and visible light driven photocatalytic activity. The present thesis embodies our attempt to develop various nano-semiconductor hybrid materials *via* chemical processing route for energy and environmental applications. Graphitic carbon nitride (g-C_3N_4), an organic semiconductor based nano-heterostructures were employed as supercapacitor electrodes for energy storage application and titanium dioxide (TiO_2), an inorganic semiconductor based

nanostructures were used as visible light driven photocatalyst for the removal of dissolved organic impurities from water. Energy storage and environmental remediation applications of Fe_2O_3@Carbon, which was derived from discarded razor blades, were also investigated as a part of the research work.

1. 1. Renewable Energy Storage

Carbon emission has been a serious environmental issue and world economy demands the need of a clean and inexhaustible renewable energy technology as the future energy source.[1,2] Majority of the energy resources of the world are non-renewable fossil fuels and more than 80 % of India's power comes from fossil fuels and nuclear energy **(Figure 1. 1 & 1. 2a)**. Therefore we need a pivotal approach to make sure that we reduce our carbon foot print by embracing advances in the technology.[3] India's renewable energy sector is developing at faster rate and our renewable energy goal is to generate 175 GW energy from renewable sources by 2022 which is 55 % higher than the currently installed projects of 60 GW **(Figure 1. 2b)**.[4]

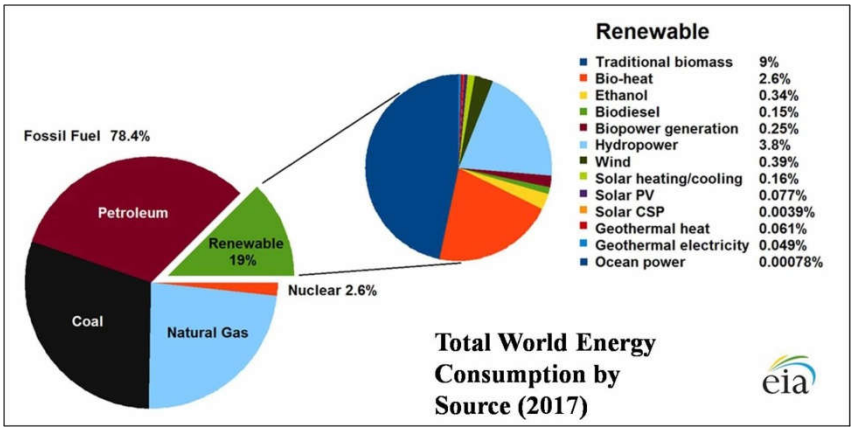

Figure 1. 1. Graphical representation of the world energy consumption by source.[5]

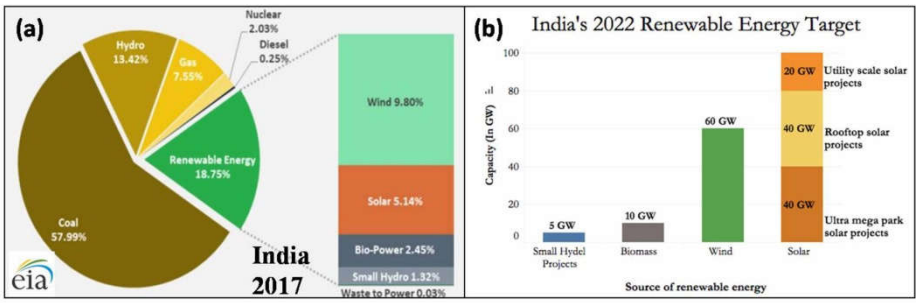

Figure 1. 2. Graphical representation of (a) India's energy consumption by source, (b) India's renewable energy goal.[5]

Renewable energy technologies such as photovoltaics, wind turbines, *etc*. are highly effective green approaches for sustainable energy development. However the storage of this generated spasmodic energy and their release upon demand is a bottleneck in renewable energy management.[6,7]

Currently lithium ion batteries emerged as a reliable rechargeable energy storage technology due to its high electrochemical performance and theoretically high energy density.[8] Lithium batteries have been used as a power source in personal digital electronic devices, automobiles, medical devices, *etc*.[9] however the low power density, short life time and slow charge-discharge process are the innate shortcomings of battery technology. The next generation hybrid vehicles, regenerative breaking systems and high power electronic devices demand high power density, large cycle life, dramatically high safety and low cost for the storage devices.[10]

Recently, supercapacitors also known as ultracapacitors or electrochemical capacitors have received great attention and are likely to show equal importance as batteries because of their superior

electrochemical properties. They possess much higher power density (1-10 $kWkg^{-1}$), excellent cycle stability (>100,000), wide temperature range of performance, intrinsically safe charge storage mechanism and they can be charged and discharged in seconds.[11]

1. 2. Supercapacitors

Supercapacitors are energy storage devices which can provide high power densities than conventional batteries and energy densities than capacitors with high cycling stability and large shelf life.[12] Energy density of a capacitor is the amount of energy stored per unit mass and power density is the amount of energy delivered per unit mass of the material.[13] These important parameters that determines the performance of an energy storage device can be expressed as

- ✓ Energy density, $E = \frac{1}{2}CV^2$ (1. 1)
- ✓ Power density, $P_{max} = \frac{E}{\Delta t}$ (1. 2)

Where C is the specific capacitance, V is the voltage, Δt is the discharge time.

The performance of storage devices were compared graphically in Ragon plot **(Figure 1. 3)** with power densities along the vertical axis and energy density along the horizontal axis.[14] It can be seen that the conventional capacitors have high power density but the energy density is lower when compared to batteries and fuel cells. They store limited charges per unit mass or unit volume however the stored charges can be released quickly with very high power. Meanwhile,

batteries and fuel cells can furnish giant energy density with very low power density. High power pulse batteries have emerged as an alternate of battery where high power supply is needed. However the pulse technology sacrifices the energy density and cycle life of the storage device. The trade-off between these performance indicators, power density and energy density has been assimilated in ultracapacitors or supercapacitors and it fill in the gap between conventional capacitors and batteries.

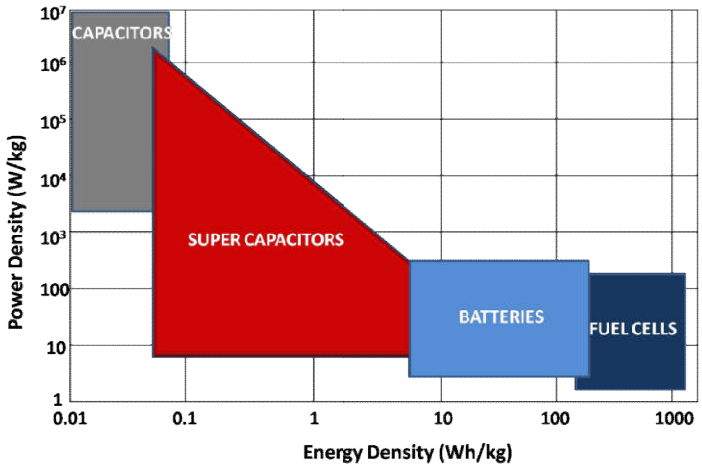

Figure 1. 3. Ragon plot: Graphical comparison of storage devices.[14]

The working principle of supercapacitor is similar to that of conventional capacitors but they use high surface area electrodes and much thinner dielectrics to reduce the distance between electrodes and they possess very high capacitance as per equation given below.

$$\checkmark \quad C = \varepsilon_0 \varepsilon_r \frac{A}{D} \qquad \textbf{(1. 3)}$$

Where A is the surface area of the electrode, D is the thickness of the double layer, ε_o is the permittivity of free space and ε_r is the relative permittivity of the material.[15]

Supercapacitor consists of two electrodes coated with a thin layer of porous and conducting nanomaterial **(Scheme 1. 1).** These electrodes are immersed in an electrolyte solution. When the voltage is applied an electrical double layer is created at the surface of each electrode thus they are also named as electrical double layer capacitors (EDLC).[15] Ascribed to their many advantages supercapacitors are presently being employed in hybrid electric vehicles, voltage stabilization in start/stop systems, solar and wind grids, burst mode power delivery, *etc*.[16]

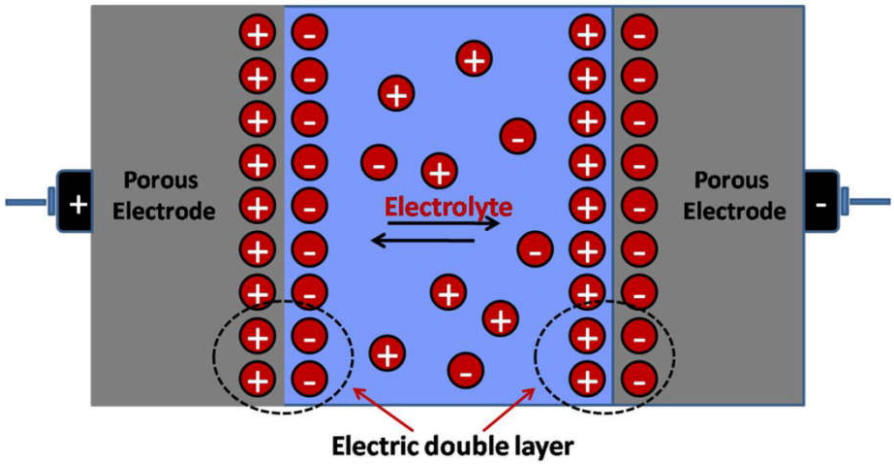

Scheme 1. 1. Schematic of the working principle of a typical supercapacitor device.

1. 3. Classification of supercapacitors

Based on the mechanism of charge storage, super capacitors were classified into three classes; i) Electrical double layer capacitors

(EDLC) in which charge storage takes place non-faradaically, ii) Pseudocapacitors with faradaic process of charge storage, iii) Hybrid capacitors which utilises both faradaic and non faradaic process.[17]

1. 3. 1. Electrical double layer capacitors (EDLC)

An electrochemical double layer capacitor consists of two carbon based electrodes dipped in an electrolyte solution and the electrodes are separated by a separator **(Scheme 1. 1)**. When potential is applied, opposite charges are created at the two electrodes as in conventional capacitors. An electrical double layer (Helmotz layer) is created at each electrode due to selective attraction of the electrolyte ions towards the electrodes through the separator. In EDLC charge storage take place non-faradaically or electrostatically and there is no transfer of matter between electrode and the electrolyte.[18] Thickness of the accumulated charge layer in EDLC is in angstrom units (A^o) and the surface area of the electrodes are very high, thus the specific capacitance of EDLC is much greater than that of conventional capacitors. However when compared to other categories of supercapacitors the specific capacitance of EDLC is relatively small (90-250 Fg^{-1}) due to limited accumulation of charges at the electrical double layer. The commonly used electrode materials in EDLC are carbon based materials such as carbon nanotubes,[19] graphene,[19] activated carbon,[19] carbon aerogels,[20] *etc*.

1. 3. 2. Pseudocapacitors

Pseudocapacitors or electrochemical double layer capacitors store charge faradiacally by the reversible electrochemical reaction at the

electrode-electrolyte interface. In this charge storage mechanism the capacitance and energy/power densities are greater than that of EDLC. Transition metal oxides and conducting polymers, whose near surface charge transport reactions are prominent are the commonly used electrodes in pseudocapacitors. Ruthenium oxide (RuO_2) is the best transition metal based electrode material that is being used in supercapacitors,[21] however the toxic and expensive ruthenium based oxides cannot be used in commercial supercapcitors. The commonly used low cost alternatives are MnO_2, SnO_2, TiO_2, CuO, Co_3O_4, *etc*. Their major disadvantage is the poor electrical conductivity and irreversible faradaic reactions of the electrode material that would results in poor cyclic stability and lower value of specific capacitance.[17] Inorder to overcome these difficulties, the universally accepted approach is to hybridise nanostructured metal oxides with conducting carbon networks such as carbon nanotubes, graphene, activated carbon or carbon aerogels.[14]

1. 3. 3. Hybrid capacitors

As mentioned previously, EDLC offers good cycling stability at the expense of their energy density and pseudocapacitors offers high energy density by sacrifying its cycling stability. Hybrid capacitors incorporate the advantages of EDLC and pseudocapacitors and mitigate their disadvantages by utilizing both faradaic and non faradaic process of charge transfer.[17] Hybrid capacitors offer high energy density, power density and excellent cycling stability. Composite materials (carbon based material and conducting polymers or carbon

materials and metal oxides) are commonly used as the electrodes in hybrid capacitors.

1. 4. Electrode materials -Conventionally used in EDLC

Carbon based electrode materials such as activated carbon, carbon nanotubes, reduced graphene oxide, graphene oxide, carbon aerogels, *etc*. were widely used as electrode material in EDLC due to their high surface area and electronic conductivity.[22] However carbon based electrode materials especially the materials in two dimensional lamellar structures undergo gradual agglomeration during the course of electrochemical reaction.[23] Moreover, in carbon based electrodes the interaction between electrode surface and electrolyte molecule has been unsatisfactory due to insufficient penetration of electrolyte molecule into the electrode surface.[24] Nitrogen doping in carbon based materials were usually carried out inorder to enhance the electrochemical properties of the electrode material. The lone pair of electrons on nitrogen provides surface polarity, and electrode-electrolye surface wettability which enhances the charge transport process between the electrode surface and electrolyte molecules.[25]

Graphitic carbon nitride (g-C_3N_4) has emerged as an alternative for carbon based EDLC material owing to its intrinsically high nitrogen content, low cost, chemical and mechanical stability. The lone pair of electrons present in the N atom of the ring structure of g-C_3N_4 induces more polarity in the molecule which enhances the wettability and the charge carrier mobility in the electrode material.[26,27]

1. 5. Graphitic Carbon Nitride (g-C_3N_4)

Graphitic carbon nitride is the most stable allotrope of the carbon nitride family. The material was first prepared by Berzilius and Liebig in 1834 however their potential applications were not explored yet.[28] The 2D π conjugated network of g-C_3N_4 originated from the interconnected s-triazine (sym. triazine; 1, 3, 5-triazine) and tri-s-triazine units through weak Vander walls forces **(Scheme 1. 2)**.[28] The hexagonal ring structure of g-C_3N_4 consists of sp^2 hybridized nitrogen atom and carbon atom similar to that of graphite, however the alternate carbon atom in the hexagonal ring structure of graphite being replaced by nitrogen atom in g-C_3N_4. The pi conjugated lamellar structure facilitate the transport of photo induced charge carriers and narrow down the band gap (2.7 eV) so as to absorb the visible region of the solar spectra.[29] The valance band and conduction band edge with respect to normal hydrogen electrode (NHE) of g-C_3N_4 are -1.3 V and 1.4 V respectively. Moreover, compared to other oxide and sulphide based photocatalysts, g-C_3N_4 is highly stable in acid and alkaline medium because of the strong covalent bond existing between carbon and nitrogen atom of g-C_3N_4. Owing to these properties the material is widely used as a photocatalyst for the oxidative removal of dissolved organics from water and as a catalyst for artificial H_2 generation.[28,30]

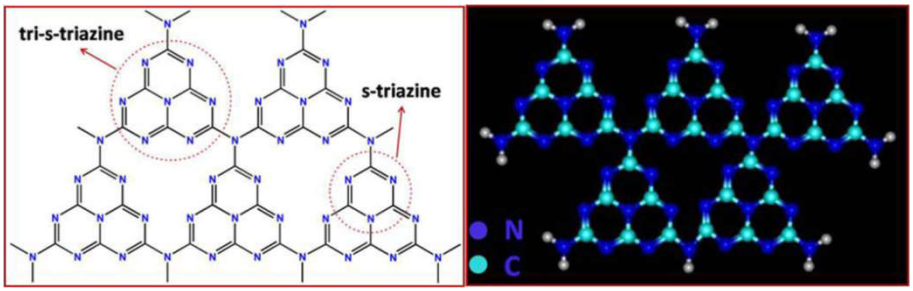

Scheme 1. 2. Schematic of the 2D π conjugated network structure of g-C_3N_4.

Recently polymeric organic semiconductor g-C_3N_4 has received great deal of attention in energy storage and energy conversion applications due to its versatile electronic structure, rapid charge separation, excellent chemical, thermal and mechanical stability, cost effectiveness and environmental friendliness.[31] The lone pair of electron present in the nitrogen rich g-C_3N_4 could offer additional negative charges into the ring structure that could provide more surface polarity, electron donor ability, and thereby enhances the charge transport properties in the material.[32] Moreover, the two dimensional layered structure possessed by g-C_3N_4 could provide maximum surface layer atoms and short diffusion pathways for ion diffusion process. They also offer large surface active sites for achieving better wettability at electrode-electrolyte interfaces.[23] However the surface area and electronic conductivity of g-C_3N_4, which is directly related to the specific capacitance and power density of EDLC supercapacitor is intrinsically low which limits their practical application.[23] The development of efficient supercapacitor electrodes based on g-C_3N_4 with maximum specific capacitance and cycling stability still remain a big challenge

but imperative for exploring their potential as an alternative energy storage system for commercial application.

1. 5. 1. g-C_3N_4 based Nanohybrid Materials as Supercapacitor Electrodes

An effective yet facile method to bypass the issue of agglomeration of 2D lamellar structures in g-C_3N_4 which makes them unsuitable for practical application is to intercalate with other inorganic functional materials such as transition metal oxides and sulphides. The pseudocapacitive nature of inorganic oxides and sulphides provides efficient charge transport at the electrode-electrolyte surfaces *via* synergistic effect between faradaic and non-faradaic process of charge transport.

Inspired by this perspective, recently, Chen *et al.* reported a two dimensional hybrid structure of g-C_3N_4/CoS which exhibited a specific capacitance value of 668 Fg^{-1} at a current density of 2 Ag^{-1} which is higher than the individual components in a three electrode cell assembly.[33] In a recent report by Ansari *et al.* commercially purchased MoS_2 and g-C_3N_4 were used for the preparation of MoS_2/g-C_3N_4 heterostructure and was used as supercapacitor electrode in a three electrode cell assembly. The hybrid sample delivered a high specific capacitance of 240 Fg^{-1} which is much higher that of bare MoS_2 (48.77 Fg^{-1}) with good cyclic stability.[23] The composite sample, MoS_2/g-C_3N_4 was also employed as a photocatalyst under visible light for the oxidative removal of rhodamine B from aqueous solution. Recently Zhao *et al.* reported a g-C_3N_4 hybridised TiO_2 nanoparticle assembly

by hydrothermal method which exhibited a high specific capacitance of 125.10 Fg^{-1} at a current density of 1 Ag^{-1} which can be attributed to the enhanced charge transport properties provided by g-C_3N_4 sheets.[34] The reports show that g-C_3N_4 based hybrid materials has been explored as a new area of research that provide challenges and opportunities particularly in the area of energy conversion, storage and environmental applications.

A series of novel g-C_3N_4 based nano semiconductor hybrid materials such as g-C_3N_4/TiO_2, g-C_3N_4/MnO_2, g-C_3N_4/SnO_2, g-C_3N_4/Co_3O_4 and g-C_3N_4/CuO electrode materials were developed for supercapacitor applications. The electrochemical properties of the fabricated electrodes were measured in a symmetric two electrode configuration. Except TiO_2 all other nanosemiconductors exhibit pseudocapacitive or faradaic nature of charge transport at the electrode-electrolyte interface. The nanohybrid electrode materials were fabricated by integrating the two charge storage processes (faradaic and non-faradaic) and they were expected to exhibit synergistic mechanism for charge storage. Moreover, the semiconductor fillers may act as spacers to effectively separate the layers of 2D g-C_3N_4 which facilitate an effective transport of ions by increasing the accessible surface area for the electrode process.

1. 6. Fe_2O_3@Carbon Nano-hybrid structures from Discarded Blades as Supercapacitor Electrodes

The solid wastes such as metals, plastics, agricultural wastes, *etc.* are the major contributing elements for municipality wastes which finally

end in landfills. The landfills produce poisonous gases such as methane, CO_2, *etc*., or it contaminates the ground water. The concept of regenerative economy or closed economy considers the waste material as a resource by recycling and reusing the garbages.[35] A novel cost effective and environmentally benign nano-hybrid structure; Fe_2O_3@Carbon was prepared from discarded razor blades and glucose by precipitation technique and followed by the hydrothermal carbonization process. The hybrid material was employed as electrode material for the fabrication of symmetric supercapacitor devices.

1. 7. Environmental Remediation

Population explosion and urbanization have lead to the pollution of environment which also has a severe implication on the contamination of water bodies. Water pollution may be defined as the contamination of underground water, lakes, seas, rivers or streams by substances which are harmful to living beings. Industrial and agricultural effluents containing heavy metal ions, pesticides, fertilizers and organic dyes are the major sources of water contamination. These pollutants are water soluble and chemically stable thus it causes eutrophication, larger biological oxygen demand and biomagnifications in the aquatic environment.[36] The researchers all over world have devoted for an efficient method for the removal/degradation of dissolved organic pollutants from the effluent water to create a clean and healthy aquatic environment. Sedimentation, filtration, coagulation, biological treatments and adsorption on porous substrates are the commonly used non-destructive phase separation techniques. Advanced oxidation process (AOP) is a special class of oxidation process which is designed

to remove dissolved impurities from water.[37]This in situ chemical oxidation process degrades the pollutants into CO_2, H_2O and harmless salts. The technique involves the production of highly reactive hydroxyl radicals ($^{\cdot}OH$) which are excellent oxidant species for the oxidative removal of pollutants. Fentons reagent (Fe^{2+}/H_2O_2),[37] H_2O_2/UV light,[38] O_3/UV light[38], *etc*. are the commonly used advanced oxidation processes. Nevertheless the techniques are excellent AOPs, it is not yet commercialized due to its high cost and stringent experimental conditions required for the reaction. *Heterogeneous semiconductor photocatalysis*[39] is an effective advanced oxidation process, which has received immense attention due to its high efficiency, photochemical stability, ambient reaction condition, recyclability, cost effectiveness and environmentally benign nature.

1. 8. Photocatalysis

Photocatalysis is the acceleration of a photoreaction in presence of a catalyst. The substance that modifies the rate of the chemical reaction in the presence of light is known as photocatalyst.[39] An ideal photocatalyst should be chemically and biologically inert, economical and environmentally benign. Moreover, it should be capable to activate large cycles of photoreactions without sufficient degradation in the photoactivity. In photocatalysis the adsorbent molecules get adsorbed on the surface of the catalyst and is oxidized and/or reduced simultaneously when the catalyst absorbs light radiation. It transfers electrons from the conduction band of the catalyst to the adsorbed molecule which is governed by the conduction band position of the catalyst and the redox potential of the adsorbed molecule (acceptor).

Thermodynamically the redox potential of the acceptor must be below the conduction band of semiconductor **(Figure 1. 4)**.[40] The process of transfer of the electron to the adsorbed molecule is called reduction. The adsorbate can acts as a donor when the potential of the adsorbate is above the valance band of semiconductor and this electron transfer process is called oxidation. In general the energy level at the bottom of the conduction band decides the reducing power of the photoelectrons and the energy levels at the top of the valance band determines the oxidative power of the photoholes.[41]

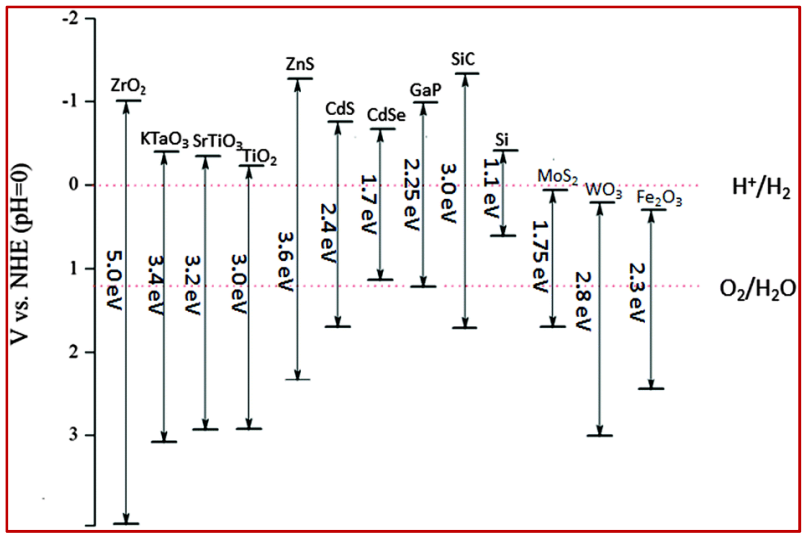

Figure 1. 4. Band gaps and band edges (CB bottom and VB top) of some wide bandgap semiconductors (pH = 0, vs. NHE at room temperature).

1. 8. 1. Titanium dioxide (TiO_2) as Photocatalyst

Photocatalysis is the acceleration of a photoreaction in presence of a catalyst. The photocatalytic functional applications of TiO_2 has emerged in the scientific world just after the photolysis of water into hydrogen and oxygen by Fujishima and Honda which was carried out using a titanium dioxide electrode in an electrochemical cell.[42] They reported that TiO_2 has a sufficiently positive valence band edge to oxidize water to oxygen and also the photogenerated electrons are reducing enough to produce super oxide radicals.

1. 8. 2. Crystal structure of TiO_2

TiO_2 is an ideal and fascinating photocatalytic material due to its cost effectiveness and high chemical and thermal stability. TiO_2 usually exists in three polymorphic varieties such as anatase (tetragonal, a = b = 3.782 Å, c = 9.502 Å), rutile (tetragonal, a = b = 4.854 Å, c = 2.953 Å) and brookite (orthorhombic, a = 5.436 Å, b = 9.166 Å, c = 5.135 Å) phases which differ in the arrangement of elementary particles **(Figure 1. 5)**. In all the three crystal forms, Ti^{4+} ions are surrounded by irregular octahedrals of oxide ions.[43] In anatase phase these octahedrals are connected by their vertices (corners), whereas in rutile these octahedrals are connected though the edges and in brookite octahedrals are connected by both corner shared and edge shared manner. Rutile structure is closer packed than anatase. The theoretical densities of rutile and anatase phases are 4.27 g/cc and 3.89 g/cc respectively. Brookite is the most trivial phase of TiO_2 and spontaneously transformed to rutile at around 750 ^oC. Rutile phase is the

thermodynamically most stable phase and the metastable anatase is the photocatalytically more active phase of TiO_2. Anatase transforms exothermically to rutile phase in the temperature range 600-800 ^oC.[41]

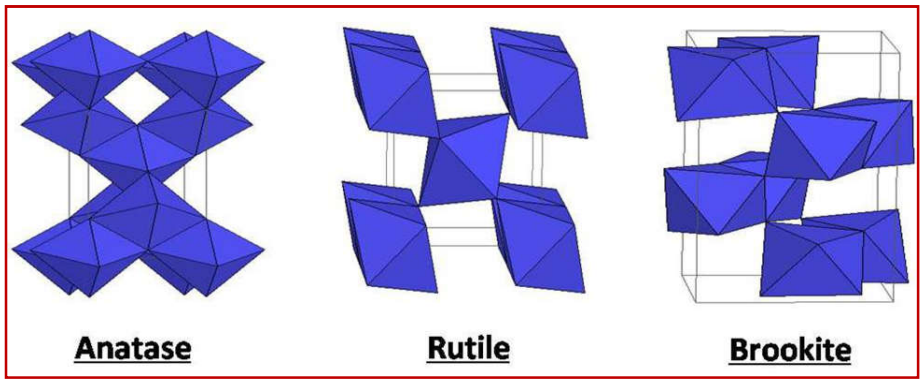

Figure. 1. 5. Crystal structures of anatase, brookite, and rutile.

1. 8. 3. Band structures of TiO_2 and Photoeffect

TiO_2 is a wide band gap semiconductor. The outer electronic configuration of titanium (Ti) is $4s^2 3d^2$ and that of oxygen is $2s^2 2p^4$. The valance band of TiO_2 consists of oxygen 2p orbital and the conduction band is composed of 3d orbitals of Ti. The Ti atoms in TiO_2 are in distorted octahedral environment and possess Ti^{4+} with $3d^0$ electronic configuration. When TiO_2 is exposed to near-UV radiation, the valance band electrons are excited to conduction band by creating a hole in the valance band. The excited electrons are in 3d state thus the valance band electrons are at different parity with conduction band. The probability of the transfer of conduction band electrons back to valance band is now restricted due to the dissimilar parity. Thus the chance for electron (e^-) hole (h^+) pair recombination is diminished considerably. However, in the case of other transition metal oxides 3d

states are present in both the valance state and conduction state and the probability of electron-hole (e^- - h^+) pair recombination is much higher. In ZnO, the valance band consists of only d orbital and the conduction band is made of s-p hybrid orbitals. Thus in ZnO also the probability of (e^--h^+) recombination is curtailed considerably.[44]

The band gap energy of rutile is 3.0 eV whilst that of anatase is 3.2 eV. Rutile absorbs some percentage of visible radiation than anatse, however the photocatalytic activity of anatase is greater than that of rutile. The reasons for the catalytic deficiency of rutile are (1) the phase formation temperature of rutile is greater than that of anatse and this high temperature treatment increases the grain size and decreases the active surface sites of rutile TiO_2. (2) The rutile phase carries very few number of hydroxyl groups on its surface. Hydroxyl groups are excellent hole scavengers, thus in the absence of hydroxyl groups on the surface of TiO_2 the electron-hole recombination rate increases. Moreover, limited number of oxygen vacancies in rutile, reduces its catalytic activity. Oxygen vacancies usually create oxygen trapping sites and these oxygen molecules are excellent electron scavengers. (3) The conduction band electrons of anatase have more reducing ability than rutile thus due to these reasons anatase is acknowledged as more efficient photocatalytic phase.[45]

1. 8. 3. Mechanism of Photocatalysis

Photo illumination of TiO_2 semiconductor with UV radiation of wavelength 388 nm or shorter causes the excitation of valance band electrons to conduction band (e^-) by creating a hole (h^+) in the valance

band **(Scheme 1. 3)**. The generated charge carriers are highly unstable species, thus in photocatalytic process there is always a competition between charge carrier transfer and (e^--h^+) pair recombination. The photogenerated electrons in the conduction band are powerful reductants and valance band holes are powerful oxidants, they initiate numerous chemical reactions at the surface of the catalyst. If the adsorbed species are water and dissolved oxygen (H_2O/O_2), H_2O get oxidized by positive holes to $^{\cdot}OH$ and H^+. The reduction of easily reducible O_2 results in the formation of superoxide radical anion ($^{\cdot}O_2^-$), after that it react with H^+ to produce hydroperoxyl radical ($^{\cdot}HO_2$) and then with electron to produce HO_2^- finally with H^+ ions to form H_2O_2. The overall reaction path way for the degradation of organic contaminants in presence of the reactive oxygen species such as $^{\cdot}OH$, $^{\cdot}O_2^-$, and H_2O_2 can be represented by the following equations.[40,46]

1. *Photo-excitation*

$$TiO_2 + h\nu \rightarrow TiO_2\,(e^-_{cb} + h^+_{vb})$$

2. *Oxidation reactions due to h^+_{vb}*

$$H_2O + h^+_{vb} \rightarrow {}^{\cdot}OH + H^+$$

$$2H_2O + h^+_{vb} \rightarrow H_2O_2 + 2H^+$$

$$OH^- + h^+_{vb} \rightarrow {}^{\cdot}OH$$

3. *Reduction reactions due to e^-_{cb}*

$$O_2 + e^-_{cb} \rightarrow {}^{\cdot}O_2^-$$

$$^{\cdot}O_2^- + 2\,H^+ \rightarrow H_2O_2$$

$$H_2O_2 + e^-_{cb} \rightarrow {}^{\cdot}OH + OH^-$$

$^{\cdot}O_2^- + H_2O_2 \rightarrow {}^{\cdot}OH + OH^-$

$^{\cdot}O_2^- + H^+ \rightarrow {}^{\cdot}HO_2$

$^{\cdot}HO_2 + e^-_{cb} \rightarrow HO_2^-$

$HO_2^- + H^+ \rightarrow H_2O_2$

$2\,{}^{\cdot}HO_2 \rightarrow O_2 + H_2O_2$

4. *Degradation of the pollutant* in presence of reactive oxygen species (ROS)

Pollutant + ROS → intermediates + CO_2 + H_2O

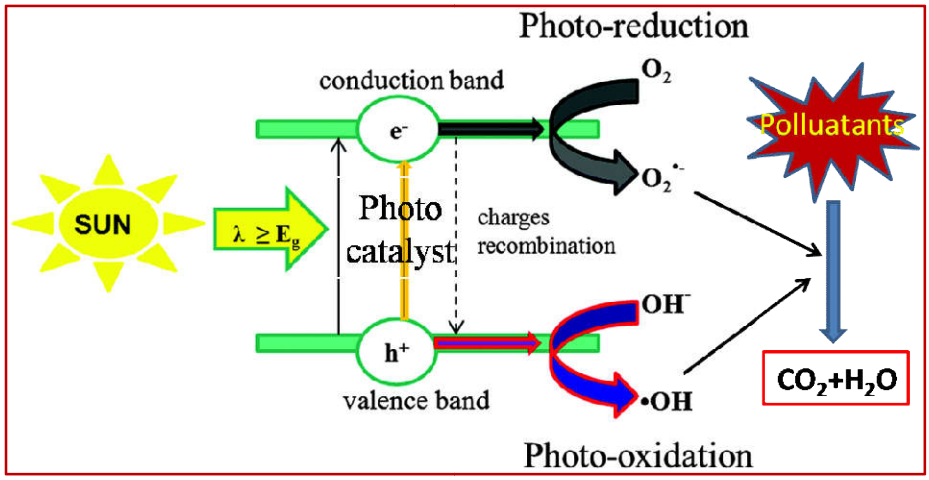

Scheme 1. 3. Schematic representation of the mechanism of Photocatalysis.

1. 9. TiO_2 based Nanoheterostructures as Visible light active Photocatalyst

Eventhough TiO_2 is a well known photocatalyst with environmentally and economically benign stable structure, the band gap energy of 3.2

eV (λ~387 nm) limits its application in sunlight/visible light harvesting technology.[47] Moreover, the fast rate of charge recombination at the surface of TiO_2 reduces the concentration of charge carriers for further reaction. The sunlight consist of 50 % visible radiation and the development of visible light active catalyst with minimum trade-off between charge transport and charge recombination is an extensive area of research.

To address this issue numerous efforts have been reported to enhance the light absorption and charge separation capability of anatase TiO_2 which includes metal and non metal doping, dye sensitization, *etc*.[48-50] To improve the photocatalytic activity of anatase TiO_2, fabrication of nano-heterostructures by coupling TiO_2 with narrow band gap semiconductors with conduction band position higher than that of TiO_2 have received great deal of attention recently. The narrow band gap semiconductors such as CdS, Polyaniline and g-C_3N_4 will act as a chromophore to absorb visible region of the solar spectra and it shifts the absorption edge of the composite sample to longer wavelength region.[51-53] Moreover, the photo generated electron from the conduction band of narrow band gap semiconductors will be transferred to the conduction band of TiO_2, and thereby facilitate an effective interfacial charge transport in the hybrid sample by reducing the rate of electron-hole pair recombination. Thus the creation of different reaction sites for oxidation and reduction process improves the overall performance efficiency of the catalyst.[51-53]

1. 9. 1. TiO_2-CdS Nanoheterostructures as Sunlight Driven Photocatalyst

Cadmium sulphate (CdS) is an excellent sunlight harvester material owing to its direct narrow band gap (2.4 eV) and can be used as a sensitizer for wide band gap semiconductors such as TiO_2. Valance band and conduction band levels of CdS semiconductor lies above that of TiO_2 which facilitate effective charge separation by reducing the possibility for photo generated electron-hole pair recombination. The work embodies our attempt to fabricate CdS hybridized TiO_2 photocatalysts in which special attention was made to optimize the minimum concentration of CdS required to sensitize TiO_2 matrix.

1. 10. Oil Spill Sorbents

Oil spill is a form of environmental pollution, especially aquatic pollution due to the release of oil from tankers, ships and oil rigs. The spilled oil severely affects the aquatic organisms and vegetation. Skimming, burning and isolations are the major conventionally used techniques for oil-spill removal. These techniques are inefficient and the incomplete burning results in the formation of toxic fumes.[54] Oil absorbing sorbent materials like organophillic clays, silica aerogels, poly-propylene, polyethelene terephthalate, graphene, activated carbon, *etc*. has been used recently for the removal of spilled oils from water. The most important condition for a material to be used as a sorbent material in large scale environmental remediation applications is efficiency, biocompatibility, recyclability and low cost.[55] However, the removal of the sorbent material from the aquatic environment along

with the adsorbed oil is tedious and time consuming. Introduction of magnetic functionality in the sorbent material facilitate rapid removal of the sorbent material in presence of an external magnetic, thereby enhances recyclability and efficiency of the sorbent material.[54] Magnetic iron oxide is proven to be an excellent candidate with biocompatibility and very low cytotoxicity for the environmental remediation applications.[56] Different types of iron oxide based sorbents such as collagen fiber-Fe_3O_4/γ-Fe_2O_3,[56] Fe_2O_3@carbon,[57] Fe-C nano heterostructures,[58] iron doped carbon nanotubes,[59] polystyrene-Fe_2O_3, *etc*.[60] were extensively studied as a magnetically separable adsorbent material.

1. 10. 1. Fe_2O_3@Carbon Nano-hetero structures from discarded razor blades as Oil-spill cleaners

In the present thesis we report a novel Fe_2O_3@Carbon nano-hetero structures prepared by the hydrothermal carbonization process by using discarded razor blades and glucose solution as precursors. The idea behind the synthesis of Fe_2O_3@C was based on the closed economy concept of Reducing, Reusing and Recycling of the garbage materials. The as synthesized Fe_2O_3@C composite material was employed as an oil-adsorbent material for the removal of artificially created oil-spills from water. The synthesized sorbent material is low cost, biocompatible and show very high efficiency for the removal of oil-spills. The oil adsorption by the material is quite instantaneous, making Fe_2O_3@C an attractive candidate for the oil removal process.

1. 11. Objectives of the Thesis

1. 11. 1. Energy objectives

1. Synthesis of g-C_3N_4 semiconductor by high temperature pyrolysis method.
2. Development of TiO_2 nanotube dispersed g-C_3N_4 nanohybrid materials (g-C_3N_4/TNT) for supercapacitor electrode applications.
3. Synthesis of g-C_3N_4/MnO_2 and g-C_3N_4/SnO_2 nano-heterostructures by chemical reduction method.
4. Evaluation of the electrochemical performance of the composite electrodes, g-C_3N_4/MnO_2 and g-C_3N_4/SnO_2.
5. Development of g-C_3N_4/Co_3O_4, g-C_3N_4/CuO nano-heterostructures and their characterization.
6. Electrochemical performance evaluation of the composite electrode g-C_3N_4/Co_3O_4 and g-C_3N_4/CuO nano-heterostructures.
7. Development of Fe_2O_3@Carbon nano-hybrid materials from discarded razor blade as supercapacitor electrodes.

1. 11. 2. Environmental objectives

1. To develop sunlight driven photocatalyst by fabricating TiO_2/CdS nano-heterostructures.
2. Characterization and evaluation of the photocatalytic activity of TiO_2/CdS composites.
3. To analyze the performance of magnetically recoverable Fe_2O_3@Carbon nano-hybrid structures as oil-spill removers.

1. 12. Overview of the Experimental Work

A detailed discussion on the experimental methods adopted for the synthesis of the nano hybrid materials and the characterization techniques used are included in Chapters 2. Chapters 3 to 6 are based on the energy perspective of the present research work. Second part of Chapter 6 and Chapter 7 are based on the environmental perspective of the thesis. In Chapter 3, the electrochemical properties of TiO_2 nano tube dispersed graphitic carbon nitride (g-C_3N_4) have been discussed by fabricating symmetric supercapacitor device. In Chapter 4, g-C_3N_4/MnO_2 and g-C_3N_4/SnO_2 heterostructures were prepared and their supercapacitor device applications in two electrode configuration were investigated. In Chapter 5, pseudocapacitive transition metal oxides such as Co_3O_4 and CuO were anchored on the surface of g-C_3N_4 and their symmetric supercapacitor device applications were analyzed. In Chapter 6, a novel strategy was adopted for the synthesis of Fe_2O_3@Carbon nano hybrid material from discarded razor blades and glucose solution as precursors. The material was successfully used as electrode material for symmetric supercapacitor device in two electrode configuration. The second part of the Chapter 6 deals with the study on the oil-spills removal ability of magnetically recoverable Fe_2O_3@Carbon adsorbent material for environmental applications. Chapter 7 deals with the environmental remediation application of the nano hybrid material based on TiO_2 and CdS. In this research work TiO_2-CdS hetero-structures were developed to enhance the visible light driven photocatalytic activity of TiO_2. The materials were well characterized and employed as a sunlight active photocatalyst for the decomposition of methyl orange dye present in water as a model pollutant.

References

1. A. Sinha, M. Shahbaz, *Renewable Energy*, 2018, 119, 703.
2. I. R. Pillai, R. Banerjee, *Energy*, 2009, 34, 970.
3. S. Shafiee, E. Topal, *Energy policy*, 2009, 37, 181.
4. S. Mittal, H. Dai, S. Fujimori, T. Masui, *Appl. Energy*, 2016, 166, 301.
5. Press Information Bureau, *Govt. of India, Ministry of new and renewable energy*, 2017.
6. M. D. Stoller, R. S. Ruoff, *Energy. Envir. Sci*., 2010, 3, 1294.
7. B. Babu, S. G. Ullattil, R. Prasannachandran, J. Kavil, P. Periyat, M. M. Shaijumon, *ACS Sustain. Chem. Eng*., 2018, 6, 5401.
8. M. Armand, J. M. Tarascon, *Nature*, 2008, 451, 652.
9. D. Damien, G. S. Anjusree, A. S. Nair, M. M. Shaijumon, *RSC Adv*., 2016, 6, 45802.
10. Y. Zhang, H. Feng, X. Wu, L. Wang, A. Zhang, T. Xia, H. Dong, X. Li, L. Zhang, *Int. J. Hydrog. Energy*., 2009, 34, 4889.
11. R. B. Rakhi, W. Chen, D. Cha, H. N. Alshareef, *J. Mater. Chem*., 2011, 21, 16197.
12. B. E. Conway, *Kluwer Academic, Plenum, New York*, 1999.
13. R. B Rakhi, D. Cha, W. Chen, H. N. Alshareef, *J. Phys. Chem. C*, 2011, 115, 14392.
14. R. Kotz, M. Carlen, *Electrochim. Acta*, 2000, 45, 2483.
15. G. Wang, L. Zhang, J. Zhang, *Chem. Soc. Rev*., 2012, 41, 797.
16. L. L. Zhang, X. S. Zhao, *Chem. Soc. Rev*., 2009, 38, 2520.
17. M. S. Halper, J. C. Ellenbogen, *The MITRE Corporation, McLean, Virginia, USA*, 2006.

18. H. Chen, T. N. Cong, W. Yang, C. Tan, Y. Li, Y. Ding, *Prog. Nat. Sci*., 2009, 19, 291.

19. J. Gamby, P. L. Taberna, P. Simon, J. F. Fauvarque, M. Chesneau, *J. power sources*, 2001, 101, 109.

20. W. Li, G. Reichenauer, J. Fricke, *Carbon*, 2002, 40, 2955.

21. J. P. Zheng, P. J. Cygan, T. R. Jow, *J. Electrochem. Soc*., 1995, 142, 2699.

22. P. J. Hall, M. Mirzaeian, S. I. Fletcher, F. B. Sillars, A. J. Rennie, G. O. Shitta-Bey, G. Wilson, A. Cruden, R. Carter, *Energy Environ. Sci*., 2010, 3, 1238.

23. S. A. Ansari, M. H. Cho, *Sci. Rep*., 2017, 7, 43055.

24. Z. Li, L. Wu, L. Wang, A. Gu, Q. Zhou, *Electrochimi. Acta*, 2017, 231, 617.

25. Y. Gong, M. Li, Y. Wang, *Chem. Sus. Chem*., 2015, 8, 931.

26. Z. Zhao, Y. Sun, F. Dong, *Nanoscale*, 2015, 7, 15.

27. H. Chen, F. Sun, J. Wang, W. Li, W. Qiao, L. Ling, D. Long, *J. Phys. Chem. C*, 2013, 117, 8318.

28. A. Thomas, A. Fischer, F. Goettmann, M. Antonietti, J. O. Müller, R. Schlögl, J. M. Carlsson, *J. Mater. Chem*., 2008, 18, 4893.

29. X. Wang, K. Maeda, A. Thomas, K. Takanabe, G. Xin, J. M. Carlsson, K. Domen, M. A. Antonietti, *Nat. Mater*., 2009, 8, 76.

30. S. C. Yan, Z. S. Li, Z. G. Zou, *Langmuir*, 2009, 25, 10397.

31. Y. Gong, M. Li, Y. Wang, *Chem. Sus. Chem*., 2015, 8, 931.

32. D. Hulicova, J. Yamashita, Y. Soneda, H. Hatori, M. Kodama, *Chem. Mater*., 2005, 17, 1241.

33. D. Jiang, Q. Xu, S. Meng, C. Xia, M. Chen, *J. Alloys Compound*., 2017, 706, 41.

34. Y. Zhao, L. Xu, S. Huang, J. Bao, J. Qiu, J. Lian, L. Xu, Y. Huang, Y. Xu, H. Li, *J. Alloys Compound*., 2017, 702, 178.

35. Y. Geng, J. Sarkis, S. Ulgiati, P. Zhang, *Science*, 2013, 339, 1526.

36. F. A. Khan, A. A. Ansari, *Bot. Rev*., 2005, 71, 449.

37. E. Chamarro, A. Marco, S. Esplugas, *Water Res*., 2001, 35, 1047.

38. I. Arslan, I. A. Balcioglu, T. Tuhkanen, *Environ. Technol*., 1999, 20, 921.

39. U. I. Gaya, A. H. Abdullah, *J. Photoch. Photobio. C*, 2008, 9, 1.

40. A. L. Linsebigler, G. Lu, J. T. Yates Jr, *Chem. Rev*., 1995, 95, 735.

41. M. A. Fox, M. T. Dulay, *Chem. Rev*., 1993, 93, 341.

42. A. Fujishima, K. Honda, *Nature*, 1972, 238, 37.

43. D. A. Hanaor, C. C. Sorrell. *J. Mater. Sci*., 2011, 46, 855.

44. S. Banerjee, J. Gopal, P. Muraleedharan, A. K. Tyagi, B. Raj, *Curr. Sci*., 2006, 90, 1378.

45. P. Bouras, E. Stathatos, P. Lianos, *Appl. Catal. B: Environ*., 2007, 73, 51.

46. J. Schneider, M. Matsuoka, M. Takeuchi, J. Zhang, Y. Horiuchi, M. Anpo, D. W. Bahnemann, *Chem. Rev*., 2014, 114, 9919.

47. P. Periyat, S. C. Pillai, D. E. McCormack, J. Colreavy, S. J. Hinder, *J. Phys. Chem. C*, 2008, 112, 7644.

48. X. Jie, N. Bao, B. Gong, S. Zhou, *Nano-Structures & Nano-Objects*, 2017, 12, 98.

49. X. Chen, C. Burda, *J. Am. Chem. Soc*., 2008, 130, 5018.

50. H. Choi, P. K. Santra, P. V. Kamat, *ACS Nano*, 2012, 6, 5718.

51. G. S. Li, D. Q. Zhang, J. C. Yu, *Environ. Sci. Technol*. 2009, 43, 7018.

52. X. Li, D. Wang, G. Cheng, Q. Luo, J. An, Y. Wang, *Appl. Catal. B Environ*., 2008, 81, 267.

53. X. Zhou, F. Peng, H. Wang, H. Yu, Y. Fang, *Chem. Comm*., 2011, 47, 10323.

54. K. G. Raj, P. A. Joy, *Journal of environmental chemical engineering*, 2015, 3, 2068.

55. J. Song, S. Huang, Y. Lu, X. Bu, J. E. Mates, A. Ghosh, R. Ganguly, C. J. Carmalt, I. P. Parkin, W. Xu, C. M. Megaridis, *ACS Appl. Mater. Interfaces*, 2014, 6, 19858.

56. P. Thanikaivelan, N. T. Narayanan, B. K. Pradhan, P. M. Ajayan, *Sci. Rep*. 2012, 20, 230.

57. Q. Zhu, F. Tao, Q. Pan. *ACS Appl. Mater. Interfaces*, 2010, 2, 3141.

58. Y. Chu, Q. Pan, *ACS Appl. Mater. Interfaces*, 2012, 4, 2420.

59. X. Gui, Z. Zeng, Z. Lin, Q. Gan, R. Xiang, Y. Zhu, A. Cao, Z. Tang, *ACS Appl. Mater. Interfaces*, 2013, 5, 5845.

60. P. Tempesti, M. Bonini, F. Ridi, P. Baglioni, *J. Mater. Chem. A*, 2014, 2, 1980.

Chapter Two

Materials and Methods

Contents

2. 1. Introduction

The properties of the semiconducting nanomaterials are associated directly with the nano structural morphology of the materials. It is during the key synthetic step that the desired properties are incorporated into the nanomaterial. Wet chemical methods have been adopted as the experimental method for the synthesis of nanomaterial because of its salient features such as compositional homogeneity, low temperature processing and phase purity. In this Chapter, section 2. 2 deals with the detailed strategies adopted for the synthesis of the semiconductor nano materials and their heterostructures. Section 2. 3, 2. 4 and 2. 5 include the various techniques used for analyzing the electrochemical energy storage and the environmental applications of synthesized semiconductor nanomaterials and their heterostructures. Proper characterization of the material is also important to analyse the

structure-property relation of the material. In final part of this Chapter (section 2. 6) prime importance have been given for scientifically explaining the theoretical principles and the utility of the various quantitative and qualitative characterization techniques employed in the present research work. Various chemicals used for the synthesis of the photocatalysts and the electrode materials are tabulated in **Table 2.1**.

Table 2. 1. List of chemicals used for the synthesis and application studies

SI. No.	Chemicals	Formula	Manufacturer
1	Titanium Tertiary Butoxide	Ti $(OC_4H_9)_4$	Sigma Aldrich, 97 %
2	Manganese Acetate Tetrahydrate	Mn $(CH_3COO)_2$	Alfa Aesar, 98 %
3	Cadmium Nitrate	Cd $(NO_3)_2.4H_2O$	Sigma Aldrich, 97 %
4	Thiourea	SC $(NH_2)_2$	Sigma Aldrich, 97 %
5	Sodium Molybdate Dihydrate	Na_2MoO_4. $2H_2O$	Alfa Aesar, 98 %
6	Tin (II) Chloride Dihydrate	$SnCl_2$	Alfa Aesar, 98 %
7	Potassium Permanganate	$KMnO_4$	Alfa Aesar, 98 %
8	Cobalt Nitrate	Co $(NO_3)_2$. $6H_2O$	Merck, India, 97 %
9	Copper Nitrate	Cu $(NO_3)_2$. H_2O	Merck, India, 97 %
10	Manganese Sulphate	$MnSO_4$	Merck, India, 97 %
11	D-Glucose	$C_6H_{12}O_6$	Alfa Aesar, 98 %
12	Oxalic Acid	$C_2H_2O_4$	Qualigens, 98 %
13	Ethanol	C_2H_5OH	Commercially purchased
14	Nitric Acid	HNO_3	Merck, India, 72 %
15	Hydrochoric Acid	HCl	Merck, India, 69 %
16	Isopropyl Alcohol	C_3H_7OH	Merck, India, 98 %
17	Methyl Orange	$C_{14}H_{14}N_3NaO_3S$	Qualigens, AR grade
18	Ammonium Hydroxide	NH_4OH	Merck, India, 30 %

2. 2. Synthesis of Nano Semiconductor Hybrid materials

2. 2. 1. Synthesis of g-C_3N_4

Graphitic carbon nitride (g-C_3N_4) was synthesized by simple pyrolysis followed by self-polymerisation of thiourea under self-supported atmosphere in a covered crucible. 5 g of thiourea is dried at 80 ^oC/ 24 hrs and heated at 550 ^oC/ 3 hrs in a muffle furnace at a heating rate of 2 ^oC/minutes.[1] This method circumvents the requirement of laborious experimental set up conventionally used for the synthesis of carbon nitride. The yellow colored g-C_3N_4 so obtained was washed with 25 ml de-ionised water to remove any residual alkaline species. The residue was then dried at 80 ^oC/ 24 hrs in a hot air oven.

2. 2. 2. Synthesis of TiO_2 Nanotubes (TNT)

TiO_2 nanotubes (TNT) were synthesized from anatase TiO_2 by adopting a previously reported modified hydrothermal method.[2] In a typical method 5 g of anatase TiO_2 nanoparticles were stirred with 60 ml, 10 N NaOH solution for 4 hrs and the resulting suspension was transferred to a 100 ml stainless steel autoclave and kept at a temperature of 150 ^oC/48 hrs. The obtained precipitate was washed with 0.1 N HCl and then with deionised water until neutral pH is attained. The product is dried overnight at 80 ^oC and then calcined at 400 ^oC/2 hrs during which crystalline anatase TiO_2 nanotubes are evolved.

2. 2. 3. Synthesis of TNT/g-C_3N_4 Nano Heterostructure

TNT/g-C_3N_4 heterojunction composites were fabricated by a simple hydrothermal method. Different weight percentages of TNT and g-C_3N_4 having TNT/g-C_3N_4 ratio 1:1, 1:2 and 1:4 was accurately weighed out and sonicated for 20 minutes in a 1:1 mixture of ethanol and water. The homogeneous suspension so obtained was transferred to a 100 ml teflon lined stainless steel autoclave and kept at a temperature of 120 ^oC for 8 hrs. Then the products were dried at 80 ^oC for 24 hrs and the composite samples were labeled as 1:1GCN, 1:2GCN and 1:4GCN.

2. 2. 4. Synthesis of g-C_3N_4/MnO_2 Nano Hybrid Material

MnO_2 nano needles grown g-C_3N_4 hybrid material was prepared by the oxidation reduction reaction between Mn^{2+} ion and Mn^{7+} ions.[3] In a typical method 200 mg of as prepared g-C_3N_4 was dispersed in 40 ml of deionised water containing 40 mM $MnSO_4$ by a probe sonicator. The suspension was kept at a temperature of 80 ^oC for 30 minutes under magnetic stirring inorder to infuse Mn^{2+} ions on the surface of g-C_3N_4 layers. 150 ml of 33 mM $KMnO_4$ solution which is kept at a temperature of 80 ^oC was added carefully to the above suspension under stirring condition. The stirring was continued for another 20 minutes by keeping the suspension at a temperature of 80 ^oC, the product obtained was washed with water, ethanol and dried in an air oven at a temperature of 100 ^oC for 8 hours.

2. 2. 5. Synthesis of g-C_3N_4/SnO_2 Nano Hybrid Material

g-C_3N_4/SnO_2 composite sample was prepared by the chemical reduction method.[4] 200 mg of synthesized g-C_3N_4 was dispersed in deionised water by using an ultrasonicator for 20 minutes. 1 ml of 38 % HCl was added to the above suspension just before the addition of 0.72 g tin (II) chloride (g-C_3N_4:SnO_2 = 1:2). The sonication was continued for another 10 minutes and the solution was magnetically stirred at normal temperature for 2 hours. The product obtained was washed with water, ethanol and dried in an air oven at 100 ^oC for 8 hours. The dried powder sample was calcined at 350 ^oC/2 hrs for the development of crystalline SnO_2 phase on g-C_3N_4.

2. 2. 6. Synthesis of g-C_3N_4/CuO and g-C_3N_4/Co_3O_4 Nanohybrid Structures

Transition metal oxide (MO) anchored g-C_3N_4 such as g-C_3N_4/Co_3O_4, g-C_3N_4/CuO nano hybrid material with g-C_3N_4:MO weight ratio of 7:3 was prepared by simple hydrothermal method. In this method 0.06 g g-C_3N_4 was weighed out separately in two beakers and dispersed in 50 ml distilled water by ultrasonication. 0.045 g $CuNO_3$ and 0.06 g $CoNO_3$ was weighed out separately in to the above suspension. The sonication was continued for another 30 minutes. NH_4OH solution was carefully added to the suspension and the pH was adjusted to 9. The precipitate was then transferred into a 100 ml stainless steel autoclave and kept a temperature of 180 ^oC for 12 hours. The product obtained was washed with distilled water, dried and calcined at a temperature of 300 ^oC for 2 hours.

2. 2. 7. Synthesis of Fe_2O_3 Nanoparticles from discarded Razor Blades

The iron oxide nanoparticles were synthesized from the iron salt solution obtained by the dissolution of razor blades. Discarded razor blades were collected and cleaned using acetone and then cut into pieces. In a typical synthesis procedure, nearly 5 g of cleaned razor blades were used. The razor blades were first dissolved in minimum quantity of hot Conc. HCl in the presence of a pinch of Zn powder. After dissolution, the solution was filtered to remove the Zn powder. The razor blade solution was made up to 100 ml in a standard flask with distilled water. The solution was then transferred to a round bottom flask, and pH was raised to 8 by dropwise addition of NH_4OH from a burette till the pH of the medium reaches 9. The iron hydroxide formed was filtered, dried in an oven and then heated at 300 °C for 2 hours in a muffle furnace to obtain iron oxide nanocrystals (Sample code FO). The razor blade steel actually consists of 12-14 % of chromium and traces of other elements in addition to iron. However only Fe get precipitated as its hydroxide while adding NH_4OH up to a pH of 9, since at this particular pH the ionic product of $Fe(OH)_2$ exceeds its solubility product and the chromium ions remains in solution (precipitation of $Cr(OH)_3$ occurs at pH 11).[5]

2. 2. 8. Preparation of Fe_2O_3@Carbon Nano-hybrid Structures

The carbon-coated iron oxide nanoparticles were prepared by hydrothermal carbonization of glucose.[6] 5 g of glucose was dissolved in 50 ml distilled water and 1 g of iron oxide nanoparticles were

dispersed in the glucose solution and mixed by continuous stirring for 1 hour. The dispersion was then transferred to a 100 ml stainless steel autoclave with teflon lining. The autoclave was then heated to 180 ^{o}C for 12 hours. After carbonization, the autoclave was cooled, and the black colored precipitate (CFO) was separated from water by centrifugation, washed multiple times by distilled water and dried in a hot air oven.

2. 2. 9. Synthesis of TiO_2-CdS Heterojunction Photocatalyst

CdS nanoparticles were synthesized by hydrothermal method. In a typical procedure 0.1 M cadmium nitrate was dissolved in 50 ml deionised water, then 0.3 M aqueous thiourea solution was added to the above solution and stirring continued for another 30 minutes. The homogeneous solution obtained was transferred to 100 ml teflon lined stainless steel autoclave and kept at a temperature of 150 °C /12hrs. The obtained precipitate was washed with water and dried at a temperature of 80 °C /12hrs.

TiO_2-CdS nano composites with different weight percentage of CdS such as 0, 1, 5, and 10% were prepared by hydrothermal method and the samples were labelled as TiO_2, TiO_2-CdS1, TiO_2-CdS5 and TiO_2-CdS10. For the synthesis of hybrid system, calculated amount of CdS nano particles were ultrasonicated in 1:1 water: ethanol mixture to get a uniform dispersion. The above dispersion was added carefully to 0.4 M titanium tertiary butoxide solution in 50 ml isopropyl alcohol. The obtained sol was vigorously stirred for 4 hours and transferred to 100 ml stainless steel autoclave and kept at a temperature of 180 °C/ 12 hrs.

The precipitate so obtained was washed several times with ethanol acetone mixture to remove excess organic solvents and the samples were calcined at 300 °C/ 2 hrs which resulted in the formation of nano crystalline TiO_2-CdS heterostructures. Bare TiO_2 nano particles (TiO_2-CdS0) were also synthesized by a similar method without the addition of CdS for the comparative study.

2. 3. Energy storage Application as Supercapacitor Electrode

The synthesized semiconductor nanomaterial hybrid systems such as g-C_3N_4/TNT, g-C_3N_4/MnO_2, g-C_3N_4/SnO_2, g-C_3N_4/Co_3O_4, g-C_3N_4/CuO and Fe_2O_3@C were employed as electrode material in symmetrical supercapacitor devices. A detailed procedure for the electrode fabrication and the electrochemical measurements were explained as follows.

2. 3. 1. Electrode preparation and Electrochemical measurements

A homogeneous mixture of active materials with polytetrafluoroethylene (PTFE) binder in the mass ratio of 95:5 in ethanol was coated onto the carbon cloth (ELAT, Nuvant systems Inc.) substrate (Area= 1 cm × 1 cm) by drop casting and then dried in a vacuum oven at 100 ^oC overnight to remove moisture and residual hydrocarbons. Two symmetrical electrodes loaded with approximately 1 mg of the active materials in each, were separated by a polymer film (Celgard 3400) dipped in 2 M KOH electrolyte solution **(Scheme 2. 1)**. The complete capacitor assembly was then sandwiched in the electrochemical test cells (ECC-Std- EL-CELL). Since the two-electrode method gives a more reliable result for such material,[7] the

performance of the electrodes for supercapacitor application was measured in two-electrode cells by cyclic voltametry (CV), galvanostatic charge-discharge and electrochemical impedance spectroscopy (EIS) using an electrochemical workstation (VMP3 Biologic).

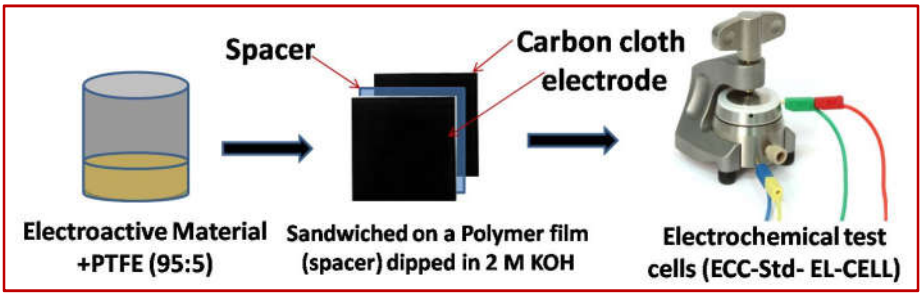

Scheme 2. 1. Schematic represenation of electrode preparation and electrochemical measurements.

The specific capacitance value of the devices were calculated from Cyclic Voltammetry (CV) and Galvanostatic Charge-Discharge (GCD) profiles using the equation,

$$\checkmark \quad Csp = \frac{A}{fVm} \tag{2.1}$$

$$\checkmark \quad Csp = \frac{2I}{m}\left(\frac{\Delta t}{\Delta v}\right) \tag{2.2}$$

respectively. where A is the absolute area of the CV curve, f is the scan rate, V is the voltage window, m is the mass of active material in a single electrode I is the discharge current, Δt is the discharge time and Δv is the cell potential range after IR drop.

2. 4. Environmental Application as Photocatalyst

TiO_2-CdS nanocomposites were used as heterojunction photocatalyst material for the sunlight driven photocatalytic studies. Detailed procedure adopted for the photocatalytic application studies are given below.

2. 4. 1. Photocatalytic Studies.

Methyl orange (MO) was taken as the target dye for the comparison of the photocatalytic efficiency of different catalysts under investigation. In the typical experiment 0.05 g (1g/litre) of the TiO_2-CdS heterojunction photo catalyst was dispersed in 50 ml of 10^{-4} M, target solution. The reaction mixture was stirred in dark for 30 minutes to establish adsorption-desorption equilibrium between the catalyst and organic molecule. The mixture was placed under sunlight and 5 ml aliquots were withdrawn at regular time intervals and centrifugation was carried out to remove the catalyst before absorption studies. UV visible absorption spectrometer was used to determine the concentration of the dye solution before and after exposure to sunlight. Intensity of sunlight was measured using Lutron, LX-107 HA lux meter and the intensity was found to be 60000-70000 Lux.[8]

2. 5. Environmental Application as Oil-Spill Adsorbents

Fe_2O_3@carbon composite nanoparticles were used as a magnetically separable adsorbent material for the removal of oil-spills from water. Procedure adopted for oil removal studies are given as follows:

2. 5. 1. Oil removal studies

The oil removal efficiency of the material was tested by weighing method. An artificial oil-spill was created in the laboratory by adding 2 g of the commercial engine oil in 10 ml water taken in a petri dish. 0.5 g of the adsorbent material was accurately weighed and smeared on the surface of the spill. Since the sorbent material, Fe_2O_3@carbon is magnetically separable, the oil adsorbed sorbent was recovered using a permanent magnet and dried overnight in an air oven at 100 °C to remove adsorbed water. The oil-retention capacity of the sorbent material was then determined by the relation;

- ✓ $k = (b-a)/a$ (2. 3)

Where 'a' is the weight of the adsorbent material smeared on the surface of the oil-spill and 'b' is the weight of the oil adsorbed material removed from the spill after drying.[9,10]

2. 6. Characterization Techniques

2. 6. 1. X-ray Diffraction (XRD)

XRD is the most powerful technique primarily employed for the determination of crystalline phase of the solid state material. It can also provide information about percentage of phase composition, lattice size, crystallinity, lattice defects and crystallite size.[11]

A crystal consists of very large number of atoms arranged in a regular repetitive manner and every atom in a crystal scatters the beam of X-

ray incident upon it. The condition for X-ray diffraction or constructive interference from crystal is given by Bragg equation.

$$\checkmark \quad 2d \sin\theta = n\lambda \qquad (2.4)$$

Where 'λ' is the wavelength of X-rays, 'n' is an integer called order reflection and 'd' is the inter planar spacing between the two lattice planes. The scattering power of an atom depends on the number of electrons thus the intensity of diffracted beam depends on the nature of atom and the location of the atom in the unit cell whereas the position of diffracted beam depends on the size and shape of the unit cell. Thus X-ray diffraction spectrum is the finger print of solid state materials and the crystalline phases in a mixture can be identified separately. The diffraction patterns obtained from the machine is usually compared with ICDD data file (International Centre for Diffraction Data) for the determination of the crystal structure of the material. XRD technique is also used to determine the crystallite size (t) of the material from the full width at half maximum (β) of the diffraction peaks by using Debye scherrer equation as:

$$\checkmark \quad Crystallite\ size\ (t) = 0.9\lambda/\beta cos\theta \qquad (2.5)$$

The broad XRD peaks observed for nanocrystalline sample is due to the fact that in nanomaterials very large number of planes are oriented randomly in all directions, thus incident rays that diffracts at angle slightly different from Bragg angle (θ) also undergo partial constructive interference.

The powder X-ray diffraction patterns of the samples were analyzed using CuKα radiation on a Bruker X-ray diffractometer.

2. 6. 2. Fourier Transform Infrared Spectroscopy (FTIR)

FTIR is the most common spectroscopic technique that provides wealth of information about the chemical structure of the molecule.[12] IR absorption spectrum is generally plotted as wave number or wavelength along the x axis and percentage transmittance or absorption intensity along the y axis. The IR region of the electromagnetic spectrum spans the region 13,000 to 10 cm^{-1} in terms of wave number. Above the temperature of absolute zero all the atomic bonds in molecules are under constant vibration. When the frequency of the bond vibration matches with the frequency of incident radiation, a quantized absorption of the radiation take place and a corresponding spectrum will be generated. Since the chemical nature of the molecule is different, no two molecules produce similar IR spectrum. FTIR spectrometers have developed as an alternative for dispersive spectroscopy owing to its sensitivity and rapid scan rate. Instead of scanning all the frequencies individually FTIR scans all the frequencies simultaneously by employing a simple optical design called Michelson interferometer.

FTIR spectral analysis was carried out using Jasco-FT/IR-4100 spectrometer. The samples were pelletised after mixing with KBr powder and the measurements were done under transmission mode in the range of 4000-400 cm^{-1}.

2. 6. 3. Raman Spectroscopy

Raman spectroscopy is non-destructive and highly versatile analysis tool in the hand of researchers and it has been applied in structural and qualitative analysis of the molecule.[13,14] It is based on the inelastic scattering of light from a molecule called Raman effect discovered by C. V. Raman and K. F. Krishnan in the year 1928.

When a light radiation with energy, hγ interacts with molecule, the radiations are scattered either elastically or in-elastically. In elastic scattering intensity of scattered radiation is equal to the intensity of incident light such type of scattering is called Rayleigh scattering. However in inelastic scattering intensity of scattered radiation is different (usually lower) from that of the incident radiation. This process of inelastic scatter is termed the Raman Effect which can occur with a change in vibrational, rotational or electronic energy of a molecule. If the incident radiation interacts with molecule in the ground vibrational state, part of the incident energy is absorbed by the molecule thus the frequency of scattered radiation reduces this change in frequency is called Stokes shift. Anti stoke shift arises when the incident radiation interact with vibrationally excited molecule; in such cases the incident radiation absorb energy from the molecule resulted in a radiation with frequency greater than that of the incident radiation. The Anti stokes shifted Raman spectrum intensity is always weaker than the Stokes-shifted spectrum. However, at room temperature it is strong enough to determine the vibrational properties at frequencies less than about 1500 cm^{-1}.

Raman spectra of all the samples were recorded on a Thermo scientific DXR 532 nm laser FT Raman microscope.

2. 6. 4. X-ray Photoelectron Spectroscopy (XPS)

XPS is one of the widely used surface analytical methods used for determining the elemental compositions and chemical state of solid materials and thin films.[15] The technique is based on the principle of photoelectric effect and it uses soft X-rays (1-15 keV) to excite core and valance electrons from the surface of the material. The intensity of these excited photoelectrons are detected and reported as a function of binding energy in XPS spectrum. In most cases the technique is non-destructive and it gives information about the top surface layer (~10 nm) of the material. The spectral peaks are denoted on the basis of angular and spin quantum numbers of the core level from which the photoelectron is ejected. The total of this angular momentum is also included in the signal notation. For example in $Ti2p_{3/2}$ signal J+S=1+1/2=3/2. In the excitation process when the surface is irradiated with X-rays having energy hr the core level electrons are ejected with a kinetic energy (KEe) by overcoming their binding energy (BEe) which can be expressed as

- ✓ $KE_e = BE_e + \phi$ (2. 6)

Where ϕ the work function of the electron represents the minimum amount of energy needed for the photoelectron electron to escape from the surface. Binding energy can be determined by measuring the kinetic energy of the photoelectron and the binding energy of photoelectron is plotted against their intensity in XPS spectra. Binding

energy of an electron depends on the chemical environment and energy state of the atom. Thus any change in the chemical environment or atomic state results in the corresponding changes in the spectra this change in binding energy is called chemical shift.

The photo excitation of the neutral atom results in other secondary emissions either a valance electron emission or photon emission. In this two competitive emission process former is called X-ray fluorescence and the latter is Auger emission. Fluorescence emission occurs when high energy X-rays are used and Auger emission take place when low energy X-ray radiations are used for analysis. However in conventional XPS instrument low energy MgKα and AlKα radiation are used to avoid the contribution from fluorescence. On the other hand Auger emissions by X-rays are considered as separate branch, X-ray excited auger electron spectroscopy (XAES).

X-ray photoelectron spectroscopy (XPS) analysis was carried out from Ultra axis Kratos Analytical, U. K, XPS instrument with an Al K_{α} as X-ray source.

2. 6. 5. Scanning Electron Microscopy (SEM)

SEM is a used to characterize the surface morphology and the chemical composition of the material.[16] The resolution power of optical microscope is limited to around 0.2 μm since visible light is used for imaging. However 2-4 magnitude higher resolution can be achieved in electron microscopy due to much smaller wavelength of electrons beams used for imaging. In SEM analysis sample surface is exposed to high energy electron beams and the sample surface

generates back scattered electrons (elastically scattered), secondary electrons (inelastically scattered) and X-rays. SEM used these ejected radiations for the surface morphology analysis and compositional analysis of the sample.

Backscattered electrons are of higher energy than the secondary electrons and its intensity is related to the atomic number of the elements in the specimen. The area of the specimen containing heavy atoms appears bright when back scattered electrons are analyzing thus it gives information about the chemical compositional difference in the material. Secondary electrons are ejected from the valance shell of the atoms in the specimen. These electrons ejected from the deep level of the specimens are absorbed by the sample and the secondary electrons from the surface of the samples only give information about the specimen. When the incident electrons knock out the inner shell electrons of the atom, these electron vacancies will be occupied by the electrons in the next higher orbits and this energy difference between the outer shell electrons and inner shell electrons are emitted as X-rays. The energy of this X-rays is the characteristics of the individual elements and these are used for the elemental analysis of the material by energy dispersive method (EDS).

Surface morphology of the samples was analyzed from Carl-Zeiss Gemini-300 field emission scanning electron microscopy (FESEM).

2. 6. 6. Transmission electron microscopy (TEM)

TEM is a versatile instrument used for analyzing the micro structural image of the material with high magnification of up to 10 lakhs times and high resolution of up to 1 nm. [16] It also gives information about the crystal lattice parameters and chemical composition through electron diffraction and energy dispersive analysis respectively. In TEM beam of electrons were accelerated through a potential of 10 to 300 kilovolts (kV) and focused on an ultra thin transparent specimen by a strong magnetic lens and the transmitted electrons were detected. TEM can provide information about the crystallinity of the material since the crystal planes acts as diffraction grating and these diffracted electron beams produces interference patterns either in the forms of dots or rings. Undiffracted beam produces central spot and those diffracted at Braggs angle produces a spot. The difference between these transmitted and diffracted beams is inversely related to the lattice spacing in the material. If the material is microcrystalline the diffraction pattern consists of series concentric lines instead of spots in crystalline samples.

TEM images of the materials were recorded using JEOL/JEM 2100 transmission electron microscope.

2. 6. 7. Photoluminescence Spectroscopy (PL)

PL spectroscopy is a powerful technique to determine the optoelectronic properties of semiconductor materials.[17] When the material is excited with energy greater than the optical band gap of the material, enormous number of excitones are produced and by

observing the emission spectra, the fate of photogenerated electrons and holes can be determined. The strong PL emission spectra indicate the increased rate of electron hole recombination and the probability of these excitons to participate in chemical reaction is comparably less. However in weak PL spectra the rate of recombination is very small and these excitons are rather efficient to carry out chemical process. Detailed information regarding the charge recombination mechanism and the optical band gap of the material can be deducted from the PL spectral data. Moreover, it gives an idea about the defect in material and the impurity level present in the sample. PL spectra basically observe the radiative transition generated from the excited sample. However, it is unsuccessful to determine the properties at the deep centres where it gives a broad spectrum due to the presence of strong phonon coupling.

Photoluminescence measurements were carried out using Perkin Elmer LS55 fluorescence spectrometer equipped with pulsed Xenon source.

2. 6. 8. UV-Visible Absorption Spectroscopy

UV-Visible Absorption Spectroscopy is the most versatile analytical instrument almost entirely used in the laboratory for the quantitative determination of the compound present in the homogeneous liquid solution. It uses ultraviolet (200-400nm) and visible region (400-800nm) [18,19] of the electromagnetic spectrum. These radiation causes excitation of the electrons from lower electronic levels to the higher electronic states of the molecules. UV-Visible absorption spectrum (plot of degree of absorption *vs* wavelength of radiation absorbed)

usually consists of few humps rather than sharp lines due the changes in the vibration energy levels associated with each electronic energy states of the molecules. The basic principle of the quantitative determination of the compound in solution is Beer-Lambert Law. It states that when a monochromatic radiation having intensity (I_o) passes through a solution in a cuvette, the intensity of the transmitted radiation (I) depend on the concentration (C) and the thickness (L) of the solution. I/I_o is called Transmittance and which is mathematically related to Absorbance (A) or the optical density by the relation:

$$\checkmark Absorbance\ A = \log\frac{Io}{I} = \varepsilon CL \qquad (2.\ 7)$$

Where ε is a constant termed as molar absorption coefficient which depends only on the nature of the molecule and wavelength of the radiation.

Diffuse Reflectance Spectroscopy: UV-Visible diffuse reflectance is a spectroscopic technique used to determine the electronic band structure of crystalline semiconducting metal oxides. Optical and the electronic properties of the materials are directly related primarily on the electronic band gap (E_g) of the material. Thus the band gap engineering is an important aspect to develop materials with tailor made properties. When the powdered crystalline sample is exposed to light radiation some portion of the light gets reflected and the remaining enters into the bulk sample and diffuse. The measure of diffuse reflected light at different wavelength gives diffuse reflectance spectrum and the reflection data were converted to absorption

coefficient value (α) according to $(1\text{-}R)^2/2R$. The band gap energy of the samples was calculated from the following Tauc equation:

$$\checkmark(ahr)^n = A(hr - E_g) \quad (2.\ 8)$$

Where A is a constant, hr is the light energy, E_g is the optical band gap energy, n=0.5 and 2 for indirect and direct bandgap semiconductors respectively. The plot of $(ahr)^n$ against hr should be a straight line above the optical absorption edge. The band gap energy of the material can be calculated by extrapolating the linear region of the Tauc plot to abscissa axis where the absorption coefficient value is zero for Eg=hr.

UV visible absorption spectral studies were carried out on a Jasco-V-550-UV/VIS spectrophotometer.

2. 6. 9. BET Surface area analysis

Gas adsorption measurements on the surface of solid materials were widely used for the determination of surface area of catalysts and supercapacitor electodes.[20,21] BET-N_2 gas adsorption studies got major attention in the area of determining the surface area, and pore size distribution of the solid materials. BET theory is an extension of Langmuir monolayer adsorption theory. In this method a known quantity of gas is admitted to confined volume of the adsorbent which is kept at a constant temperature. As the adsorption takes place, pressure in the confined volume falls until equilibrium is attained. The relation between amount of gas adsorbed at gas solid interface and the equilibrium pressure of the gas is called adsorption isotherm. BET equation can be written as

$$\checkmark \frac{P}{Vtotal}(Po - P) = \left[\frac{1}{Vmono}C\right] + \left[\frac{C-1}{Vmono}C\right] + \left(\frac{P}{Po}\right) \qquad (2.\ 9)$$

Where $Vtotal$ is the volume of the gas adsorbed at pressure P and $Vmono$ is the volume of the gas adsorbed when monolayer adsorption is completed. Po is the saturation pressure of the gas molecule and C is a constant related to the enthalpy of adsorption in the monolayer. According to BET theory the plot of $\frac{P}{Vtotal}(Po - P)$ against $\frac{P}{Po}$ should be a straight line with intercept $I = \frac{1}{Vm}C$ and slope $S = \frac{C-1}{Vmono}C$. Thus from the slope and intercept the value of $Vmono$ and C can be evaluated from this the specific surface area of the solid adsorbent can be calculated by the equation $S = Vmono\ Na/m \times 22400$ m^2g^{-1}. Where Na is Avogadro constant, m is the mass of test powder in grams, 22400 is the volume capacity occupied by 1 mole of gas at STP.

BET surface area measurements (N_2 adsorption) of the samples were done by Micromeritics Tristar 2 USA surface area and porosity analyzer after degassing at 200 °C for 2 hours.

2. 6. 10. Cyclic Voltametry (CV)

CV is a powerful method for characterizing the electrochemical performance of an electrode material.[22,23] It consists of a working electrode immersed in an electroactive solution, the potential of this working electrode is cycled at a constant sweep rate and measuring the resulting current as a function of applied potential. In cyclic voltametry potential difference is applied across working electrode and reference electrode where as current is measured across working electrode and

counter electrode. The plot of current generated at the working electrode (vertical axis) *vs* the applied potential (horizontal axis) is called cyclic voltammogram. The potential is selected to cause some redox reactions in the electrode electrolyte interface. The current taken out from the CV is arises due to this redox reaction either in the form of faradaic reaction or electrical double layer charging. The potential of the working electrode is controlled by using a saturated calomel electrode (SCE) or silver/silver chloride electrode as the reference electrode. The applied potential or the excitation signal in CV is a linear potential scan with triangular wave form.

In the present research work the electrochemical performance of the nanohybrid materials for supercapacitor electrode application was measured in two electrode configuration from an electrochemical workstation (VMP3 Biologic).

References

1. S. Panneri, P. Ganguly, M. Mohan, B. N. Nair, A. A. P. Mohamed, K. G Warrier, U. S. Hareesh, *ACS Sustain. Chem. Eng*., 2017, 5, 1610.

2. B. Vijayan, N. M. Dimitrijevic, T. Rajh, K. Gray, *J. Phys. Chem. C*, 2010, 114, 12994.

3. R. B. Rakhi, D. Cha, W. Chen, H. N. Alshareef, *J. Phys. Chem. C*, 2011, 115,14392.

4. A. L. M. Reddy, S. Ramaprabhu, *J. Phys. Chem. C*, 2007, 111, 7727.

5. A. I Vogel, *A Text-Book of Quantitative Inorganic Analysis*-Theory And Practice. Longmans, Green and Co. London, 2013, 437.

6. M. Sevilla, A. B. Fuertes, *Carbon*, 2009, 47, 2281.

7. V. Khomenko, E. Frackowiak, F. Beguin, *Electrochim. Acta*, 2005, 50, 2499.

8. S. G. Ullattil, P. Periyat, *Nanoscale*, 2015, 7, 19184.

9. K. G. Raj, P. A. Joy, *Journal of environmental chemical engineering*. 2015, 3, 2068.

10. P. Thanikaivelan, N. T. Narayanan, B. K. Pradhan, P.M. Ajayan, *Sci. Rep*., 2012, 2,1.

11. B. D. Cullity, J. W. Weymouth, *Am. J. Phys*., 1957, 25, 394.

12. R. D. Waldron, *Phys. Rev*., 1955, 99, 1727.

13. R. Fagan, D. W. Synnott, D. E. McCormack, S. C Pillai, *Appl. Surf. Sci*., 2016, 371, 447.

14. T. Ohsaka, F. Izumi, Y. Fujiki, J. Raman. *Spectrosc*., 1978, 7, 321.

15. C. R. Brundle, A. D. Baker, *Academic Press, London*, 1978.

16. H. Ma, K. J. Shieh, T. X. Qiao, S. Cherng, *Nature and Science*, 2006, 4, 14.

17. P. Nandakumar, C. Vijayan, Y. V. Murti, *J. Appl. Phys*., 2002, 91, 1509.

18. A. E. Morales, E. S. Mora, U. Pal, *Rev. Mex. Fis*., 2007, 53, 18.

19. S. J. Hong, S. Lee, J. S. Jang, J. S. Lee, *Energy Environ. Sci*., 2011, 4, 1781.

20. K. S. Sing, *Pure Appl. Chem*., 1985, 57, 603.

21. K. Sing, *Colloids Surf. A Physicochem. Eng. Asp*., 2001, 187, 3.

22. J. J. Van Benschoten, J. Y. Lewis, W. R. Heineman, D. A. Roston, P. T. Kissinger, *J. Chem. Educ.*, 1983, 60, 772.

23. R. S. Nicholson, *Anal. Chem*., 1965, 37, 1351.

Chapter Three

TiO_2 nanotubes dispersed g-C_3N_4 nanosheets as efficient electrode materials for supercapacitors

Contents

3.1. Introduction

In the event of the glaring problem of depletion of conventional non renewable energy sources staring at us in the eye, not to mention the huge amounts of pollution caused by such sources, the question of global energy demand for a clean and abundant energy source needs to be solved and requires an imminent solution. With solar energy being at present the best promising alternative, the problem associated with this technology that of storing the energy harvested requires urgent and detailed attention. It is due to this, energy storage devices such as supercapacitors hold the present day researcher's interest. Supercapacitors store energy by incorporating high surface area electrodes and thinner dielectrics rather than chemicals, unlike conventional batteries, and has been considered as an alternative power source because of their durability and ability to charge and discharge within a short period of time.[1-3] Transition metal oxide based pseudocapacitors which store energy *via* faradaic mechanism are having superior electrochemical capacitance as compared to the carbon

based electrical double layer (EDLC) capacitor, as in the latter, the capacitance purely depends on the limited accumulation of charge at electrode-electrolyte interface.[4-9] So far reported successful candidates among the various metal oxides used in supercapacitors, like the ruthenium oxides, has the disadvantage of being expensive and are also toxic.[10] Among the low-cost transition metal oxides, TiO_2 nanotubes has shown promise in electrochemical applications recently.[5] TiO_2 holds particular interest due to its environmentally benign chemical nature, stability and low cost.[11-14] Unfortunately, specific capacitance of TiO_2 nanotube supercapacitors are very small and it drops continuously on increasing the scan rate due to its low electrochemical activity and poor conductivity.[15-17] In order to overcome these limitations, several attempts have been made by technologists to design electrodes which can possess high values of specific capacitance without compromising the electrochemical stability of the material. Universally adopted approach include coupling the metal oxide with conducting carbon based materials such as activated carbon, carbon aerogels, graphene, carbon nanotubes or by self-doping with hydrogen or Ti^{3+} ions, which has been reported to provide excellent cycle life and good electrochemical stability.[4,10,18] However, these conventional carbon materials need high processing temperature and utilize harsh chemicals. Recently graphitic carbon nitride (g-C_3N_4), a polymer of s-triazine units, has been recognized as a riveting 2D nanomaterial for diverse application due to its low cost, chemical endurance and non-toxicity.[19] The supercapacitor performance of TiO_2 nanotubes supported over g-C_3N_4 scaffold is yet unexplored. Herein we report for the first time the synthesis and supercapacitor performance of TiO_2 nanotubes (TNT) incorporated into two-dimensional g-C_3N_4.

3. 2. Results and Discussion

A schematic representation for the preparation of TiO_2 nanotubes (TNT) was described as **Scheme 3. 1**. TNT/g-C_3N_4 nanostructure was prepared from TNT and g-C_3N_4 by hydrothermal method at 100 ^oC/6 hrs.

Scheme 3. 1. Schematic representation of the synthesis of TiO_2 nanotubes (TNT)

3. 2. 1. XRD analysis

TiO_2 phase formation and the layer stacking arrangement in g-C_3N_4 were confirmed from the powder XRD patterns shown in **Figure 3. 1**. The observed peaks in **Figure 3. 1(a)** at *2θ* values 25.46, 38.0, 48.19, 54.50, 62.69, 69.94^o can be readily indexed to the (101), (004), (200), (105), (211) and (204) planes of TiO_2 (JCPDS No. 21-1272) in anatase phase (TNT). The strongest peak in the XRD patterns of g-C_3N_4 at 27.1^o (**Figure. 3. 1e**) with an interplanar distance (d) of 0.326 nm corresponding to the reflection from (002) plane is originated from the diffraction from stacking of conjugated aromatic systems. The peak at 13.1^o from (100) plane with a *d* value of 0.675 nm is due to the presence of in-planar tri-s-triazine units.[23] It is clear from the XRD analysis that the composite materials 1:1GCN, 1:2GCN and 1:4GCN in **Figure 3. 1(b), 3. 1(c) and 3. 1(d)** has both TNT and graphitic carbon

nitride phases in it and the peak at 27.1° confirms the presence of g-C_3N_4 in the composite sample and is marked as (*) in the XRD spectrum.

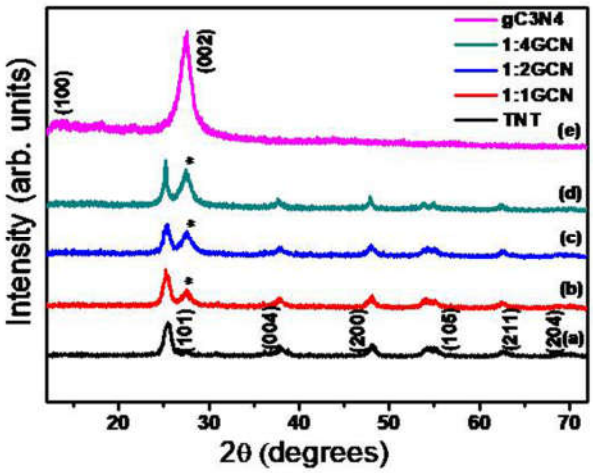

Figure 3. 1. XRD patterns of a) TNT, b) 1:1GCN c) 1:2GCN, d) 1:4GCN and e) g-C_3N_4.

3. 2. 2. FTIR Spectral analysis

Vibrational spectra of the synthesized samples were recorded (**Figure 3. 2**) to confirm the formation of TNT, g-C_3N_4 and also to analyse the interaction between the two component phases. The polymeric g-C_3N_4 sample shows several peaks in the 1200-1600 cm^{-1} region corresponding to the stretching vibrational modes of C-N heterocycles present in g-C_3N_4. The peak at 811 cm^{-1} arises from the characteristic breathing mode of s-triazine monomeric units. Broad band located around 3000-3500 cm^{-1} belongs to the N-H stretching vibrations of primary and secondary amines groups at the defect sites of aromatic ring.[24] The peak at 400-500 cm^{-1} in TNT and composite materials is

the characteristic peak of anatase TiO_2 which arises due to the stretching vibrations of Ti-O-Ti bonds.[25]

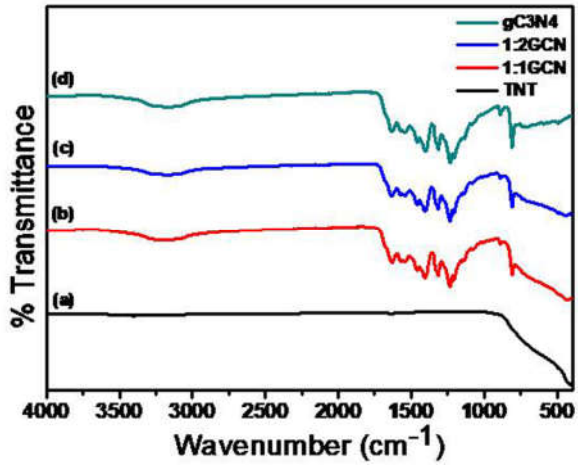

Figure 3. 2. FTIR spectra of a) TNT, b) 1:1GCN c) 1:2GCN and d) g-C_3N_4.

3. 2. 3. X-ray Photo Electron Spectroscopy (XPS)

The chemical state of the elements in the synthesized g-C_3N_4 was investigated using XPS. The survey XPS spectrum in **Figure 3. 3(a)** at 287 eV and 397 eV confirm the presence of carbon and nitrogen elements. The elemental quantification data from XPS is attached as inset in **Figure 3. 3(a)**. No other metallic or non-metallic impurities other than C and N are present in the sample indicating a high degree of purity for the synthesized g-C_3N_4. A very weak O1s peak at 530 eV is due to the surface contamination of the sample from adsorbed water molecules in the atmospheric air. The high resolution C1s spectra in **Figure 3. 3(b)** with a characteristic peak at 287.69 eV originated from the sp^2 C atom connected to N atom of N-C=N units in the aromatic ring of g-C_3N_4.[20] Low intensity peak at 284 eV and 294 eV

corresponds to C-C coordinated carbon atoms and the pi excitation in C=N bonds respectively, thus the pi excitation confirm the presence of sp^2 hybridized carbon atom in g-C_3N_4.[27] The high resolution N1s peak in Figure 3. 3(c) at 398 eV can be attributed to the –C=N bonded N atom in triazine ring. Presence of low intensity shoulder peak at 400 eV is originated from the bridging nitrogen atom in N-$(C)_3$ or N bonded with H atom. A very weak intensity peak at 403 eV can be atributed to the charging effects or positive charge localization in heterocycles and the cyano- group.[20]

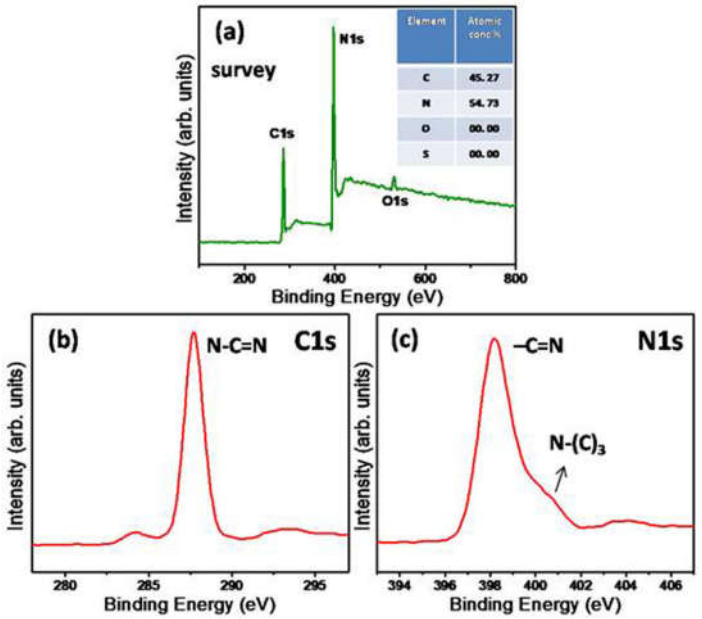

Figure 3. 3. XPS spectra of synthesized g-C_3N_4: a) The whole survey spectrum; b) C1s XPS spectrum; c) N1s XPS spectrum.

3. 2. 4. Morphology analysis

Morphology of the as synthesized TiO_2 and the composite sample 1:4GCN was characterized from a transmission electron microscope

(TEM). Electron microscopic image of TiO_2 in **Figure 3. 4(a)** exhibited a tubular structure with an average length of 18-20 nm and an average diameter of 8-10 nm. The SAED pattern of the bare TNT was also given in **Figure 3. 4(b)** which has shown concentric rings in the diffraction pattern indicating the characteristics partially crystalline nature of the nanosized samples. The synthesized 1:4GCN composite electrode sample has exhibited a uniform distribution of TiO_2 nanotubes in g-C_3N_4 matrix (**Figure 3. 4c**). It is clear from the TEM images and the SAED pattern (**Figure 3. 4d**) of the composite sample that the morphology and the crystallanity of the TiO_2 nanotubes were not disturbed while fabricating the composite samples. Moreover, the TEM confirms the formation of heterojunction between TNT and g-C_3N_4 and that the TNTs can act as spacers between the g-C_3N_4 nanosheets.

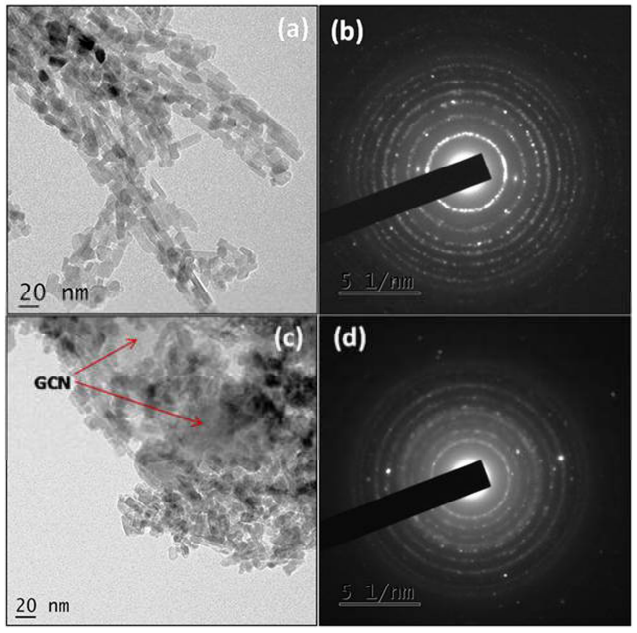

Figure 3. 4. TEM images of TNT (a), composite electrode 1:4GCN (c) and the corresponding SAED patterns (b & d)

3. 2. 5. BET-Surface area analysis

BET surface areas of the samples were determined by N_2 gas adsorption-desorption technique proposed by Brunauer, Emmett and Teller were presented in **Figure 3. 5**. All the adsorption isotherms indicates type IV curve with H3 hysteresis which are the characteristics of mesoporous material according to IUPAC classifications. BET surface area of TNT and GCN respectively are 25 and 32 m^2g^{-1}, however the composite samples show comparably higher surface area values of 35, 38 and 74 m^2g^{-1} for 1:1GCN, 1:2GCN and 1:4GCN respectively. The remarkable increase in the specific surface area for the 1:4GCN sample can be attributed to the spacer effect of TiO_2 nanotubes in 2D g-C_3N_4 network.

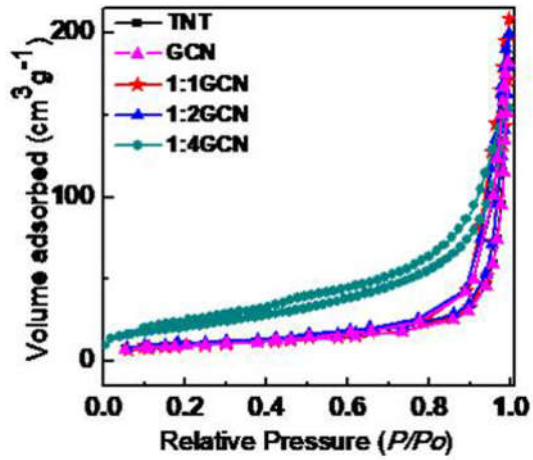

Figure 3. 5. BET N_2 adsorption isotherm of different samples.

3. 2. 6. Cyclic Voltammogram (CV)

CV is used to analyze the capacitive behavior of an electrode material. Cyclic voltammograms of TNT, GCN, 1:1GCN, 1:2GCN and 1:4GCN

composites taken at different scan rates of 5, 10, 20, 50, 100 and 200 mVs^{-1} are shown in **Figure 3. 6**. TNT have very low specific capacitance value and the narrow CV loop of TNT is due to its limited pseudo capacitive contribution from the most stable Ti^{4+} ions of TiO_2 (**Figure 3. 6a**). The GCN and the composite samples have shown nearly rectangular type CV loops (**Figure 3. 6b, 3. 6c & 3. 6d**) due to the electrical double layer nature of g-C_3N_4. The composite electrode with 1:4 ratio of TNT and GCN exhibit almost rectangular type CV (**Figure 3. 6e**) upto a scan rate of 200 mVs^{-1} indicates the characteristics of an excellent capacitance behavior. The absence of oxidation and reduction peak in the CV curve of 1:4GCN is due to the negligible pseudocapacitive contribution from TNT. The summary of the specific capacitance of the electrodes at various scan rates is shown in **Figure 3. 6(f)**. All the samples show high specific capacitance value at slow scan rate as the ions in the electrolyte get more time to diffuse into the pores of electrode material and resulted in a marked increase in the capacitance value.[27]At slower scan rate of 5 mVs^{-1}, TiO_2 nanotube exhibits a gravimetric specific capacitance (C_{sp}) of 24 Fg^{-1}. After hybridizing with g-C_3N_4 (C_{sp} of 72 Fg^{-1}) the capacitance value increased significantly. The maximum specific capacitance of 110 Fg^{-1} was obtained for 1:4GCN composite at a scan rate of 5 mVs^{-1} and the value is much higher than the individual components in the composite. In the 1:4GCN composite, due to the optimum quantity of TNT spacers in between the layers of 2D g-C_3N_4, the accessible surface area of the composite increased considerably, leading to higher specific capacitance. In 1:1GCN (38 Fg^{-1}) and 1:2GCN (60 Fg^{-1}) composites also there is an increase in the specific capacitance values due to the contribution from the EDLC behavior in g-C_3N_4 scaffold.

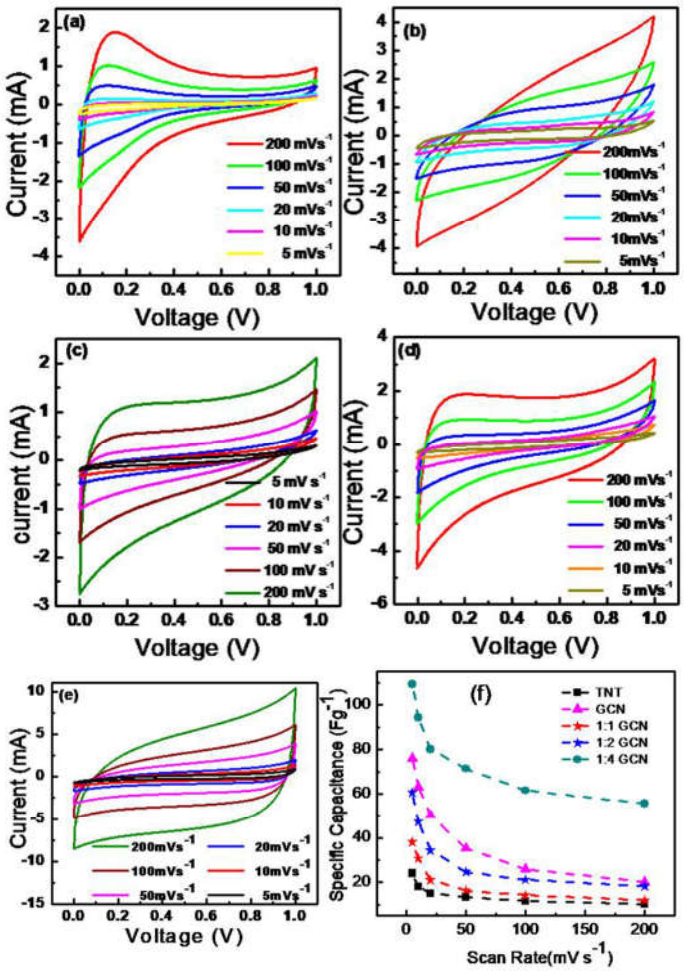

Figure 3. 6. Cyclic voltammograms of (a) TNT, (b) GCN, (c) 1:1GCN, (d) 1:2GCN and (e) 1:4GCN composite at different scan rates (f) Variation of specific capacitance as a function of scan rate.

3. 2. 7. Galvanostatic Charge-discharge (CD) curves

CD curve of the super capacitors measured at a constant current density of 1 Ag^{-1} and potential range of 0 to +1 V is given in **Figure 3. 7(a)**. TNT, GCN, the composite electrodes 1:1GCN and 1:2GCN showed a very sharp charge-discharge curve, however in 1:4GCN

electrodes the charge discharge time increases considerably. In 1:4GCN, the enhancement in electrochemical properties may be due to the spacer effect of 1D TiO_2 in between the layers of 2D g-C_3N_4 which can provide an excellent platform for charge transport. From the CD curves, the specific capacitance values for symmetric supercapacitors based on TNT, GCN, 1:1GCN, 1:2GCN, 1:4GCN electrodes were calculated as 15.02, 50.22, 21.28, 33.74 and 79.62 Fg^{-1} respectively and the results are in consistent with the values obtained from CV measurements. At a constant energy density of 1 Ag^{-1} the symmetric supercapacitors based on TNT, GCN, 1:1GCN, 1:2GCN, 1:4GCN electrodes exhibited current densities of 2.08, 6.97, 2.96, 4.66 and 11.11 $Whkg^{-1}$ respectively at a power density of 1 $KWkg^{-1}$. The cycling stability performance of 1:4GCN based best performing symmetric supercapacitor was conducted at a constant current density of 5 Ag^{-1}. The device retained nearly 92% of its maximum capacitance even after 9000 consecutive charge-discharge cycles (**Figure 3. 7b**).

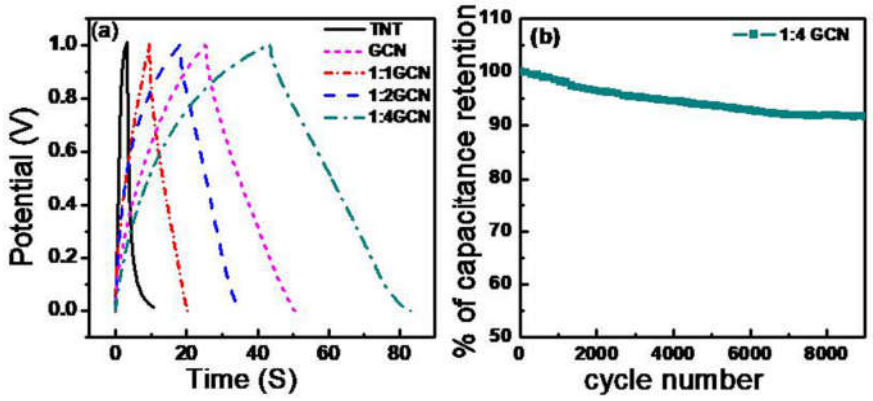

Figure 3. 7. (a) CD curves of TNT, GCN, 1:1GCN, 1:2GCN and 1:4GCN supercapacitor electrodes at a constant current density of 1 Ag^{-1}. (b) Cycling performance of 1: 4 GCN at a current density of 5 Ag^{-1}

3. 2. 8. Electrochemical Impedance Spectroscopy (EIS)

To confirm the improved charge transport behavior the electrochemical responses (Nyquist plot) of the TNT-GCN composite was compared with bare TNT and are depicted in **Figure 3. 8.** Spectra are measured with sinusoidal signal of 5 mV at a dc bias of 0 V over the frequency range of 100 kHz to 1 MHz. EIS spectrum generally consists of three parts. At low-frequency region impedance is controlled by the diffusion of ions from the bulk of the solution to the electrode surface (Warburg diffusion). Arc radius of the plot at high frequency denotes the charge transfer resistance (R_{ct}) at the vicinity of solid electrode. Equivalent series resistance (*ESR*) at high frequency region arises due the contribution from electrolytic solution resistance, contact resistance at electrode-electrolyte interface and the characteristic resistance of the active ions.[27] Inclination of the warburg line to the imaginary vertical axis at low frequncy indictes the lower diffusion resistance of the elctrolyte ion which is the charactarestic feature of an ideal capacitor.[28] In the present investigation warburg line of EIS of TNT is away from the vertical line however on hybridising it with conducting scaffold the inclination is more towards the vertical axis and the composite 1:2GCN and 1:4GCN shows almost vertical line behaviour at low frequncy with maximum capacitance value.[4]

The Arc radius (R_{ct}) of TNT-GCN composite is reduced considerably when TNT is embedded in the matrix of g-C_3N_4. Smaller arc radius indicates the faster electron transport rate at the interface in composite electrode due to the formation of nano structured network which leads to the more effective charge separation.[4,25]

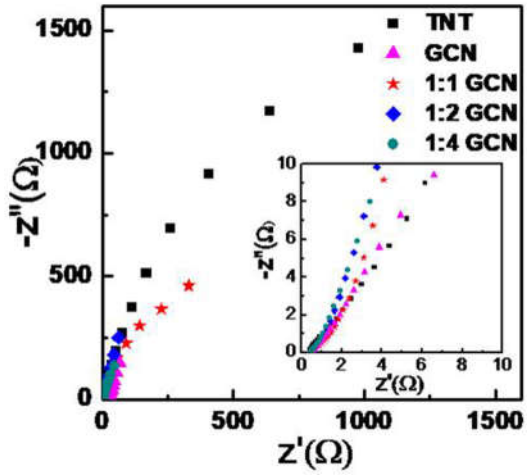

Figure 3. 8. Nyquist plots for TNT, GCN, 1:1GCN, 1:2GCN, 1:4GCN composites based supercapacitor devices at dc bias of 0 V with sinusoidal signal of 5 mV over the frequency range from 100 kHz and 1 MHz.

3. 3. Conclusions

Anatase TiO_2 (TNT) supported over g-C_3N_4 was fabricated by a simple hydrothermal method. TNT and g-C_3N_4 were prepared separately by alkaline hydrothermal method and self-polymerization method respectively. The electrochemical performance of TNT and GCN was found to have improved substantially by incorporating a g-C_3N_4 matrix. Among the various composite samples prepared **1:4** weight ratio of TiO_2/g-C_3N_4 has shown a maximum specific capacitance of 110 Fg^{-1} due to the spacer effect of the 1-D TiO_2 in 2D g-C_3N_4. The present work will be helpful to further develop supercapacitor electrode materials based on economically and environmentally benign TiO_2 based nano hetero structures.

References

1. Q. Qu, S. Yang, X. Feng, *Adv Mater*, 2011, 23, 5574.
2. H. Chen, T. N. Cong, W. Yang, C. Tan, Y. Li, Y. Ding, *Prog. Nat. Sci*., 2009, 19, 291.
3. G. Wang, L. Zhang, J. Zhang, *Chem. Soc. Rev*., 2012, 41, 797.
4. R. B. Rakhi, H. N. Alshareef, *J. Power Sources*, 2011, 196, 8858.
5. X. Lu, G. Wang, T. Zhai, M. Yu, J. Gan, Y. Tong, Y. Li, *Nano Lett*., 2012, 12, 1690.
6. C. C. Hu, K. H. Chang, M. C. Lin, Y. T. Wu, *Nano Lett*., 2006, 6, 2690.
7. J. W. Lee, T. Ahn, J. H. Kim, J. M. Ko, J. D. Kim, *Electrochim. Acta*, 2011, 56, 4849.
8. X. Xia, J. Tu, Y. Mai, X. Wang, C. Gu, X. Zhao, *J. Mater. Chem*., 2011, 21, 9319.
9. Q. Qu, P. Zhang, B. Wang, Y. Chen, S. Tian, Y. Wu, R. Holze, *J. Phys. Chem. C*, 2009, 113, 14020.
10. Y. H. Lin, T. Y. Wei, H. C. Chien, S. Y. Lu, *Adv. Energy Mater*., 2011, 1, 901.
11. H. Wu, D. Li, X. Zhu, C. Yang, D. Liu, X. Chen, Y. Song, L. Lu, *Electrochim. Acta*, 2014, 116, 129.
12. G. Wang, Z. Y. Liu, J. N. Wu, Q. Lu, *Mater. Lett*., 2012, 71, 120.
13. M. Salari, S. H. Aboutalebi, K. Konstantinov, H. K. Liu, Phys. *Chem. Chem. Phys*., 2011, 13, 5038.
14. B. Chen, J. Hou, K. Lu, *Langmuir*, 2013, 29, 5911.
15. M. Yu, Y. Zeng, C. Zhang, X. Lu, C. Zeng, C. Yao, Y. Yang, Y. Tong, *Nanoscale*, 2013, 5, 10806.

16. C. Xiang, M. Li, M. Zhi, A. Manivannan, N. Wu, *J. Mater. Chem*., 2012, 22, 19161.

17. Y. Luo, D. Kong, J. Luo, S. Chen, D. Zhang, K. Qiu, X. Qi, H. Zhang, C. M. Li, T. Yu, *RSC Adv*., 2013, 3, 14413.

18. H. Zhou, Y. Zhang, *J. Phys. Chem. C*, 2014, 118, 5626.

19. A. Thomas, A. Fischer, F. Goettmann, M. Antonietti, J.O. Mueller, R. Schloegl, J. M. Carlsson, *J. Matter. Chem*., 2008, 18, 4893.

20. V. Khomenko, E. Frackowiak, F. Beguin, *Electrochim. Acta*, 2005, 50, 2499.

21. F. Dong, L. Wu, Y. Sun, M. Fu, Z. Wu, S. C. Lee, *J. Mater. Chem*., 2011, 21, 15171.

22. G. Liao, S. Chen, X. Quan, H. Yu, H. Zhao, *J. Mater. Chem*., 2012, 22, 2721.

23. S. C. Pillai, P. Periyat, R. George, D. E. McCormack, M. K. Seery, H. Hayden, S. J. Hinder, *J. Phys. Chem. C*, 2007, 111, 1605.

24. A. P. Dementjev, A. De Graaf, M. C. M. Van de Sanden, K. I. Maslakov, A. V. Naumkin, A. A. Serov, *Diam. Relat. Mater*., 2000, 9, 1904.

25. C. Arbizzani, M. Catellani, M. Mastragostino, C. Mingazzini, *Electrochim. Acta*, 1995, 40, 1871.

26. M. S. Kim, T. W. Lee, J. H. Parka, *J. Electrochem. Soc*., 2009, 156, A584.

27. P. R. Deshmukh, S. V. Patil, R. N. Bulakhe, S. N. Pusawale, J. J. Shim, C. D. Lokhande, *Rsc Adv*., 2015, 5, 68939.

Chapter Four

One-pot synthesis of g-C_3N_4/MnO_2, g-C_3N_4/SnO_2 hybrid nanocomposites for Supercapacitor applications

Contents

4. 1. Introduction

The storage of renewable energy and its release upon demand has been a significant technological matter of contention in recent years. [1,2] Lithium-ion (Li-ion) batteries have been successful for the storage of renewable energy with high energy density.[3,4] However, the next generation hybrid vehicles, regenerative breaking system, and high power electronic devices demand high power density, large cycle life, and dramatically high safety and low cost. Supercapacitors have been widely employed as an alternative or in support of Li-ion batteries to address these demands.[5,6] Supercapacitors possess much higher power density, excellent cycle stability, a wide temperature range of performance, intrinsically safe charge storage mechanism and they can be charged and discharged in seconds.[7,8] Supercapacitors store charges either non-faradaically (EDLC capacitors) or faradaically (pseudocapacitors).[9]

Nanocarbon materials such as activated carbon, carbon nanotubes, reduced graphene oxide and graphene oxide are widely used as electrode materials in EDLC due to their high surface area and electronic conductivity.[10] Nitrogen or Sulphur doping in carbon-based materials are usually carried out to increase the wettability of the electrode surface with the electrolyte.[11,12] However, the nonmetal doping creates chemical inhomogeneity and thereby reduces the shelf life of the electrode material.

Graphitic carbon nitride (g-C_3N_4) has emerged as an alternative for purely carbon-based EDLC electrode materials owing to its low cost, chemical and mechanical stability and intrinsically high nitrogen content.[13] The lone pair of electron present in the N atom of the ring structure of g-C_3N_4 induces more polarity in the molecule and enhances the wettability and the charge carrier mobility of the material.[14]

The specific capacitance of bulk g-C_3N_4 exhibits a very low EDLC specific capacitance of 71 Fg^{-1} and 81 Fg^{-1} at a current density of 0.5 Ag^{-1} and 0.2 Ag^{-1} respectively due to its inherently low specific surface area and conductivity.[15] The reports suggested that the electrochemical properties of bulk g-C_3N_4 can be enhanced dramatically by the incorporation of pseudo capacitive phases into the matrix of bare g-C_3N_4 which will facilitate the charge transport by a synergistic effect between faradaic and non-faradaic process of electron transport.[13,14]

Transition metal oxides (TMOs) such as, RuO_2, MnO_2, V_2O_5, TiO_2, SnO_2, *etc*. and Prussian blue (PB) are widely used as the

pseudocapacitive electrode materials. Ultralong V_2O_5@conducting polypyrrole composite exhibited enhanced super capacitor performance along with superior rate capability and improved cycling stability.[16] A challenging fabrication technique was reported on the synthesis of PB and its analogues (PBA) which exhibit a high specific capacitance of 292 Fg^{-1} in the neutral Na_2SO_4 aqueous electrolyte.[17] Among the different pseudocapacitive materials MnO_2 is of particular interest due to its high electrochemical activity, environmental compatibility, low cost and abundant availability on earth. Wang *et al*. reports the latest progress in MnO_2-based nanocomposite electrodes to provide guidance for the design, manufacturing, and assembly of high-performance pseudocapacitive material for supercapacitors.[18]

Various reports are available on the synthesis and electrochemical performance studies of transition metal oxide incorporated g-C_3N_4 nanocomposite electrodes. For carbon-doped graphitic carbon nitride@MnO_2 (CCNM) composite, Shan *et al*. reported a specific capacitance of in a three-electrode system was 324 Fg^{-1} at a current density of 0.2 Ag^{-1} with capacitance retention of 80.2% after 1000 cycles.[19] In another report, the same group evaluated the electrochemical performance of single atom (K/Na) doped graphitic carbon nitride@MnO_2 electrode in three-electrode configuration.[20] Chang *et al.* reported a maximum specific capacitance of 211 Fg^{-1} at a current density of 1 Ag^{-1} in a 0.5 M Na_2SO_4 electrolyte solution for MnO_2/g-C_3N_4 nanocomposite in three electrode assembly.[21] Recently Chen *et al.* reported the synthesis of a two dimensional hybrid structure of g-C_3N_4/CoS which exhibited a specific capacitance value of 668 Fg^{-1} at a current density of 2 Ag^{-1} which is

higher than the individual components in a three electrode cell assembly.[22] $Ni(OH)_2$ nano flowers were grown on a sandwiched layers of g-C_3N_4 and reduced graphene oxide by Li *et al*.[23] and this hybrid sample has shown an excellent specific capacitance of 1785 Fg^{-1}. In a recent report by Ansari *et al*.[24] commercially purchased MoS_2 and g-C_3N_4 was used for the preparation of MoS_2/g-C_3N_4 heterostructure and was used as a supercapacitor electrode in a three electrode cell. The hybrid sample delivered a high specific capacitance of 240 Fg^{-1} than the bare MoS_2 (48.77 Fg^{-1}) with good cyclic stability. Zhao *et al*.[25] reported a g-C_3N_4 hybridised TiO_2 nanoparticle assembly by hydrothermal method which exhibited a high specific capacitance of 125.1 Fg^{-1} at 1 Ag^{-1} which can be attributed to the enhanced charge transport properties provided by g-C_3N_4 sheets. The results show that the electrochemical performance of g-C_3N_4 can be tailored by fabricating heterojunction materials with transition metal oxides and sulphides. Moreover, the recent studies shows that the technocrats are searching for low cost and environmental friendly transition metal oxide hybrid materials as an alternative for RuO_2 based supercapacitors owing to its exorbitant rate and toxicity.[26] Guan *et al*. studied the effect of morphology on the supercapacitance of nanostructured $NiCo_2O_4$/graphitic carbon nitride nanocomposite in three electrode configuration.[27] Among the low cost and green electrodes MnO_2 and SnO_2 based hybrid materials occupy special attention due to its excellent electrochemical performance.[19]

In all these reports, the electrochemical performance of the samples was measured in ***three electrode*** configuration which is far different

from the performance of the electrodes in actual device conditions. Compared to three electrode configuration, measurements in ***two electrode configuration*** is more suitable for evaluating the performance of supercapacitor test cells as it mimics the physical configuration and charge transfer that occur in real supercapacitor application and thus provides the best indication of an electrode material's performance.

In the present work MnO_2 and SnO_2 were chemically grown directly over a 2D support of g-C_3N_4 to develop g-C_3N_4/MnO_2 and g-C_3N_4/SnO_2 nanohybrid materials. Symmetrical supercapacitors were fabricated using the synthesized composites and their electrochemical performance was compared with that of bare g-C_3N_4 in a two electrode cell assembly and the results are discussed.

4. 2. Results and discussion

A schematic representation of the overall synthesis of g-C_3N_4/MnO_2 *via* oxidation/reduction mechanism and g-C_3N_4/SnO_2 through air oxidation process at a calcinations temperature of 350 ^oC/2 hrs can be represented by the following **equations 4. 1 and 4. 2.** Schematic representation of the formation of nano hybrid materials is shown in **Scheme 4. 1 and 4. 2**.

$$3MnSO_4+2KMnO_4+2H_2O \rightarrow 5MnO_2+K_2SO_4+2H_2SO_4 \quad (4.\ 1)$$

$$SnCl_2+O_2 \rightarrow SnO_2+Cl_2 \quad (4.\ 2)$$

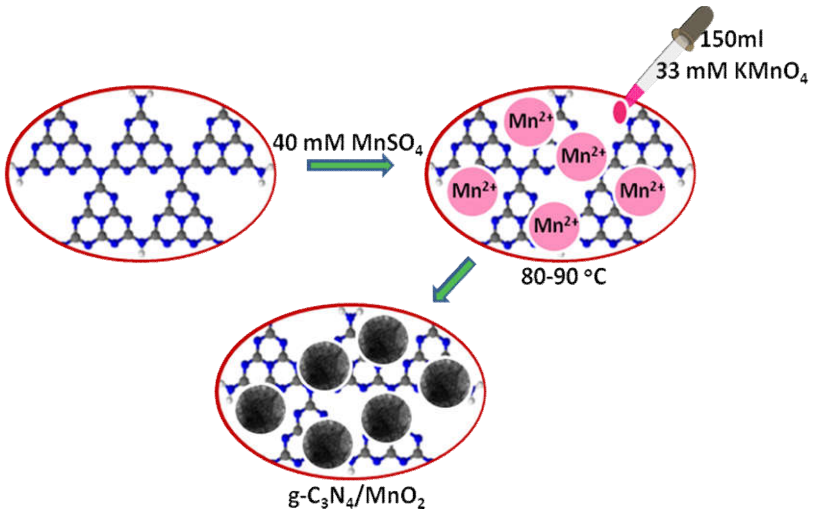

Scheme 4. 1. The growth mechanism of needle like MnO_2 structures on g-C_3N_4.

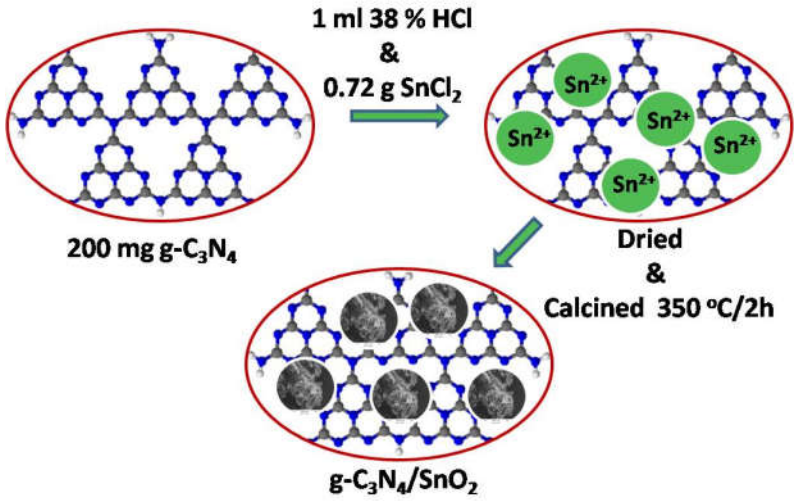

Scheme 4. 2. The growth mechanism of SnO_2 nano structures on g-C_3N_4.

4. 2. 1. XRD analysis

X-ray diffraction pattern was used to confirm the crystalline phase analysis of the synthesized electrode materials. As observed in **Figure 4. 1(a)**, sharp peak at 27.1^{o} with an interplanar distance of 0.326 nm (002) is originated from the layer stacking arrangement of conjugated aromatic systems in g-C_3N_4 and the peak at 13.1^{o} is from the (100) plane formed in the crystal due to the presence of in-planar tri-s-triazine units.[20] The crystalline phase of SnO_2 in composite sample g-C_3N_4/SnO_2 was confirmed by the presence of peaks at 2θ values at 26.8, 33.6, 38.1, 51.6, 53.4 and 63.6 which correspond to the reflection from (110), (101), (200), (211), (220), (310) and (212) planes of tetragonal SnO_2 (JCPDS card no. 41-1445). The XRD peaks of the g-C_3N_4/MnO_2 show four characteristics peaks situated at 2θ values which corresponds to the lattice reflection from (110), (220), (400) and (002) planes of α-MnO_2 having tetragonal symmetry (JCPDS card no. 44-0141). Compared to the g-C_3N_4/SnO_2 hybrid material, g-C_3N_4/MnO_2 has shown a partially crystalline nature as evidenced from the XRD spectrum. The amorphous nature of the material is considered to be more beneficial for supercapacitor electrode application since it facilitates the wettability at the electrode-electrolyte interface and thereby increases the charge transport properties. Confirmation of g-C_3N_4 phase in the composite samples is marked as (c) in the XRD spectrum.

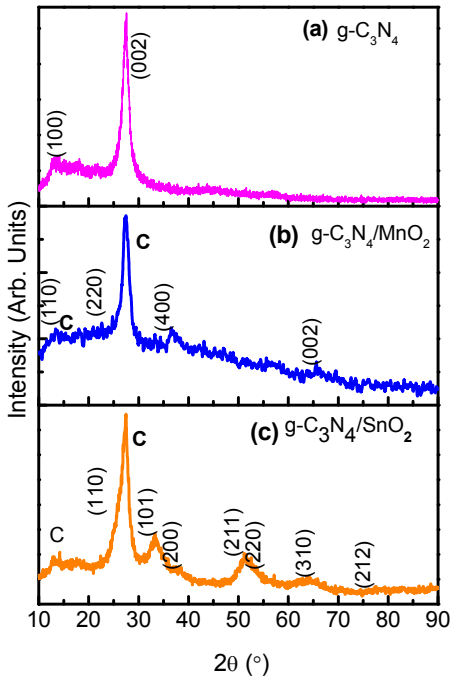

Figure 4. 1. XRD patterns of (a) g-C_3N_4 (b) g-C_3N_4/MnO_2 (c) g-C_3N_4/ SnO_2.

4. 2. 2. FTIR Spectral analysis

FTIR spectra of bare g-C_3N_4 and g-C_3N_4/MnO_2, g-C_3N_4/SnO_2 composite samples were depicted in the **Figure 4. 2**. g-C_3N_4 **(Figure. 4. 2a)** exhibits several peaks in 1200-1600 cm^{-1} region which represents the C-N stretching vibrations of the heterocyclic ring. The peak at 810 cm^{-1} originates from the characteristic in-plane breathing vibrational mode of s-triazine units.[30] The peak at 500-700 cm^{-1} in the **Figure 4. 2(b)** was derived from the stretching vibrational modes of Mn-O and Mn-O-Mn bonds of the MnO_2 present in the composite sample. The peaks at 1100-1040 cm^{-1} in the **Figure 4. 2(b)** was originated from the bending vibrational modes of –OH groups attached to the surface of MnO_2 molecules which indicates that the MnO_2 in

composite sample g-C_3N_4/MnO_2 was highly hydroxylated compared to other samples.[31] The –OH bending vibrational modes at 1631 and 1392 cm^{-1} in the IR spectra are intermixed with the peaks of g-C_3N_4. The FTIR spectra of g-C_3N_4/SnO_2 composite **(Figure 4. 2c)** samples also show a distinct nanohybrid structure formed between the constituent phases. In addition to g-C_3N_4 peaks, the peaks at 450 to 650 cm^{-1} indicates the characteristic vibrational modes of Sn-O bonds in SnO_2.[32] The broad peaks in all the samples at around 3200-3600 cm^{-1} can be attributed to the symmetric stretching vibrations of surface adsorbed H_2O molecules.

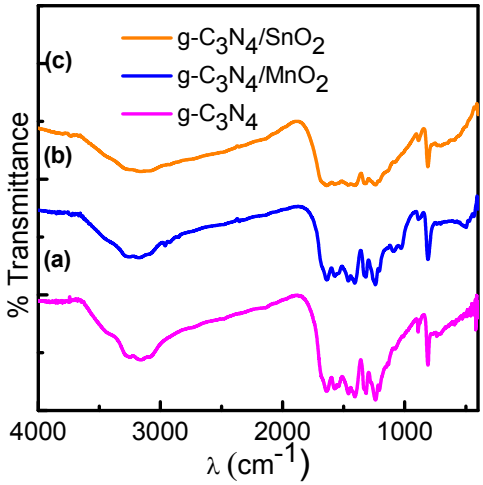

Figure 4. 2. FTIR spectra of (a) g-C_3N_4 (b) g-C_3N_4/MnO_2 (c) g-C_3N_4/ SnO_2.

4. 2. 3. Morphology Analysis

The morphology and the microstructure of the composite samples were analyzed using transmission electron microscopy (TEM) and field emission scanning electron microscopy (FESEM). It is clear from **Figure 4. 3(a)** that MnO_2 phases with flower type morphologies were uniformly distributed in the g-C_3N_4 phase. While growing MnO_2 phase

on the g-C_3N_4 sheets MnO_2 crystallize in nanoflakes morphology. These nanoflakes with high surface energy undergo molecular self-assembly to form more stable MnO_2 nanoflowers on the surface the g-C_3N_4 sheets. The SAED pattern with concentric rings indicates that the MnO_2 phases were not formed in the perfect crystalline state however they are in a partially crystalline state as observed from the XRD patterns **(Figure 4. 1b)**. The SnO_2 phases were formed over the g-C_3N_4 phase in spherical morphology and by comparing to MnO_2 phase they are more crystalline as observable from the SAED pattern in the **Figure 4. 3(b) & (d)**. The surface morphology and the interaction between the constituent phases in the composite samples, g-C_3N_4/MnO_2 and g-C_3N_4/SnO_2 were further confirmed from the FESEM images represented in **Figure 4. 3(e) & (f)** respectively. The SEM images indicate the proper mixing of metal oxide nanostructures on g-C_3N_4 phase.

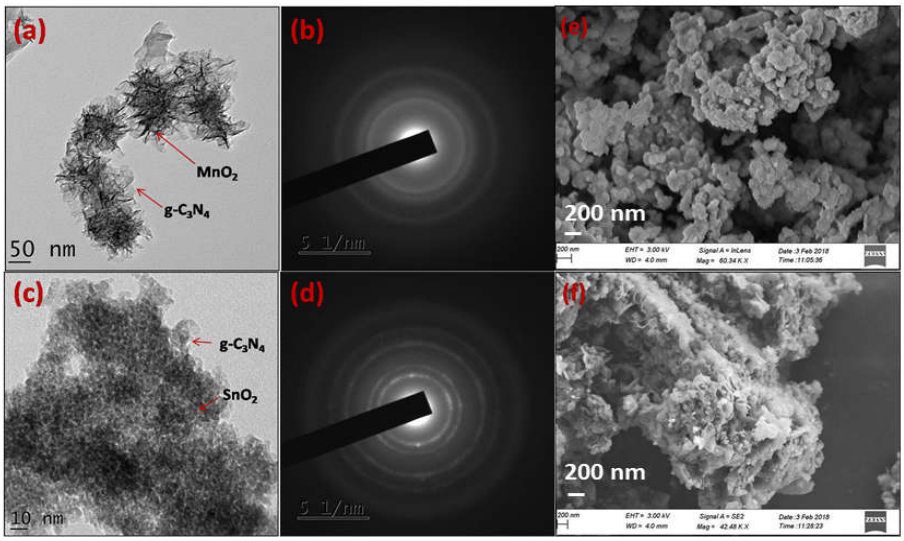

Figure 4. 3. TEM images of (a) g-C_3N_4/MnO_2 (c) g-C_3N_4/SnO_2 (b) & (d) corresponding SAED patterns (e) & (f) FESEM images of the composites g-C_3N_4/MnO_2 and g-C_3N_4/SnO_2.

4. 2. 4. BET-Surface area analysis

Nitrogen adsorption-desorption isotherms of various electrode samples were given in **Figure 4. 4**. All the samples exhibited a distinct type IV physisorption curve with H3 hysteresis loop which are in accordance with the IUPAC characteristics for mesoporous materials with pore size between 2-50 nm. The calculated surface area values from the isotherms were found to be 32. 8, 38. 2 and 70. 2 m^2g^{-1} for g-C_3N_4, g-C_3N_4/SnO_2 and g-C_3N_4/MnO_2 samples respectively. The high BET surface area possessed by g-C_3N_4/MnO_2 can be attributed to the effective spacer effect of MnO_2 in between the 2D layers of g-C_3N_4. Moreover, the flower type morphology of MnO_2 enhances the accessible surface area of g-C_3N_4/MnO_2 electrodes for the electrochemical process. The average BJH adsorption pore volume and the BJH desorption pore size values are given in **Table 4. 1**. The average pore size value of g-C_3N_4 gets reduced while adding metal oxide. This can be attributed to the incorporation of metal oxide particles in between the pores or the layers of lamellar g-C_3N_4. The average pore volume of MnO_2 loaded samples increased effectively due to the porous nature of MnO_2 nanostructure as evidenced from the TEM images. The high surface area and pore volume possessed by g-C_3N_4/MnO_2 enable them to effectively interact with large number of electrolyte ions for getting better electrochemical performance than g-C_3N_4/SnO_2 samples.

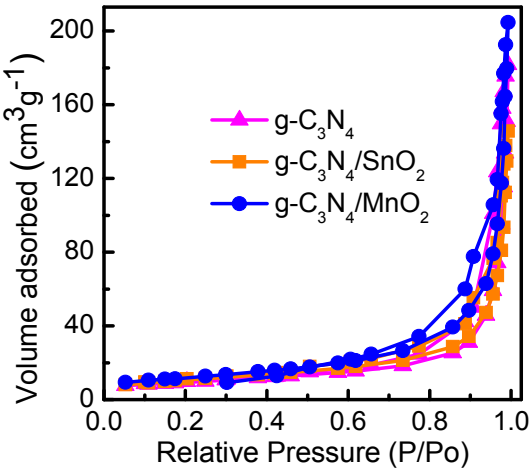

Figure 4. 4. BET N_2 adsorption isotherms of various electrodes

Table 4. 1. BET surface area and pore size measurements.

Sample	BET surface area/$m^2 g^{-1}$	Pore volume/ $cm^3 g^{-1}$	BJH desorption pore size/nm
g-C_3N_4	32	0.29	25.9
g-C_3N_4/SnO_2	38	0.23	20.7
g-C_3N_4/MnO_2	70	0.34	19.6

4. 2. 5. Cyclic Voltammogram (CV)

The electrochemical performance of the prepared electrode materials was measured in symmetric two electrode configuration within the potential range from 0 to 1 V. The cyclic voltammograms of the symmetric supercapacitors based on g-C_3N_4, g-C_3N_4/SnO_2 and g-C_3N_4/MnO_2 electrodes at 5, 10, 20, 50, 100 and 200 mVs^{-1} are given in the **Figure 4. 5**. All the three devices exhibited nearly rectangular type CV curves. The enhanced current value in the CV loops of g-C_3N_4/MnO_2 electrodes as compared to the other two devices indicates

higher level of charge storage. Two types of mechanism can be proposed for the pseudocapacitive charge storage in MnO_2 system. First one is by the intercalation and extraction of proton or metal cation into the oxide layers. Second is by the surface adsorption and desorption of the electrolyte cation or proton. The chemical **equation** can be represented as **4. 1** and **4. 2**[33]

$$MnO_2 + M^+ + e^- \rightarrow MnOOM \quad (4.\ 1)$$

$$MnO_{2\ (surf)} + M^+ + e^- \rightarrow MnOOM_{\ (surf)} \text{ where } (M^+ = K^+, H_3O^+) \quad (4.\ 2)$$

The superior performance of the supercapacitor based on g-C_3N_4/MnO_2 electrodes may be attributed to the improved surface area of the composite upon MnO_2 loading (as confirmed from the BET results) and the pseudocapacitive contribution from MnO_2 nanoflakes.

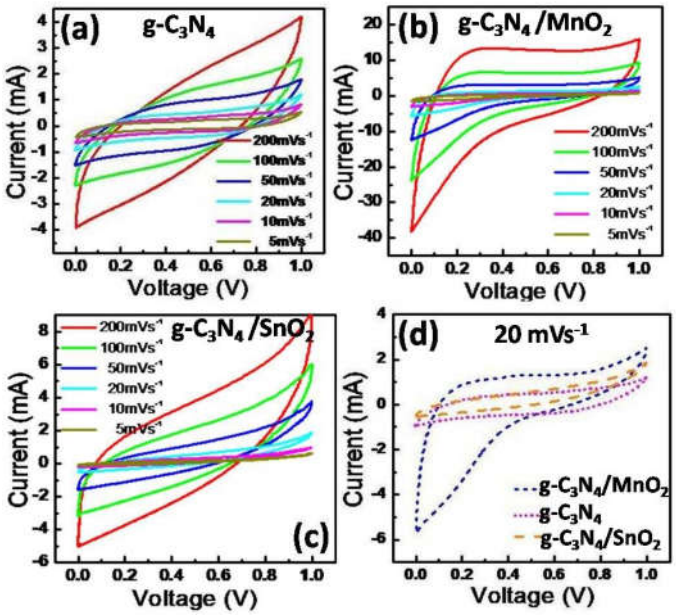

Figure 4. 5. Cyclic voltammograms of (a) g-C_3N_4 (b) g-C_3N_4/SnO_2 (c) g-C_3N_4/MnO_2 at different scan rates (d) Comparison of the CV loops of the various supaercapacitors at a scan rate of 20 mVs^{-1}.

A comparison of the CV loops of different supercapacitors fabricated from various electrode materials at a scan rate of 20 mVs^{-1} was shown in the **Figure 4. 5(d)**. For the same mass loading, the supercapacitor based on g-C_3N_4/MnO_2 electrode exhibited superior charge storage performance with negligible contact resistance.[34] **Figure 4. 6** show a general characteristic of the variation of specific capacitance with scan rates from 5 mVs^{-1} to 200 mVs^{-1}. At a scan rate of 5 mVs^{-1}, the specific capacitance value calculated from the CV loops of symmetric supercapacitors based on g-C_3N_4/MnO_2, g-C_3N_4/SnO_2 and bare g-C_3N_4 electrodes are 192 Fg^{-1}, 93 Fg^{-1} and 72 Fg^{-1} respectively.

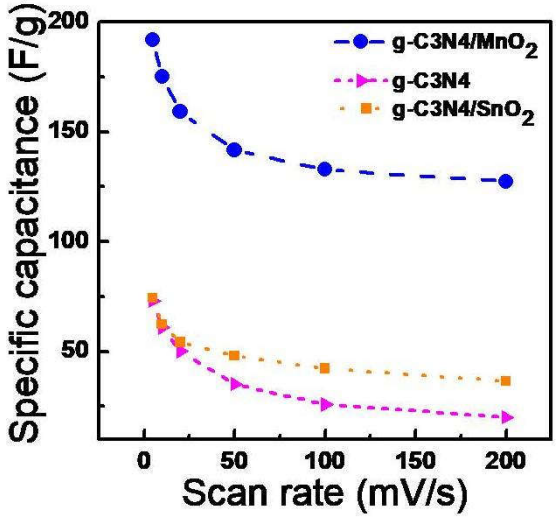

Figure 4. 6. Variation of specific capacitance of g-C_3N_4, g-C_3N_4/MnO_2 and g-C_3N_4/SnO_2 as a function of scan rate.

4. 2. 6. Galvanostatic Charge-Discharge Curves (GCD)

The galvanostatic charge-discharge (GCD) curves of symmetric supercapacitors in two electrode configuration at a constant current density of 1 Ag^{-1} in the potential range of 0 to 1 V are shown in **Figure 4. 7**. The GCD measurements are standard tests used to analyze the

performance of the electrode material in practical operational conditions. The specific capacitance of the supercapacitor device for various electrode materials calculated from GCD was found to be 174 Fg^{-1}, 64 Fg^{-1} and 50.22 Fg^{-1} for g-C_3N_4/MnO_2, g-C_3N_4/SnO_2 and g-C_3N_4 respectively. The specific capacitance values obtained in the present study are lower than the values reported for MnO_2 modified g-C_3N_4 composites in 3-electrode configuration (211 Fg^{-1})[21]. But it is well-known that a three electrode measurement configuration always gives higher specific capacitance values than a two electrode configuration. The two electrode configuration is best suited to evaluate the performance in a real device.

The duration of the charge-discharge cycle for MnO_2 modified g-C_3N_4 is extremely higher when compared to other supercapacitor devices with very small IR drop value characteristics of electrodes with very small internal resistance.[19] At a constant power density of 1 $kWkg^{-1}$ the symmetric supercapacitors based on g-C_3N_4 and g-C_3N_4/SnO_2 as electrodes exhibited an energy densities of 6.9 and 8.8 $Whkg^{-1}$ respectively however the energy density of g-C_3N_4/MnO_2 has given a three times higher value (24.1 $Whkg^{-1}$) than the energy densities possessed by other electrodes.

The enhancement in the electrochemical performance of g-C_3N_4/MnO_2 based supercapacitor can be attributed to the pseudo capacitive contribution from the high surface area MnO_2 loaded electrode. However, the pseudocapacitive contribution from SnO_2 in g-C_3N_4/SnO_2 electrode was found to be very small owing to the small BET surface area value possessed by this electrode sample.

4. 2. 7. Cyclic Stability

The stability performance of the supercapacitor devices is evaluated by conducting galvanostatic charge- discharge measurements for 6000 cycles at a constant current density of 5 Ag^{-1} in the potential range between 0 and + 1 V. The stability curves are shown **Figure 4. 7(b)**. After 6000 charge-discharge cycles, symmetric supercapacitors based on g-C_3N_4, g-C_3N_4/MnO_2 and g-C_3N_4/SnO_2 electrodes exhibited a cycling stability of 94%, 85% and 87% respectively.

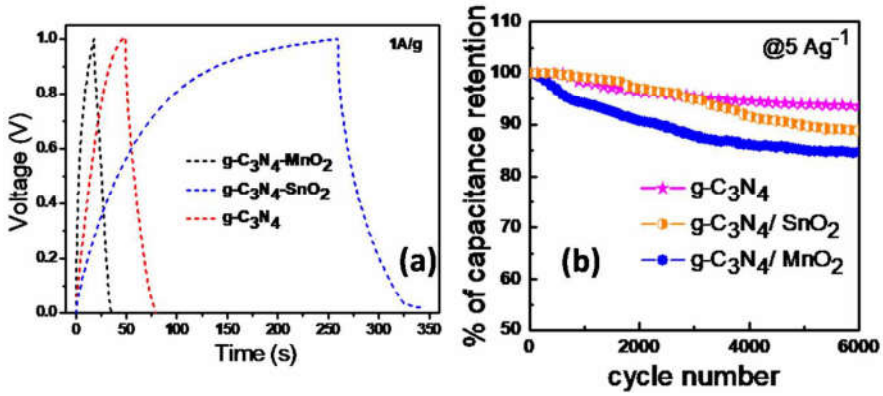

Figure 4. 7. (a) Galvanostatic charge–discharge curves of g-C_3N_4, g-C_3N_4/MnO_2 and g-C_3N_4/SnO_2 based supercapacitor devices at a constant current density of 1 Ag^{-1} in 2 M KOH electrolyte and (b) cycling performance of the symmetric supercapacitors at a constant current current density of 5 Ag^{-1}.

4. 2. 8. Electrochemical Impedance Spectra (EIS)

Electrochemical impedance spectroscopy (EIS) was used to further analyze the performance of the supercapacitor electrode materials. The electrochemical impedance spectra (Nyquist plots) of g-C_3N_4, g-C_3N_4/MnO_2 and g-C_3N_4/SnO_2 based supercapacitor devices are shown in **Figure 4. 8**. The Nyquist plot consists of a semicircle at high-frequency region and a straight line at the low-frequency region.[1,2] The

high-frequency region determines the charge transport properties at electrode-electrolyte interface. The diameter of the semicircle gives the value of charge-transfer resistance (R_{ct}). The high-frequency region of the impedance spectra is given as inset of **Figure 4. 8**. A vertical line in the low-frequency region suggests an ideal capacitive behavior. However, if the line makes an angle 45° with the real axis, it is called the Warburg line which results from the frequency dependence of ion diffusion in the electrolyte to the electrode interface. Length of the straight line at a low frequency range is associated with the ion diffusion resistance of the electrolyte ions into the bulk electrode. Shorter length of the Warburg line indicates that the electrode offers lower impedance to the diffusion of electrolyte ions, there by offering improved charge storage performance. The length of the straight line in the low-frequency region is the shortest for MnO_2 loaded g-C_3N_4 electrode and it also shows a very small R_{ct} value, indicating the superior capacitive performance as compared to bare g-C_3N_4 and g-C_3N_4/SnO_2.

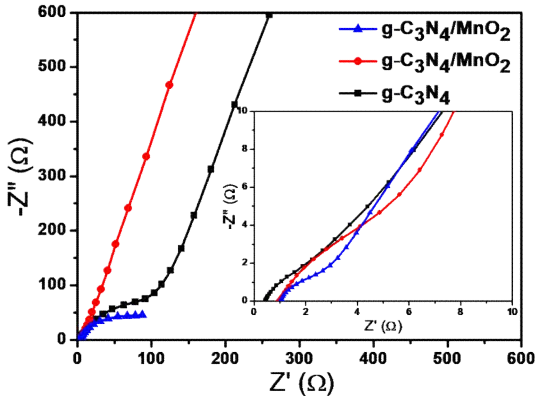

Figure 4. 8. Nyquist plots for g-C_3N_4, g-C_3N_4/MnO_2 and g-C_3N_4/SnO_2 based supercapacitor devices at dc bias of 0 V with sinusoidal signal of 5 mV over the frequency range from 100 kHz and 1 MHz. *Z*': real impedance. *Z*": imaginary impedance.

4. 3. Conclusions

Pseudocapacitive MnO_2 and SnO_2 anchored g-C_3N_4 nanosheets g-C_3N_4/MnO_2, g-C_3N_4/SnO_2 were synthesized *via* one-pot chemical reduction technique. The material characterization using XRD, FTIR and TEM studies demonstrated a good homogeneity between the constituent phases for hybrid materials. The electrochemical performance of the bare g-C_3N_4 was found to be enhanced remarkably by MnO_2 incorporation. The specific capacitance values of g-C_3N_4, g-C_3N_4/SnO_2 and g-C_3N_4/MnO_2 calculated from charge- discharge curve was found to be 50.22 Fg^{-1}, 64 Fg^{-1}, 174 Fg^{-1} respectively and the corresponding energy density values at a constant power density of 1 $kWkg^{-1}$ are 6.9, 8.8 and 24.1 $Whkg^{-1}$. The performance increase in g-C_3N_4/MnO_2 hybrid electrode material was attributed to the spacer effect of MnO_2 nanoflowers in between the g-C_3N_4 layers which enhance the BET surface area and thereby facilitating excellent charge transport at the electrode-electrolyte interfaces. The present work can be used as a platform for the development of modified carbon-based electrode materials for electrochemical storage device applications.

References

1. W. J. Gan, L. Hongzhen, Z. Xingyuan, L. Xu, L. Xingrui, K. Feiyu, *Small*, 2018, 14, 1703950.
2. J. G. Wang, H. Liu, H. Sun, W. Hua, H. Wang, X. Liu, B. Wei, *Carbon*, 2018, 127, 85.
3. M. Armand, J. M. Tarascon, *Nature*, 2008, 451, 652.
4. D. Damien, G. S. Anjusree, A. S. Nair, M. M. Shaijumon, *RSC Adv*., 2016, 6, 45802.
5. M. D. Stoller, R. S. Ruoff, *Energy Environ. Sci*., 2010, 3, 1294.
6. R. B. Rakhi, D. Cha, W. Chen, H. N. Alshareef, *J. Phys. Chem. C*, 2011, 115, 14392.
7. P. Simon, Y. Gogotsi, *Nat. Mater.,* 2008, 7, 845.
8. R. Kötz, M. Carlen, *Electrochim. Acta*, 2000, 45, 2483.
9. M. S. Halper, J. C. Ellenbogen, The MITRE Corporation, McLean, Virginia, USA. 2006.
10. M. Inagaki, H. Konno, O. Tanaike, *J. Power Sources*, 2010, 195, 7880.
11. J. Zhang, X. Zhang, Y. Zhou, S. Guo, K. Wang, Z. Liang, Q. Xu, *ACS Sus. Chem. Eng*., 2014, 2, 1525.
12. L. F. Chen, X. D. Zhang, H. W. Liang, M. Kong, Q. F. Guan, P. Chen, Z. Y. Wu, S. H. Yu, *ACS Nano*, 2012, 6, 7092.
13. C. Lu, D. Wang, J. Zhao, S. Han, W. Chen, *Adv. Fun. Mater*., 2017, 27, 1606219.
14. Y. Gong, M. Li, Y. Wang, *Chem. Sus. Chem*., 2015, 8, 931.
15. M. Tahir, C. Cao, N. Mahmood, F. K. Butt, A. Mahmood, F. Idrees, S. Hussain, M. Tanveer, Z. Ali, I. Aslam, *ACS Appl. Mater. Interfaces*, 2013, 6, 1258.
16. J. G. Wang, H. Liu, H. Liu, W. Hua, M. Shao, *ACS Appl. Mater. Interfaces*, 2018, 10, 18816.
17. J. G. Wang, Z. Zhang, X. Zhang, X. Yin, X. Li, X. Liu, F. Kang, B. Wei, *Nano Energy*, 2017, 39, 647.

18. J. G. Wang, F. Kang, B. Wei, *Prog. Mater. Sci*., 2015, 74, 51.

19. Q. Y. Shan, X. L. Guo, F. Dong, Y. X, Zhang, *Mater. Lett*., 2017, 202, 103.

20. X. Chang, X. Zhai, S. Sun, D. Gu, L. Dong, Y. Yin, Y. Zhu, *Nanotechnology*, 2017, 28, 135705.

21. D. Jiang, Q. Xu, S. Meng, C. Xia, M. Chen, *J. Alloys Compd.*, 2017, 706, 41.

22. L. Li, J. Qin, H. Bi, S. Gai, F. He, P. Gao, Y. Dai, X. Zhang, D. Yang, P. Yang, *Sci. Rep*., 2017, 7, 43413.

23. S. A. Ansari, M. H. Cho, *Sci. Rep*., 2017, 7, 43055.

24. Y. Zhao, L. Xu, S. Huang, J. Bao, J. Qiu, J. Lian, L. Xu, Y. Huang, Y. Xu, H. Li, *J. Alloys Compd*., 2017, 702, 178.

25. R. B. Rakhi, W. Chen, D. Cha, H. N. Alshareef, *J. Mater. Chem*., 2011, 21, 16197.

26. B. Guan, Q. Y. Shan, H. Chen, D. Xue, K. Chen, Y. X. Zhang, *Electrochim. Acta*, 2016, 200, 239.

27. S. Panneri, P. Ganguly, B. N. Nair, A. A. Mohamed, K. G. Warrier, U. N. Hareesh, *Environ. Sci. Pollut. R*., 2017, 24, 8609.

28. V. Khomenko, E. Frackowiak, F. Beguin, *Electrochim. Acta*, 2005, 50, 2499.

29. Chen H, Wang Y, Lv YK. Catalytic oxidation of NO over MnO_2 with different crystal structures. *RSC Adv*., 2016, 6, 54032.

30. Z. A. Hu, Y. L. Xie, Y. X. Wang, L. P. Mo, Y. Y. Yang, Z. Y. Zhang. *Mater. Chem. Phys*., 2009, 114, 990.

31. W. Xiao, H. Xia, J. Y. Fuh, L. Lu, *J. Power Sources*, 2009, 193, 935.

32. B. Babu, S. G. Ullattil, R. Prasannachandran, J. Kavil, P. Periyat, M. M. Shaijumon, *ACS Sustain. Chem. Eng*., 2018, 6, 5401.

Chapter Five

g-C_3N_4/CuO and g-C_3N_4/Co_3O_4 Nanohybrid Structures as Low cost Electrode Material in Symmetric Supercapacitor Device.

Contents

5. 1. Introduction

The renewable energy storage and its supply upon demand has been a serious challenge among researchers owing to the short life span and poor power delivery of conventionally used lithium ion batteries.[1] Supercapacitor has recognized as a suitable storage device that can be used in combination with batteries to mitigate the power delivery problems associated with batteries.[2] Supercapacitors possess excellent performance recyclability due to the absence of any type mass transfer between the electrodes.[3] Carbon based electrode materials have been used conventionally in supercapacitor devices due to its high surface area and storage capacity.[4] Nitrogen doped carbon allotropes were emerged recently as supercapacitor electrodes, which shows excellent electrode-electrolyte interaction due to the presence of lone pair of electrons on nitrogen atom.[5] Graphitic carbon nitride (g-C_3N_4) is considered as an intrinsically nitrogen rich system with lamellar structure and it could offer more number of binding sites for the electrolyte molecules to interact with the electrode surface.[6] However, the low surface area and the agglomerated layer structure limit its

application as a supercapacitor device electrode.[7] Transition metal oxides with pseudocapacitive nature can be suitably coupled with g-C_3N_4 layer structure in order to mitigate the limitations of bare g-C_3N_4 electrodes.[8]

Among the transition metal oxides Co_3O_4 and CuO have received great deal of attention due to their economically viable and environmental friendly nature.[9,10] Only a very few reports are available in the literature based on the electrochemical properties of g-C_3N_4 and Co_3O_4, CuO nanohybrid systems. In a recent research by Zheng *et al.* mesoporous Co_3O_4 was anchored on g-C_3N_4 surface and the composite material possesses a specific capacitance value of 780 Fg^{-1} at a current density of 1.25 Ag^{-1}.[11] In another attempt Shim *et al.* fabricated a supercapcitor device from carbon and CuO anchored g-C_3N_4, which has given a specific capacitance value of 247.2 Fg^{-1} at a current density of 1 Ag^{-1}.[12] In the available reports the electrochemical performance of the material were characterized in three electrode configuration only, however the actual performance of the device should be analyzed in two electrode configuration for practical applications.

In the present work pseudocapacitive Co_3O_4 and CuO metal oxides were grown on the surface of a 2D g-C_3N_4 phase. The hybrid materials were employed as electrode material in symmetric supercapacitors. The highlight of the present research is that the electrochemical properties of Co_3O_4 and CuO modified g-C_3N_4 were analyzed for the first time in symmetric two electrode configuration. The present research will be an excellent reference for the researchers working in the area of developing high energy density electrode materials with environmentally and economically benign nature.

5. 2. Results and Discussion

5. 2. 1. X-ray Diffraction

The X-ray diffraction studies of the composite samples were carried out to analyze the phase formation of the component phases and were given as **Figure 5. 1**. In the XRD spectrum of g-C_3N_4/Co_3O_4 (**Figure 5. 1a**), the peaks at 2θ values 18.9, 31.2, 36.9, 38.2, 44.7, 54.8, 59.4 and 65.3 corresponds to the diffraction from (111), (220), (311), (222), (400), (422), (511) and (440) planes of cubic phase of Co_3O_4 (JCPDS No: 43-1003).[13] The XRD spectrum of g-C_3N_4/CuO shows reflections at 2θ values 35.6, 38.5,49.2, 66.6 and 68.2 corresponds to (-111), (111), (-202), (022) and (220) planes of monoclinic phase of CuO (JCPDS No: 48-1548). The crystallite size of the particles calculated from Debye-Scherrer formula was found to be 8-10 nm and 10-15 nm for g-C_3N_4/CuO and g-C_3N_4/Co_3O_4 respectively. The diffraction peaks marked as (C*) is the characteristic peak of g-C_3N_4 originated from the layer stacking arrangements in two dimensional g-C_3N_4 networks.

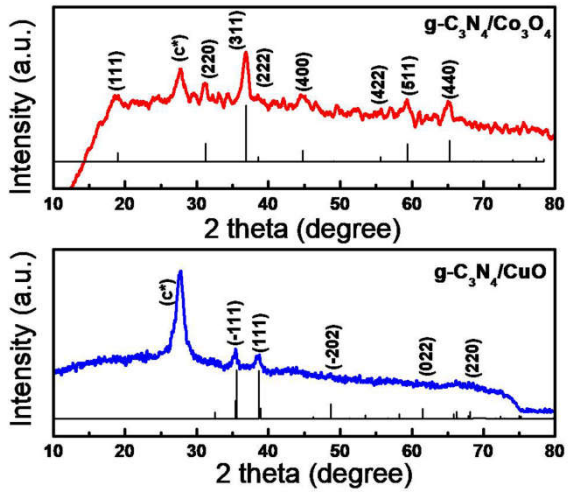

Figure 5. 1. XRD spectra of (a) g-C_3N_4/Co_3O_4 and (b) g-C_3N_4/CuO.

5. 2. 2. FTIR Spectra

The FTIR analysis (**Figure 5. 2**) of the composite sample was done to further analyze the phase formation of the constituent phases and to determine the presence of functional group on the surface of the electrode material. The common peaks in both the spectra of g-C_3N_4/Co_3O_4 and g-C_3N_4/CuO are due to the contribution from g-C_3N_4 phase. The peaks at the region of 1200-1600 cm^{-1} arises from the –CN stretching vibrations of the heterocyclic rings of s-triazine units. The sharp at 810 cm^{-1} is the characteristic peak arises from the breathing mode vibrations of triazine ring.[14] The peaks around 1000-1100 cm^{-1} arises from the bending vibrations of –OH functional groups and the broad peaks around 3200-3600 cm^{-1} originates from the stretching vibrations of H_2O molecules adsorbed on the surface of the electrode material. The existence of spinel Co_3O_4 nanoparticles on the electrode sample can be confirmed from the presence of sharp characteristic peaks in **Figure 5. 2(a)** at 575 cm^{-1} and 665 cm^{-1} respectively.[11] The peak at 537 cm^{-1} in **Figure 5. 2(b)** is the stretching vibrational band of Cu-O bond in monoclinic CuO crystal.[15]

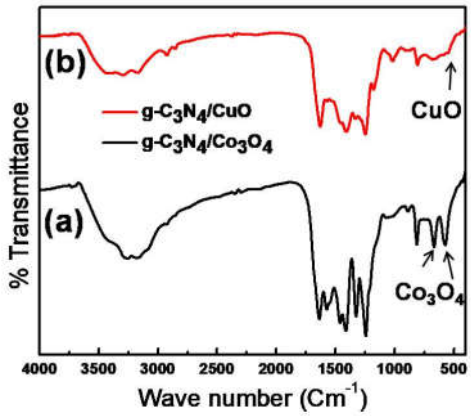

Figure 5. 2. FTIR spectra of (a) g-C_3N_4/Co_3O_4 and (b) g-C_3N_4/CuO.

5. 2. 3. X-ray Photoelectron Spectroscopy (XPS)

XPS spectra of the hybrid nanostructures g-C_3N_4/Co_3O_4 and g-C_3N_4/CuO were recorded inorder to analyze the chemical composition and the electronic environment of the electrode materials. The survey XPS spectra of the samples were given as **Figure 5. 3(a) & (b)**. The survey spectrum confirms the presence of constituent phases in the composite sample. Binding energy values in all the spectra were carbon corrected by comparing with C1s value of 284. 8 eV. The high resolution XPS spectra of Co in **Figure 5. 3(c)** exhibits well defined peaks at 780 and 796 eV corresponding to the $Co2p_{3/2}$ and $Co2p_{1/2}$ spin states with a spin separation of 16 eV, which are the characteristics of Co_3O_4 phase. Two weak satellite peaks at 788 and 804 eV are the features of spinel structure in which +3 ion occupy octahedral site and +2 ion at the tetrahedral sites.[16] The O1s peak at 531.2 eV in **Figure 5. 3(d)** is the characteristic peak of spinel Co_3O_4 structure which arises due to the presence of lattice oxygen. Second O1s peak at 535.9 eV is due to the presence of defective oxygen on the surface of the Co_3O_4 phase. The two major peaks of C1s in **Figure 5. 3(e)** at 284. 8 and 288.6 eV are originated from the sp^2 hybridised N-C=N structure of g-C_3N_4 network. The N1s peaks in **Figure 5. 3(f)** at 398.4 and 400.5 eV are attributed to the N atom from N-C=N and N-$(C)_3$ structural units of g-C_3N_4.[7]

The high resolution XPS spectra of Cu in g-C_3N_4/CuO is depicted in **Figure 5. 3(g)**. The peaks at 933.2 and 953.3 eV are the characteristic signal of $Cu2p_{3/2}$ and $Cu2p_{1/2}$ respectively and the satellite peaks of Cu^{2+} at higher binding energy region are also visible.[17] The O1s give

spectra at 531. 4 and 536. 1 eV which are the characteristics of lattice and defective oxygen respectively **(Figure 5. 3h)**. C1s peaks at **(Figure 5. 3i)** 284.7 eV, 288.8 eV and the N1s peaks **(Figure 5. 3j)** 398.9 eV and 400.9 eV are the characteristic peaks of g-C_3N_4 as discussed in the case of g-C_3N_4/Co_3O_4.[7]

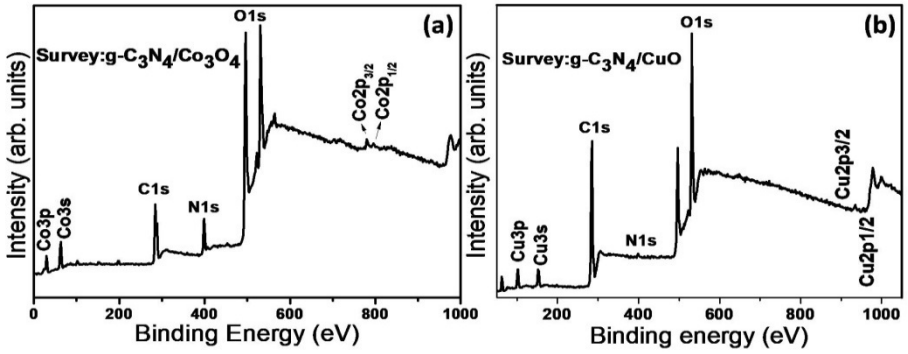

Figure 5. 3. Survey XPS spectrum of (a) g-C_3N_4/Co_3O_4 and (b) g-C_3N_4/CuO.

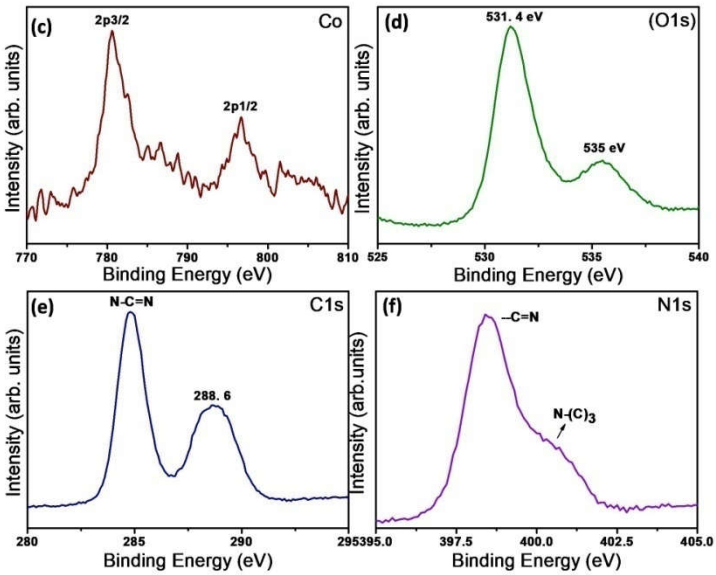

Figure 5. 3. High resolution spectra of (c) Co2p, (d) O1s, (e) C1s and (f) N1s in g-C_3N_4/Co_3O_4.

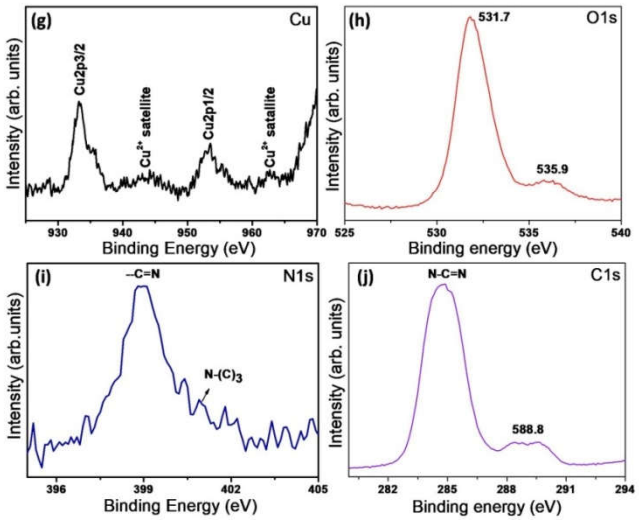

Figure 5. 3. High resolution spectra of (g) Cu2p (h) O1s (i) N1s and (j) C1s.

5. 2. 4. Morphology Analysis

The surface morphology of the composite electrodes g-C_3N_4/Co_3O_4 and g-C_3N_4/CuO were depicted as **Figure 5. 4(a)** and 5. **4(b).** g-C_3N_4/Co_3O_4 sample exhibited a spherical morphology with porous nature, however in g-C_3N_4/CuO the particles aggregated together to form large grains which is unfavorable for the penetration of electrolyte molecules during electrochemical process.

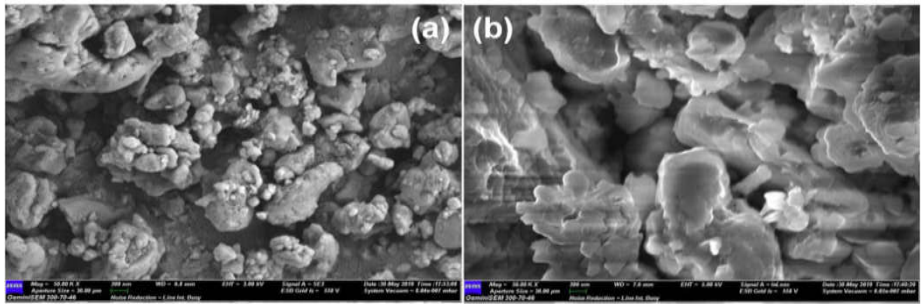

Figure 5. 4. FESEM images of (a) g-C_3N_4/Co_3O_4 and (b) g-C_3N_4/CuO electrodes.

Morphology and further analysis of the crystalline nature of the materials were carried out using TEM. It can be seen from the **Figure 5. 5(a)** that the Co_3O_4 particles were uniformly distributed in the network of g-C_3N_4 with clear boundary between the constituent phases; however in g-C_3N_4/CuO **(Figure 5. 5c)** the distribution of CuO in g-C_3N_4 matrix is non-homogeneous with a small aggregation of metal oxide phases in the matrix. The SAED patters of the composite sample indicated that in g-C_3N_4/CuO **(Figure 5. 5d)**, the metal oxide phases are more crystalline with bright spots than in g-C_3N_4/Co_3O_4 **(Figure 5. 3e)** (The results are matching with the XRD results). The crystalline phases usually reduce the performance of an electrochemical device by decreasing the accessible surfaces for the electrolyte molecule to interact with electrode surface. It is also seen from SAED pattern that the diffraction patterns are obtained from the highly populated planes of Co_3O_4 (311) and CuO (111) & (-111) in the composite material.

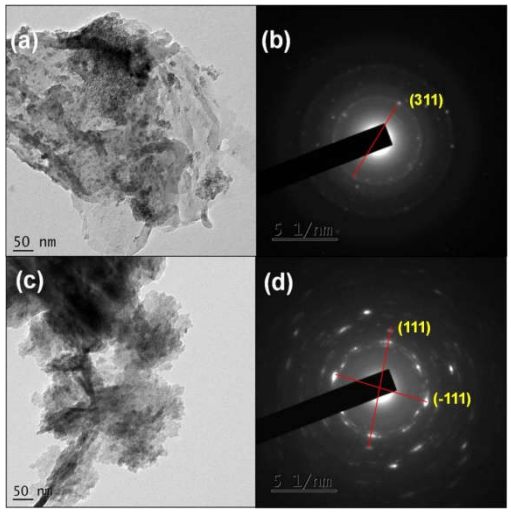

Figure 5. 5. (a), (c) TEM images of g-C_3N_4/Co_3O_4 and g-C_3N_4/CuO; (b), (d) Corresponding SAED patters.

5. 2. 5. Cyclic Voltammogram (CV)

The CV profiles of g-C_3N_4/CuO and g-C_3N_4/Co_3O_4 electrodes are shown in **Figure 5. 6**. The CV curve of an ideal supercapacitor material is expected to be in rectangular shape. In current (i)-voltage (v) curve, the value of current [i=C(v/t)] should be constant since for an ideal capacitor, the scan rate '(v/t)' and capacitance 'C' are constant.[18] In **Figure 5. 6(a),** the CV profiles of g-C_3N_4/Co_3O_4 electrodes shows a rectangular type CV and an excellent current response these are the characteristic features of an ideal capacitive material. The CV profile of g-C_3N_4/CuO electrodes (**Figure 5. 6b**) exhibits a small deviation from ideal capacitive behavior as compared to g-C_3N_4/Co_3O_4 electrode.

Figure 5. 7 show the variation in specific capacitance with scan rate for various supercapacitor electrodes. The electrochemical properties of composite electrodes were also compared with bare g-C_3N_4 in the same figure. The Csp value of all the electrodes were high at lower scan rate since the electrolyte molecule get enough time for their interaction with the electrode surface. The calculated value of specific capacitance (Csp) from CV profile for g-C_3N_4/CuO and g-C_3N_4/Co_3O_4 at a scan rate of 5 mVs^{-1} was found to be 238 Fg^{-1} and 108 Fg^{-1} respectively which are much greater than the Csp of bare g-C_3N_4 (74 Fg^{-1}). Compared to the electrochemical performance of bare g-C_3N_4, the composite samples, g-C_3N_4/CuO and g-C_3N_4/Co_3O_4 has shown excellent performance due to the psudocapacitive contribution from CuO and Co_3O_4 nanocrystals.[18]

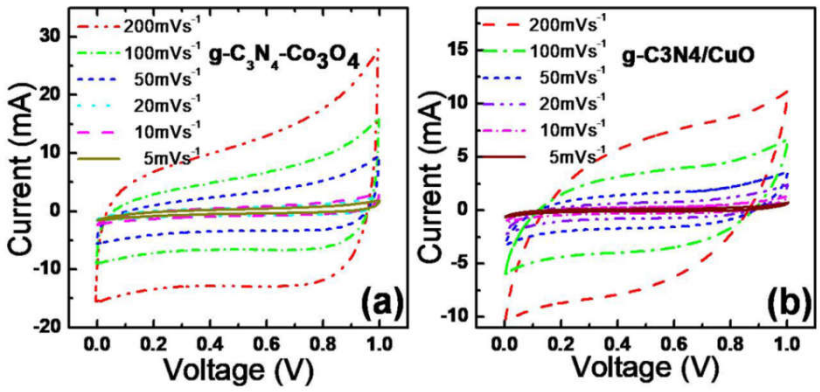

Figure 5. 6. Cyclic voltammograms of (a) g-C_3N_4/Co_3O_4 and (b) g-C_3N_4/CuO at different scan rates.

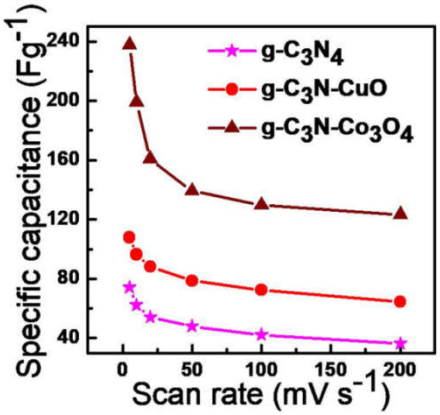

Figure 5. 7. Variation of specific capacitance of g-C_3N_4, g-C_3N_4/CuO and g-C_3N_4/Co_3O_4

5. 2. 6. Galvanostatic Charge-Discharge (GCD)

The actual device performance of the supercapacitor can be analyzed from the GCD experiments.[19] The GCD profile was performed in 2 M KOH solution at different current densities of 1, 2, 3, 4 and 5 Ag^{-1} and is shown in **Figure 5. 8.** Compared to g-C_3N_4/CuO **(Figure 5. 8b)**; g-C_3N_4/Co_3O_4 (**Figure 5. 8a)** supercapcitor electrodes exhibited almost triangular type GCD curve indicating an excellent efficiency for the

charge-discharge process. The IR drop value at the beginning of the discharge curve indicates the internal resistance of the electrode materials arising from electrical contact resistance, bulk solution resistance and resistance from ion migration. Compared to g-C_3N_4/CuO, the IR drop value of g-C_3N_4/Co_3O_4 is significantly lower which indicates good charge efficiency for g-C_3N_4/Co_3O_4 supercapacitor. The specific capacitance value of the devices were calculated from the GCD profiles using the equation, $Csp = \frac{2I}{m}(\frac{\Delta t}{\Delta v})$; where I is the discharge current, m is the mass of active material in a single electrode, Δt is the discharge time and Δv is the cell potential range after IR drop. The Csp value of the symmetric supercapacitors based on g-C_3N_4/CuO and g-C_3N_4/Co_3O_4 electrodes, calculated from GCD profiles at different current densities are given in **Table 5. 1**. The Csp value of g-C_3N_4/CuO and g-C_3N_4/Co_3O_4 electrodes at a current density of 1 Ag^{-1} was found to be 95 Fg^{-1} and 201 Fg^{-1} respectively. At high current densities, the Csp value of the devices decreases due to the limited interaction time between the electrode and electrolyte molecules.[20]

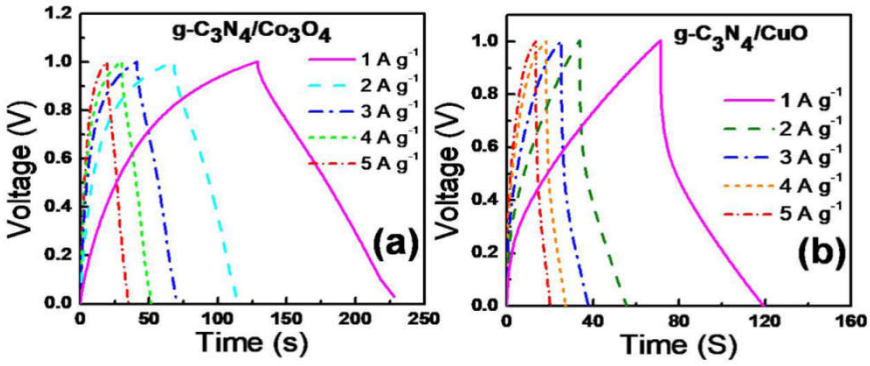

Figure 5. 8. GCD curves of (a) g-C_3N_4/Co_3O_4 and (b) g-C_3N_4/CuO based supercapacitors at a constant current density of 1 Ag^{-1} in 2 M KOH electrolyte.

Table 5. 1. Specific capacitance of g-C_3N_4/CuO and g-C_3N_4/Co_3O_4 calculated from GCD data.

Current density (Ag^{-1})	Csp (Fg^{-1}) g-C_3N_4/Co_3O_4	Csp (Fg^{-1}) g-C_3N_4/CuO
1	95	201
2	87	190
3	78	182
4	74	176
5	70	171

5. 2. 7. Cyclic Stability

The cyclic stability of the supercapacitor devices were analyzed from the charge-discharge profile under an applied current density of 5 Ag^{-1} for 6000 cycles and given as **Figure 5. 9**. The g-C_3N_4/Co_3O_4 based device has exhibited an excellent cyclic stability of 97% even after 6000 cycles. However, the stability of g-C_3N_4/CuO and g-C_3N_4 was found to be, 94% and 93% respectively. The agglomeration of the electrode material during electrochemical process could be a reason for the reduced cyclic stability in g-C_3N_4/CuO and g-C_3N_4 electrodes.

The energy density and power density of the device was calculated from the GCD profile by the relation; $E = \frac{1}{2} CspV^2$ and $P = E/\Delta t$. At a constant power density of 1 $kWkg^{-1}$, the energy density possessed by g-C_3N_4/Co_3O_4 and g-C_3N_4/CuO based devices are 27.9 $Whkg^{-1}$ and 13.2 $Whkg^{-1}$ respectively.

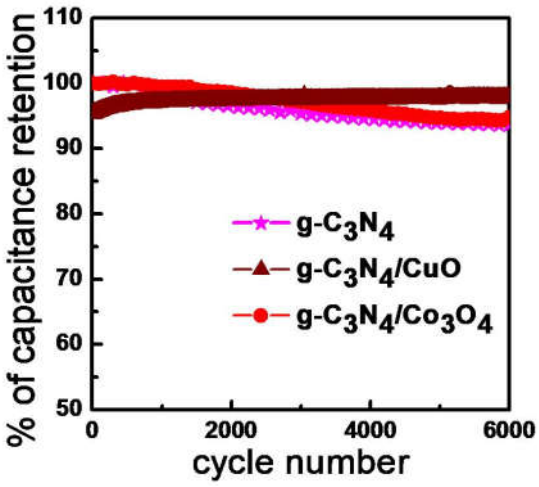

Figure 5. 9. Cyclic performance of the symmetric supercapacitors at a constant current density of 5 Ag^{-1}.

5. 2. 7. Electrochemical Impedance Spectra (EIS)

EIS or Nyquist spectra of the electrode materials were performed to further analyze the performance of the devices (**Figure 5. 10**). The EIS spectra consist of a semicircle at high frequency region and a vertical line at the low frequency region. The radius of the semicircle (Rct) gives the value of charge transport resistance of the electrode material. A small arc radius in EIS spectra indicates a better charge transport at the electrode-electrolyte interface.[21] In the present case the Rct value of g-C_3N_4/Co_3O_4 (**Figure 5. 10a)** is very small compared to g-C_3N_4/CuO (**Figure 5. 10b)** electrodes indicating an excellent charge transport in g-C_3N_4/Co_3O_4 electrode. The low frequency region of the impedance spectra is associated with the diffusion of ions from the bulk of the solution to the electrode surface. A vertical line parallel to y-axis of the plot is the ideal condition for a supercapacitor material. It can be seen that, for g-C_3N_4/Co_3O_4 electrodes the straight line at low frequency region is more vertical than the other electrode. Moreover,

the length of the straight line is very small (less imaginary part) in g-C_3N_4/Co_3O_4 electrodes designating a lower resistance for ion diffusion from the bulk of the solution to electrode surface.[22]

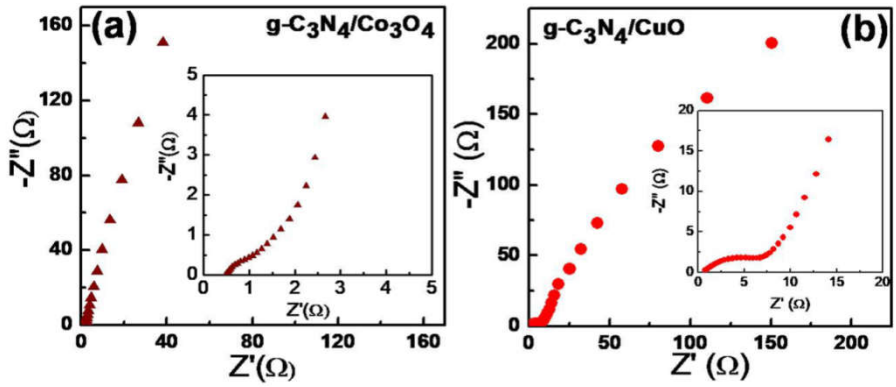

Figure 5. 10. Nyquist plots of (a) g-C_3N_4/Co_3O_4 and (b) g-C_3N_4/CuO based supercapacitor devices at dc bias of 0 V with sinusoidal signal of 5 mV over the frequency range from 100 kHz and 1 MHz.

5. 3. Conclusions

In summary, pseudocapacitive Co_3O_4 and CuO nanoparticles were anchored on the surface of the two dimensional g-C_3N_4 by direct precipitation method. g-C_3N_4/Co_3O_4 and g-C_3N_4/CuO nano hybrid materials were used as cost effective electrodes in symmetric supercapacitor devices. The electrochemical performance of g-C_3N_4 have shown significant enhancement by coupling with Co_3O_4 and CuO with a specific capacitance of 201 Fg^{-1} and 95 Fg^{-1} for g-C_3N_4/Co_3O_4 and g-C_3N_4/CuO composite materials respectively. The enhancement in electrochemical properties in composite sample can be attributed to the presence of pseudocapacitive metal oxide phases. The g-C_3N_4/Co_3O_4 exhibited a cyclic stability of 97 % even after 6000 cycles with an energy density of 27.9 $Whkg^{-1}$.

References

1. M. R. Palacin, A. Guibert, *Science*, 2016, 351, 1253292.
2. M. D. Stoller, R. S. Ruoff, *Energy Environ. Sci*., 2010, 3, 1294.
3. J. Kavil, P. M. Anjana, C. P. Roshni, P. Periyat, K. G. Raj, R. B. Rakhi, *Appl. Surf. Sci*., 2019, 487, 109.
4. L. L. Zhang, X. S. Zhao, *Chem. Soc. Rev*., 2009, 38, 2520.
5. L. F. Chen, X. D. Zhang, H. W. Liang, M. Kong, Q. F. Guan, P. Chen, Z. Y. Wu, S. H. Yu, *ACS Nano*, 2012, 6, 7092.
6. Y. Gong, M. Li, Y. Wang, *Chem. Sus. Chem*., 2015, 8, 931.
7. J. Kavil, P. M. Anjana, P. Periyat, R. B. Rakhi, *J. Mater. Sci. Mater. Electron*., 2018, 29, 16598.
8. J. Kavil, P. M. Anjana, P. Periyat, R. B. Rakhi, *Sustainable Energy & Fuels*, 2018, 2, 2244.
9. Q. Guan, J. Cheng, B. Wang, W. Ni, G. Gu, X. Li, L. Huang, G. Yang, F. Nie, *ACS Appl. Surf. Iterfaces*, 2014, 6, 7626.
10. A. Pendashteh, M. F. Mousavi, M. S. Rahmanifar, *Electrochim. Acta*, 2013, 15, 347.
11. H. L. Zhu, Y. Q. Zheng, *Electrochim. Acta*, 2018, 265, 372.
12. S. P. Vattikuti, B. P. Reddy, C. Byon, J. Shim, *J. Solid State Chem*., 2018, 262, 106.
13. R. B. Rakhi, W. Chen, M. N. Hedhili, D. Cha, H. N. Alshareef, *ACS Appl. Surf. Iterfaces*, 2014, 6, 4196.
14. G. Liao, S. Chen, X. Quan, H. Yu, H. Zhao, *J. Mater. Chem*., 2012, 22, 2721.
15. A. Pendashteh, M. F. Mousavi, M. S. Rahmanifar, *Electrochim. Acta*, 2013, 88, 347.
16. M. C. Biesinger, B. P. Payne, A. P. Grosvenor, L. W. Lau, A. R. Gerson, R. S. Smart, *Appl. Surf. Sci*., 2011, 257, 2717.

17. M. C. Biesinger, L. W. Lau, A. R. Gerson, R. S. Smart, *Appl. Surf. Sci*., 2010, 257, 887.

18. Q. Guan, J. Cheng, B. Wang, W. Ni, G. Gu, X. Li, L. Huang, G. Yang, F. Nie, *ACS Appl. Surf. Iterfaces*, 2014, 6, 7626.

19. B. Babu, S. G. Ullattil, R. Prasannachandran, J. Kavil, P. Periyat, M. M. Shaijumon, *ACS Sustain. Chem. Eng*., 2018, 6, 5401.

20. D. Jiang, Q. Xu, S. Meng, C. Xia, M. Chen, *J. Alloys Compd.*, 2017, 706, 41.

21. R. B. Rakhi, B. Ahmed, D. Anjum and H. N. Alshareef, *ACS Appl. Mater. Interfaces*, 2016, 8, 18806.

22. W. Qi, R. Lv, B. Na, H. Liu, Y. He, N. Yu, *Acs Sustain. Chem. Eng*., 2018, 6, 4739.

Chapter Six

Multifunctional nanohybrid material from discarded razor blades as cost-effective supercapacitor electrodes and oil-spill cleaners

Contents

6. 1. Introduction

The industrialization and the population explosion have to lead to an unparallel explosion and diversity in the generation of waste materials. The waste management demands an immediate and scientific approach for socio-economic development and environmental protection. The concept of "closed economy production model" or regenerative economy contemplates the garbages as the resource that promotes a novel and sustainable developmental strategy by minimizing the landfills.[1] Closed economy minimizes the environmental pollution and depletion of resources by reducing, reusing and recycling (3R) of the waste material. Clean energy technology and a clean environment are inevitable for the sustainable development of the society.[2] Last few decades, the researchers and policymakers have been searching for functional materials that can be used for renewable energy conversion, storage and simultaneously for environmental remediation.

In recent years, supercapacitors have received an increasing interest in energy storage technology owing to its superior electrochemical properties than the conventional batteries.[3,4] As evidenced from the 'Ragon-plot'**(Figure 1. 3)**, supercapacitors provide much higher power density than conventional batteries and energy density than dielectric capacitors. Supercapacitor technology has been explored tremendously as an environmentally benign energy resource in recent years surely due to the development of a wide range of nanostructured materials from researchers all over the world.[5] Attempts were reported recently to fabricate supercapacitor electrodes from waste materials as a green approach to attain the global goal of sustainable development. Garbages such as tires, biomass, plastic wastes were used as the prospective source of activated carbon for supercapacitor applications.[6-9] However, to the best our knowledge, there are no reports for the fabrication of nanosemiconductor hybrid materials from discarded materials with multifunctional utility in energy storage and environmental applications.

The contamination of water by different chemical substances is one of the lethal issues faced around the globe. Among the various contaminants, oil spills generated from damaged pipelines, tankers, and rigs are considered as the one of the worst environmental concern caused by human activity. Oil spills are known to cause severe long-term damages to the aquatic environment by which the entire aquatic ecosystem gets destabilized.[10] Conventional methods for the clean-up process such as skimming, hot water spraying and burning cause damage to the aquatic organisms. Due to the simplicity in application,

the organophilic sorbent materials like organic polymers, zeolites and graphenes have received considerable attention recently. To make the process viable, large quantities of oil have to be removed from the spillage quite instantaneously using a low-cost sorbent. The most common strategy is to employ magnetic adsorbents which can instantaneously remove oil from spills utilizing the hydrophobic interactions with oil molecules followed by magnetic separation.[11] Generally, iron oxide nanoparticles (Fe_2O_3) are attached to various low-cost adsorbents for oil removal.[12,13] Therefore, the cost-effectiveness of adsorbent materials is mostly limited by the cost of iron-oxide in the adsorbent composite.

Fe_2O_3 based nanohybrid materials have been considered as a suitable candidates for supecapacitor electrodes as well owing to its environmentally and economically benign nature.[14] Moreover, the material exhibit excellent electrochemical performance due to its pesudocapacitive behavior. Fe_2O_3@carbon (CFO) hybrid materials were introduced to further enhance the cyclic stability and specific capacitance of Fe_2O_3 (FO) based electrodes. Various recent reports are available on the synthesis and supercapacitor applications of Fe_2O_3@C based nanomaterials.[15-18] However, as mentioned earlier there are no reports on the synthesis of multi functional Fe_2O_3@C nano-hetero structures by considering the concept of 'closed economy'. Moreover in most of the literatures, the supercapcitors studies of Fe_2O_3@C were mostly carried out in three electrode configuration. Compared to three electrode configuration, two electrode systems are suitable for evaluating the performance of the supercapcitors.[5]

The highlight of the present work is the attempt to fabricate multifunctional nano-hybrid structures; Fe_2O_3@carbon from used razor blades and glucose as precursors. The hybrid structures were successfully used as electrode materials in symmetric supercapacitor devices *(Two electrode configuration)* for energy storage application and the materials were also employed as magnetically separable oil spill removers for environmental remediation. This new approach makes the process more cost-effective and sustainable.

6. 2. Results and Discussion

Fe_2O_3@C (CFO) nano-hybrid structures were prepared from discarded razor blades and glucose solution as represented in **Scheme 6. 1**

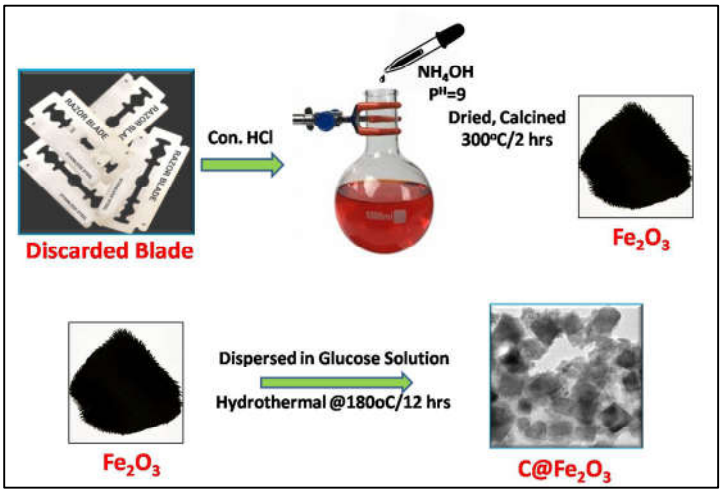

Scheme 6. 1. Shematic representation of the formation of Fe_2O_3@C (CFO) nano-heterostructures.

6. 2. 1. XRD analysis

The crystal structure analysis depicted in **Figure 6. 1(a)** reveals the presence of room temperature stable, cubic maghemite phase of Fe_2O_3 in the razor blade derived iron oxide sample. The observed peaks at 2θ values 30.1°, 35.4°, 43.0°, 53.1°, 57.0° and 62.5° matches with the JCPDS file no. 39-1346 of γ- Fe_2O_3.[12,20] The corresponding diffraction planes are (220), (311), (400), (422), (511) and (440) of γ- Fe_2O_3 with normal spinel structure.[12,20] The average crystallite size (D) calculated using Scherrer equation, $D=0.9\lambda/\beta\cos\theta$ (λ is the wavelength of CuKα radiation, β is the FWHM and θ is the peak position) for Fe_2O_3 and Fe_2O_3@C is 25 nm and 28 nm respectively. In the case of Fe_2O_3@C, the less intense (100) and (002) reflections of carbon shell is masked by the crystalline reflections from Fe_2O_3.[12]

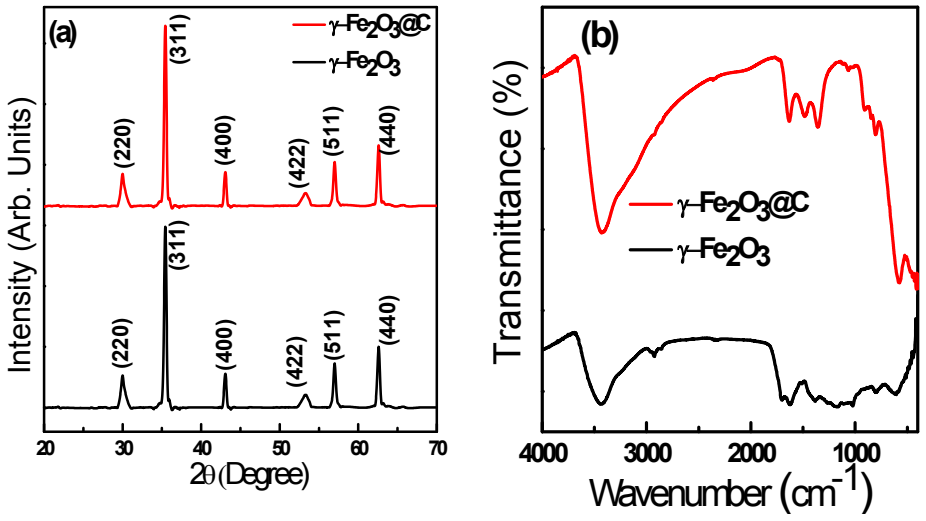

Figure 6. 1. (a) X-ray diffraction pattern and (b) FTIR spectra of the razor blade derived γ- Fe_2O_3 (FO) and γ- Fe_2O_3@C (CFO).

6. 2. 2. FTIR Spectral analysis

FTIR spectral analyses of the samples were carried out to confirm the formation of Fe_2O_3 and its hetero-junction species with carbon. The absorption bands in **Figure 6. 1(b)** at 585-610 cm^{-1} represents the stretching vibrations of Fe-O bonds.[13] The Fe-O vibration modes of CFO sample exhibit sharp absorption bands owing to the further crystallization of Fe_2O_3 phases during hydrothermal treatment for the deposition of carbon species. The broad absorption peaks at around 3430 cm^{-1} in both the samples indicate the presence of adsorbed hydroxyls species on the surface of the material. The presence of absorption band in CFO at around 1640-1350 cm^{-1} can be attributed to the C-O stretching vibrations of carboxylate anions adsorbed during the hydrothermal carbonization of glucose molecules on Fe_2O_3 nanocrystals.[22,23] The FTIR studies show that the CFO possesses enough adsorbed functionalities on the surface of the sample which facilitate an excellent wettability between the electrode-electrolyte species for enhanced electrochemical properties.

6. 2. 3. TEM Analysis

The microstructure characterization of the carbon-coated Fe_2O_3 nano-hybrid structure (CFO) is depicted in **Figure 6. 2**. The TEM images clearly show that the crystalline Fe_2O_3 phases are in plate-like morphology with particle size upto 50 nm. The formation of the hybrid structure between Fe_2O_3 flakes and carbon is evident from the low-resolution images. The SAED patterns with bright spots indicate a highly crystalline nature for the derived Fe_2O_3 phases in CFO sample due to the presence of more crystalline phase orientation of Fe_2O_3 during the hydrothermal carbonization process at 180 °C for 24 h.

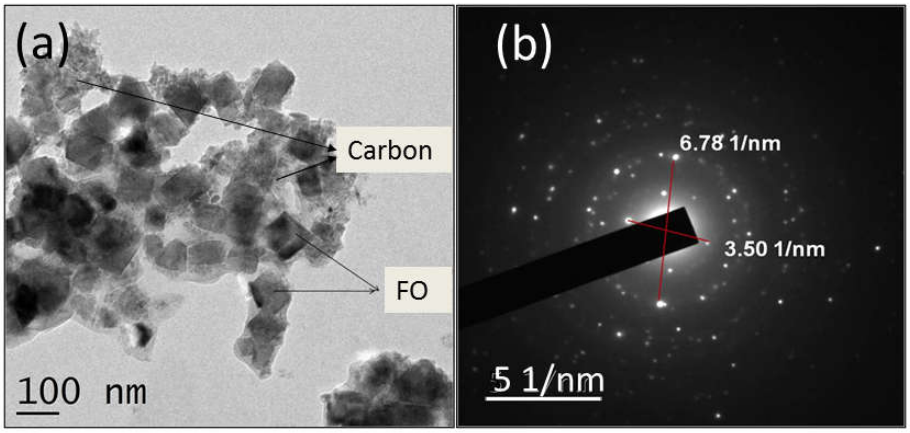

Figure 6. 2. (a) TEM image of Fe_2O_3@C nano-heterostructure and (b) the corresponding SAED pattern.

6. 2. 4. FESEM-EDS analysis

The elemental analysis of the as prepared Fe_2O_3 (FO) and the composite sample CFO were analyzed from a FESEM instrument attached with Energy dispersive X-ray spectroscopy (EDS) **Figure 6. 3(a)** shows that the prepared Fe_2O_3 sample contains small amount of other elements such as C, Ni and Cr which is attributed to the contribution from the stainless steel of razor blades. The razor blade steel usually consists of about 12-14 % chromium. However in the prepared Fe_2O_3 sample the composition Cr is negligibly small since at the experimental pH of 9, only $Fe(OH)_2$ get precipitated due to the higher solubility product of $Fe(OH)_2$ than $Cr(OH)_3$. The EDS results of CFO sample in **Figure 6. 3(b)** indicated that the carbon content of the composite sample get enhanced when compared to FO sample due to the deposition of carbon on Fe_2O_3 crystals due to the hydrothermal carbonization of glucose molecule.

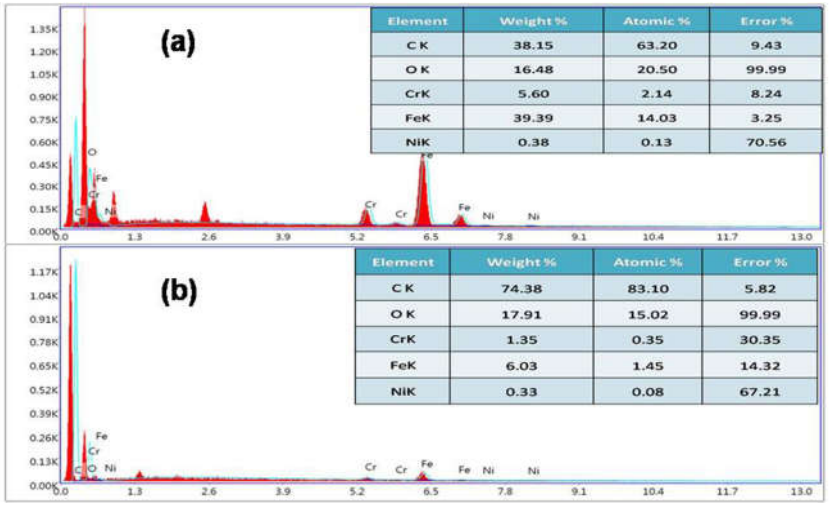

Figure 6. 3. FESEM-EDS analysis of (a) Prepared Fe_2O_3 from discarded razor blades and (b) composite sample Fe_2O_3@Carbon.

6. 2. 5. BET-Surface area analysis

BET surface area measurements of FO and CFO were carried out by analyzing the nitrogen adsorption-desorption isotherms of samples (**Figure 6. 4**). The samples exhibited a type IV physisorption curve with H3 hysteresis loop characteristics of a mesoporous material.[4] However, the area of the hysteresis loop is very narrow due to the limited average pore size (4 nm) possessed by the samples. The adsorption studies indicated that the BET surface area of both the samples; FO and CFO were in the same range of 49 and 50 m^2g^{-1} respectively. The results indicate that in the present study, the carbon coating does not make any changes in the surface area of the composite materials.

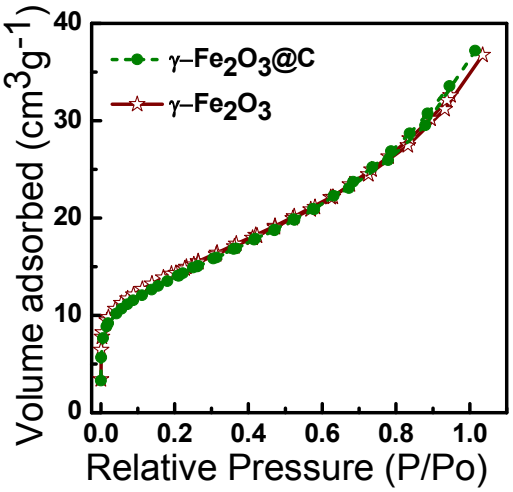

Figure 6. 4. BET N_2 adsorption isotherms of FO and CFO samples.

6. 2. 6. Cyclic Voltammogram (CV)

The electrochemical performance of the fabricated symmetric supercapacitors based on FO and CFO samples were evaluated from the cyclic voltammograms (CV) at different scan rate of 5, 10, 20, 50, 100, 200 mVs^{-1} within a potential window of 0 to 1 V **(Figure 6. 5)**. The FO electrode in **Figure 6. 5(a)** exhibited a pair of oxidation and reduction peaks corresponds to the pseudocapacitive behavior of bare Fe_2O_3 in KOH electrolyte based on the redox reaction **(equation 6.1),**

$$Fe_2O_3 + M^+ + 2e^- \leftrightarrow Fe_2O_3M, \text{ where } M = K^+ \text{ or } H_3O^+.^{14} \qquad \textbf{(6. 1)}$$

Compared to FO electrode, CFO electrode (**Figure 6. 5b**) show superior electrochemical performance with a nearly rectangular type CV curve which is the characteristic feature of an ideal capacitor material.[1] The excellent charge storage properties of CFO electrode can be attributed to their synergic effect of faradaic and non-faradaic process of charge storage mechanism.[24] In CFO sample carbon

particles were coated uniformly on the Fe_2O_3 particles as observable from the TEM images. The carbon layer acts as a template for the formation of electrical double layer (EDLC) at the electrode-electrolyte interface which suppresses the redox peaks originated from the pseudocapacitive behavior of bare Fe_2O_3.[14] Moreover, as evidenced by IR studies the carbon layers render more functionality on the electrode surface, which is advantageous for the effective wettability between the electrode material and electrolyte molecules.

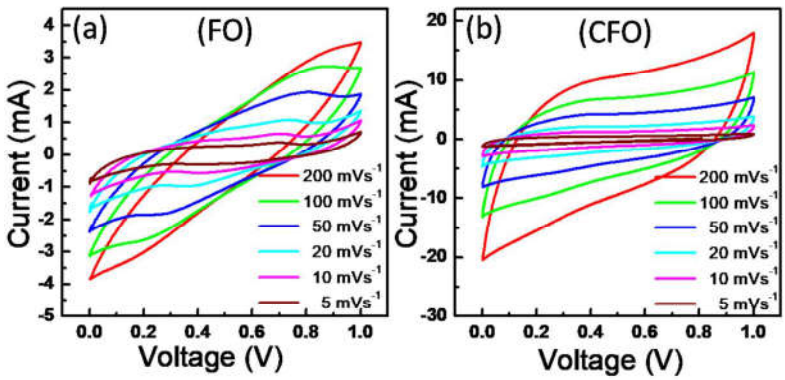

Figure 6. 5. (a) & (b) CV curves of supercapacitors based on FO and CFO electrodes at different scan rates.

6. 2. 7. Galvanostatic Charge-discharge (CD) curves

Supercapacitor performance of the electrode materials was further analyzed by galvanostatic charge-discharge (CD) studies (**Figure 6. 6a and Figure 6. 6b**). The analysis were carried out at different current densities of 1, 2, 3, 4 and 5 Ag^{-1} in the potential range between 0 to +1 V. GCD measurements are significant to analyze the performance of the device under practical operating conditions. As shown in **Figure 6. 6(b)**, the CFO sample exhibited a symmetrical type charge-discharge

curve showing a linear relationship between potential and time.[25] The IR drop of CFO electrode is very minimal compared to FO electrode which indicates that CFO had low internal resistance and the considerable charge-discharge duration in CFO denotes a much higher specific capacitance for the composite electrode. At a constant current density of 1 Ag^{-1}; CFO sample exhibited the highest specific capacitance value of 285. 6 Fg^{-1} which is almost two-fold the specific capacitance FO electrode (122.7 Fg^{-1}). At a constant power density of 1 $kWkg^{-1}$, the energy density possessed by FO and CFO electrode based supercapacitors were E=22.52 $Whkg^{-1}$ and 37.88 $Whkg^{-1}$ respectively. The energy density (energy stored per unit mass of the materials) was calculated by the relation, $E=1/2\ C_{sp}V_i^2$, where C_{sp} is the specific capacitance, and V_i is the initial voltage of the discharge curve. The electrochemical performance of the Fe_2O_3@C (CFO) electrodes was compared in **Table 6. 1** with recent literature reports on the same materials. The CFO electrode has shown much higher electrochemical properties than the reported results.

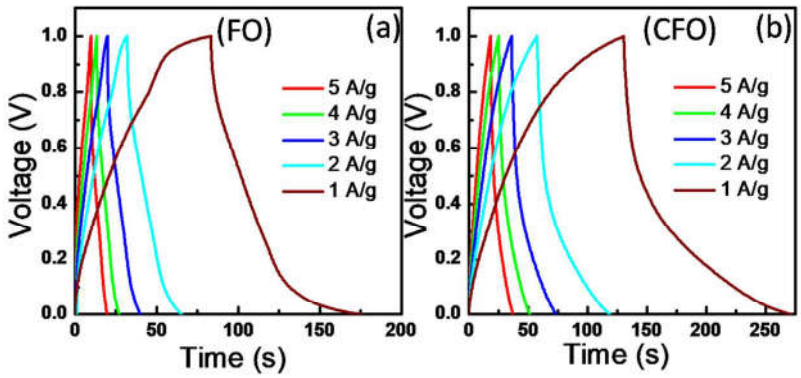

Figure 6. 6. (a) & (b) GCD curves of FO and CFO based supercapacitors at a constant current density of 1 Ag^{-1} in 2 M KOH electrolyte.

Table 6. 1. Recent reports on the electrochemical properties of Fe_2O_3@C hybrid materials.

Electrode material	Electrolyte	Current density (Ag^{-1})	Specific capacitance (Fg^{-1})	Electrode configuration	Ref.
α-Fe_2O_3@C	1M KOH	1	288	Three electrode	15
α-Fe_2O_3@C	1M H_3PO_4	1.5	249	Three electrode	16
Fe_2O_3@C	5M KOH	0.5	612	Three electrode	17
Fe_2O_3@AC	6M KOH	1	240	Three electrode	18
Fe_2O_3/C	1M Na_2SO_3	0.5	235	Three electrode	26
γ- Fe_2O_3@C	1M KOH	1	285	Two electrode	This work

The enhanced electrochemical performance in CFO electrode can be attributed to the very high BET surface area possessed by this sample which provides more reactive sites for the electrochemical interaction between electrode and electrolyte molecule. Moreover, in CFO two types of charge storage mechanism operates; i) faradaic process due to the presence of pseudocapacitive Fe_2O_3 phase ii) non-faradaic process of charge storage owing to the presence of carbon moiety on the Fe_2O_3 phase.

The variation of the specific capacitance of the material at different scan rates and current densities is shown in **Figure 6. 7(a)** and **Figure 6. 7(b)** respectively. The specific capacitance of both the electrodes decreases at higher scan rate and high current density. Under this conditions electrolyte molecules are provided with less time for the electrode-electrolyte interaction. However, at lower san rates and current densities, the electrolyte molecules get sufficient time to

interact with the electrode material which results in the enhancement in the specific capacitance of the device.

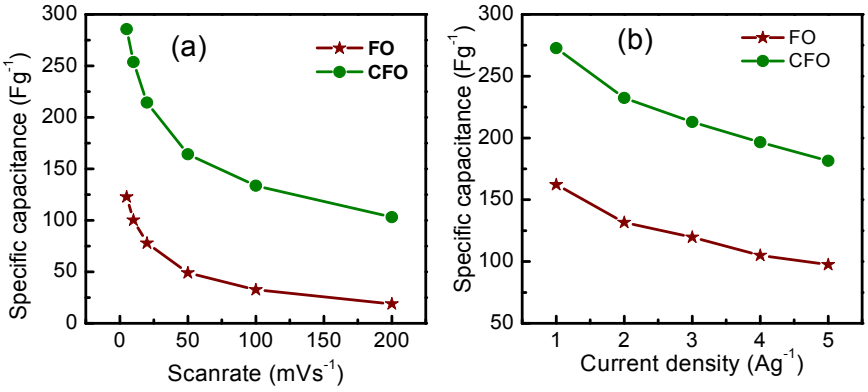

Figure 6. 7. Variation of Specific capacitance of FO and CFO based symmetric supercapacitors at different (a) scan rates and (b) current densities.

6. 2. 8. Cyclic Stability

The cyclic stability is a crucial factor for the commercialization of the supercapacitor device. The stability was evaluated by performing the charge-discharge measurements for 5000 cycles at a constant current density of 5 Ag^{-1} in the potential range of 0 to +1 V. The specific capacitance was plotted as a function of the number of cycles and given as **Figure 6. 8**. The symmetric supercapacitor fabricated from CFO electrode has shown excellent cyclic stability and the stability was found to be increasing with the number of cycles after an initial drop of 8 % around 250 cycles. After 5000 cycles, the capacitance retention of the supercapacitor fabricated from the composite sample CFO was found to be ~98 %, and that of FO was only 74 % of that of the respective initial capacitances.

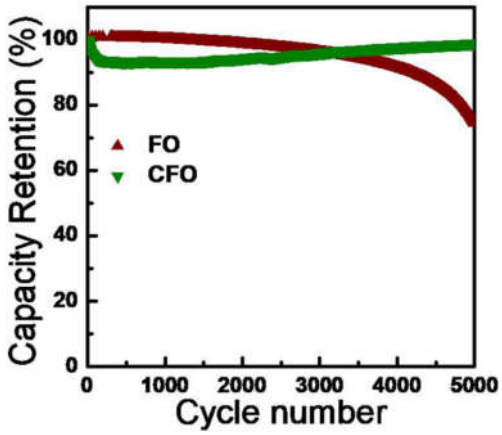

Figure 6. 8. Cycling performance of FO and CFO based symmetric supercapacitors at a constant current density of 5 Ag^{-1}.

6. 2. 9. Electrochemical Impedance Spectroscopy (EIS)

The electrochemical impedance Spectra (EIS) of the symmetric supercapacitors fabricated from FO and CFO electrodes are shown in **Figure 6. 9**. The plots show a semicircle in the high-frequency region and a straight line in the low-frequency region. The intercept of the semicircle at high-frequency region indicates the solution resistance (R_s) of the electrolyte.[27,28] Both the electrodes exhibit the same R_s value of 0.7 Ω in the aqueous KOH electrolyte. The radius of the semicircle at the high-frequency region indicated the charge transfer resistance (*Rct*) at the interface of the electrode. In the present experiment, the CFO electrode has exhibited a smaller R_{ct} value (5 Ω) as compared to FO (75 Ω) electrode indicating an effective charge transport at the electrode-electrolyte interface. A straight line at the low-frequency region (Warburg line) of the Nyquist plot which makes an angle 45° with real axis, determines the frequency dependent ion diffusion at the electrode-electrolyte interface. The inclination of the straight line

towards the vertical axis of the plot in CFO electrode indicates an ideal capacitive behavior in the carbon-doped sample. The enhancement in the electrochemical behavior in CFO electrode can be due to the presence of surface functional groups and the synergic effect of two charge storage mechanisms operates in the Fe_2O_3@C sample.[28]

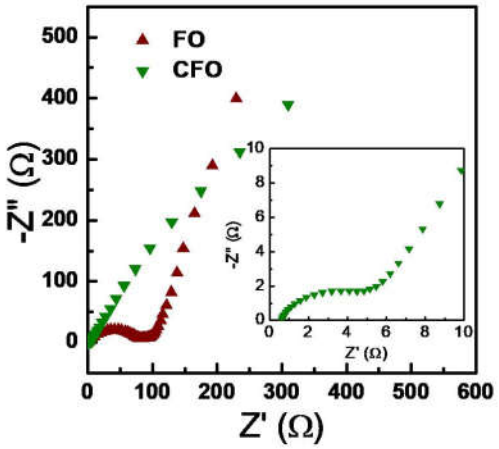

Figure 6. 9. EIS spectra for symmetric supercapacitors based on FO and CFO electrodes at a dc bias of 0 V with sinusoidal signal of 5 mV over the frequency range from 100 kHz and 1 MHz.

6. 2. 9. Environmental Application: Oil-Spill Removal

The Fe_2O_3@C composite material (CFO) was applied for the removal of oil spills from water. The oil removal efficiency of the material was tested after creating an artificial oil spill in the laboratory using commercial engine oil. CFO was smeared on top of the spilled oil and then recovered using a permanent magnet. The oil retention studies in **Figure 6. 10** indicated that the adsorbent material is capable of removing oil upto 5 times its weight. The snapshots of the different steps of oil removal process are given in **Figure 6. 11**. The oil

adsorption by the material is quite instantaneous, making CFO an attractive candidate for the oil removal process. The oil removal capacity of CFO is comparable to the iron oxide-carbon core-shell system with triethoxysilane modified surface and macroporous Fe/C nanocomposites reported in literature.[29-30] Even though the oil removal capacity of CFO is lower when compared to many of the materials reported in the literature like nitrogen doped graphene framework,[31] hybrid graphene-carbon nanotube foam,[32] polymer hybrid nanoparticles,[33] CNT sponges,[34] *etc*. The hybrid material, CFO still is a superior in terms of applicability since they are far more cost effective than these materials. The oil removal capacity of CFO might be limited by the surface functional groups as evident from the IR **(Figure 6. 1b)** studies. Therefore, it is possible to engineer CFO as a better oil removing agent by minimizing the polar surface functional groups and thereby making it much more lyophilic.

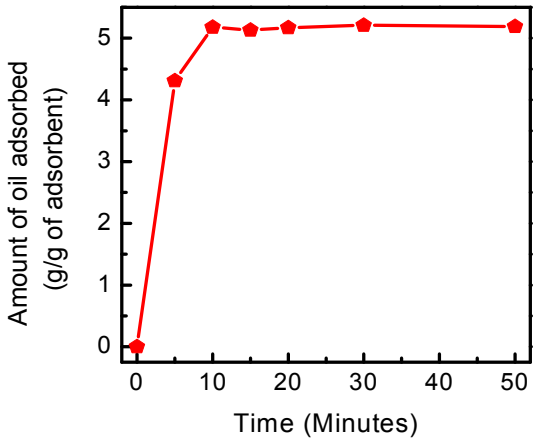

Figure 6. 10. Oil retention capacity of CFO as a function of time, using commercial engine oil.

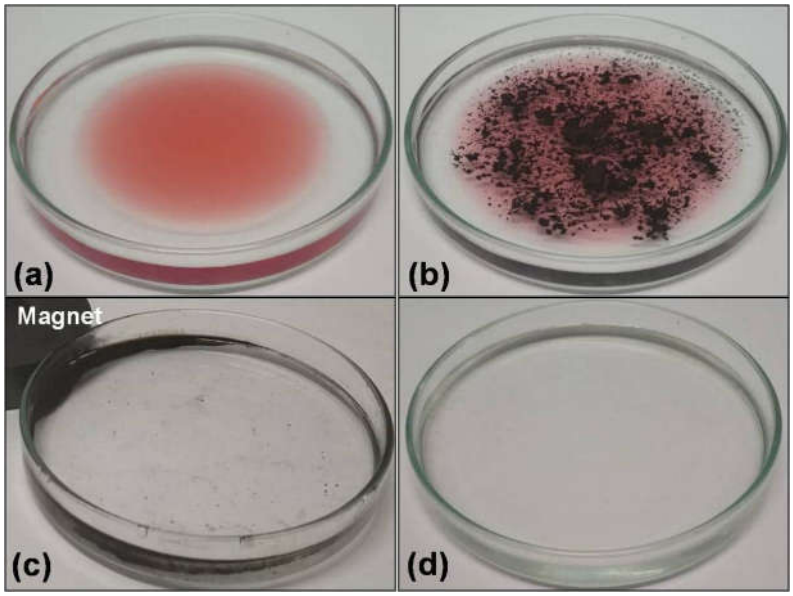

Figure 6. 11. Snapshots of different stages of oil removal process. (a) Oil spilled over water (b) Fe_2O_3@C (CFO) dispersed over oil-water mixture (c) The adsorbent along with the oil is recovered by an external magnet (d) clear water after the removal of oil and adsorbent.

6. 3. Conclusions

Fe_2O_3@carbon (CFO) nano-heterostructures were fabricated from the discarded razor blades and glucose solution by considering the concept of regenerative economy. Hydrothermally prepared hybrid material exhibited multifunctional applications in energy storage and environmental remediation. The symmetric supercapacitor device fabricated from CFO has exhibited a specific capacitance value of 285. 6 Fg^{-1} with an outstanding capacitive retention of ~98 % after 5000 cycles. The CFO sample was successfully employed as an efficient magnetically recoverable adsorbent for the removal oil spills from water. The oil removal efficiency of CFO was found to 5 g oil per 1 g of adsorbent with the assistance of an external magnet.

References

1. A. Murray, K. Skene, K. Haynes, *J. Bus. Ethics*, 2017, 140, 369.

2. Y. Geng, J. Sarkis, S. Ulgiati, P. Zhang, *Science*, 2013, 339, 1526.

3. M. D. Stoller, R. S. Ruoff, *Energy Environ. Sci*., 2010, 3, 1294.

4. J. Kavil, P. M. Anjana, P. Periyat, R. B. Rakhi, *Sustainable Energy & Fuels*, 2018, 2, 2244.

5. J. Kavil, P. M. Anjana, P. Periyat, R. B. Rakhi, *J. Mater. Sci. Mater. Electron*., 2018, 29, 16598.

6. Y. Chang, Y. Pang, Q. Dang, A. Kumar, G. Zhang, Z. Chang, X. Sun, *ACS Appl. Energy Mater*., 2018, 1, 5685.

7. H. Chen, F. Yu, G. Wang, L. Chen, B. Dai, S. Peng, *ACS Omega,* 2018, 3, 4724.

8. P. Yu, Y. Liang, H. Dong, H. Hu, S. Liu, L. Peng, M. Zheng, Y. Xiao, Y. Liu, *ACS Sustain. Chem. Eng.,* 2018, 6, 15325.

9. Y. Chang, Y. Pang, Q. Dang, A. Kumar, G. Zhang, Z. Chang, X. Sun, *ACS Appl. Energy Mater.,* 2018, 1, 5685.

10. M. O. Adebajo, R. L. Frost, J. T. Kloprogge, O. Carmody, S. Kokot, *J. Porous Mater*., 2003, 10, 159.

11. P. Thanikaivelan, N. T. Narayanan, B. K. Pradhan and P. M. Ajayan, *Sci. Rep.*, 2012, 2, 1.

12. K. G. Raj and P. A. Joy, *Journal of environmental chemical engineering*, 2015, 3, 2068.

13. M. O. Adebajo, R. L. Frost, J. T. Kloprogge, O. Carmody, S. Kokot, *J. Porous Mat*., 2003, 10, 159.

14. V. D Nithya, N. S Arul, *J. Power Sources*, 2016, 30, 297.

15. M. Zhu, J Kan, J Pan, W. Tong, Q. Chen, J. Wang, S. Li, *J. Energ. Chem*., 2019, 1, 1.

16. N. K. Chaudhari, S. Chaudhari, J. S. Yu, *Chem. Sus. Chem*., 2014, 7, 3102.

17. Y. Ye, H. Zhang, Y. Chen, P. Deng, Z. Huang, L. Liu, Y. Qian, Y. Li, Q. Li, *J. Alloy. Compound.*, 2015, 5, 422.

18. Y. Li, L. Kang, G. Bai, P. Li, J. Deng, X. Liu, Y, Yang, F. Gao, W. Liang, *Electrochim. Acta*., 2014, 10, 67.

19. A. I. Vogel, Longmans, Green and Co. London, New York, Toronto, 5 th edition, 2013, 437.

20. S. Babar, N. Gavade, H. Shinde, P. Mahajan, K. H. Lee, N. Mane, A. Deshmukh, K. Garadkar, V. Bhuse, *ACS Appl. Nano Mater*., 2018, 1, 4682.

21. V. Khomenko, E. Frackowiak, F. Béguin, *Electrochim. Acta*, 2005, 50, 2499.

22. S. Biniak, G. Szymanski, J. Siedlewski and A. Swiatkowski, *Carbon*, 1997, 35, 1799.

23. B. Babu, S. G. Ullattil, R. Prasannachandran, J. Kavil, P. Periyat, M. M. Shaijumon, *Acs Sustain. Chem. Eng*., 2018, 6, 5401.

24. A. Borenstein, O. Hanna, R. Attias, S. Luski, T. Brousse, D. Aurbach, *J. Mater. Chem. A*, 2017, 5, 12653.

25. B. Liu, M. Yang, H. Chen, Y. Liu, D. Yang, H. Li, *J. Power Sources*, 2018, 397, 1.

26. Y. Lin, X. Wang, G. Qian, J. J. Watkins, *Chem. Mater*., 2014, 26 (6), 2128-2137.

27. R. B. Rakhi, B. Ahmed, D. Anjum, H. N. Alshareef, *ACS Appl. Mater. Interfaces*, 2016, 8, 18806.

28. W. Qi, R. Lv, B. Na, H. Liu, Y. He, N. Yu, *Acs Sustain. Chem. Eng*., 2018, 6, 4739.

29. Q. Zhu, F. Tao, Q. Pan, *ACS Appl. Mater. Interfaces*, 2010, 2, 3141.

30. Y. Chu, Q. Pan, *ACS Appl. Mater. Interfaces*, 2012, 4, 2420.

31. Y. Zhao, C. Hu, Y. Hu, H. Cheng, G. Shi and L. Qu, *Angew. Chem. Inter. Ed*., 2012, 51, 11371.

32. X. Dong, J Chen, Y. Ma, J. Wang, M. B. Chan-Park, X. Liu, L. Wang, W. Huang, P. Chen*, Chem. Comm*., 2012, 48, 10660.

33. A. Pavia-Sanders, S. Zhang, J. A. Flores, J. E. Sanders, J. E. Raymond, K. L. Wooley, *ACS nano*, 2013, 7, 7552.

34. X. Gui, J. Wei, K. Wang, A. Cao, H. Zhu, Y. Jia, Q. Shu, D. Wu, *Adv. Mater.*, 2010, 22, 617.

Chapter Seven

CdS Senzitized TiO_2 Nanoheterostructures as Sunlight Driven Photocatalyst

Contents

7. 1. Introduction

TiO_2 based heterogeneous catalysis becomes an efficient technique for the photocatalytic oxidative removal of dissolved organic and inorganic contaminants in water due to its cost effectiveness, and the distinctive photocatalytic activity.[1-4] It is the bandgap energy of TiO_2 (3.2 eV) that limits its application as solar energy harvesting photocatalyst.[5,6] Visible light response of TiO_2 has been modified by various approaches such as metal and non-metal doping in an attempt to tailor the band gap[7,8] photosensitization by anchoring organic chromophores,[9] *etc*. In recent years heterojunction photocatalyst fabrication *via* hybridizing TiO_2 with suitable narrow band gap semiconductors such as CdS, Cu_2O, ZnO, *etc* had received considerable attention among the scientific community due to its excellent light absorption ability, improved photocatalysis and photo stability.[10-12]

CdS act as an excellent sunlight harvesting material owing to its narrow band gap (2.4 eV) and can be used as a sensitizer for wide band gap semiconductors.[13] Valence band and conduction band levels of CdS semiconductor lies above that of TiO_2 which facilitate effective charge separation by reducing the possibility for photo generated electron-hole pair recombination.[14] CdS sensitised TiO_2 have also been exploited as photocatalyst for hydrogen production from water[15,16] as photoelectrode in dye sensitized solar cells to improve the efficiency of the cells[17,18] and as highly efficient charge carriers in heterogeneous photocatalysis.[19,20]

Photocatalytic activity of CdS sensitized TiO_2 nanoparticles have been reported recently by Shuli Bai *et al*. and Li *et al*. for the degradation of Rhodamine B and for the oxidation of NO gas respectively.[21,22] They found that the surface incorporation of CdS crystals had a marked effect on the photoactivity of TiO_2. The selective oxidation of alcohol to aldehyde in presence of CdS nanorods on the surface of TiO_2 was reported by Liu *et al.*[23] Very recently visible light active CdS decorated TiO_2 photocatalysts have been developed for the oxidative removal of organic dyes from aqueous textile effluents.[24,25] Xu *et al.*[26] have developed a simple design for encapsulating CdS nano spheres into a thin TiO_2 shell inorder to improve the charge transport properties and to improve the selective redox reactions under visible light. In this work remarkable increase in photoactivity was obtained due to effective interfacial hybridization between CdS and TiO_2. As compared to previous reports, the present work embodies our attempt to fabricate CdS hybridized TiO_2 photocatalysts, in which special

attention was given to optimize the minimum concentration of CdS required to sensitize TiO_2 matrix. Hydrothermal method was adopted to fabricate the different compositions of TiO_2-CdS nanohybrid systems (0%, 1%, 5% and 10%), out of which 10 % CdS incorporation was found to be the optimum concentration for the oxidative removal of organic pollutant. Toxic and mutagenic methyl orange dye[27] was selected as the reference system to study the photocatalytic properties of the CdS sensitized TiO_2 nano hybrid system. Hopefully the work would provide an insight for the further development of TiO_2 based nano hetero systems for energy and environmental applications.

7. 2. Results and Discussion

7. 2. 1. X-ray Diffraction

X-ray diffraction patterns of pure TiO_2 and CdS along with different composition of TiO_2-CdS are shown in **Figure 7. 1**. XRD peaks in **Figure 7. 1(a)** at 2θ values 25.4 ^{o}, 38.1 ^{o}, 48.1 ^{o}, 54.6 ^{o} and 62.9 ^{o} corresponds to the diffraction from (101), (103), (200), (105) and (211) crystal planes of anatase TiO_2 (JCPDS No. 21-1272). Diffraction peaks in **Figure 7. 1(e)** at 26.5 ^{o}, 43.9 ^{o} and 52.0 ^{o} could be indexed to (111), (220) and (311) phases of cubic crystalline CdS (JCPDS No. 10-0454). It was observed that the characteristic peaks of anatase TiO_2 and CdS (marked as *) are preserved at TiO_2-CdS10 (**Figure 7. 1d**) composite which indicates an effective hybridization between the two phases for this particular composition.

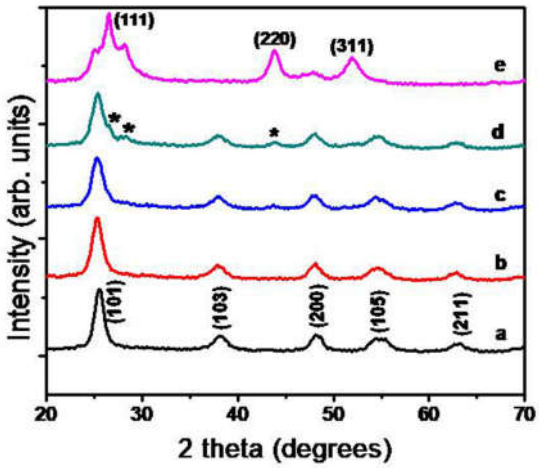

Figure 7. 1. XRD patterns of (a) TiO_2 (b) TiO_2-CdS1 (c) TiO_2-CdS5 (d) TiO_2-CdS10 and (d) CdS.

7. 2. 2. Transmission electron microscopy (TEM)

TEM was used to analyze the microstructure and the particle size of different photo catalysts. TEM images in **Figure 7. 2(a)** displays the homogeneous dispersion of CdS nano crystals in TiO_2 matrix with an average particle size of 10-15 nm. The crystallite size calculated from the XRD data by using Debye Scherrer method was found to be 8-10 nm. HRTEM image (**Figure 7. 2b**) of the TiO_2-CdS10 composite displays two types of lattice planes with interplanar distance 0.34 nm (101 plane of TiO_2) and 0.32 nm (111 plane of CdS) unequivocally confirm excellent hybridization established between TiO_2 and CdS nanoparticles in TiO_2-CdS10 heterostructure photocatalyst**.**

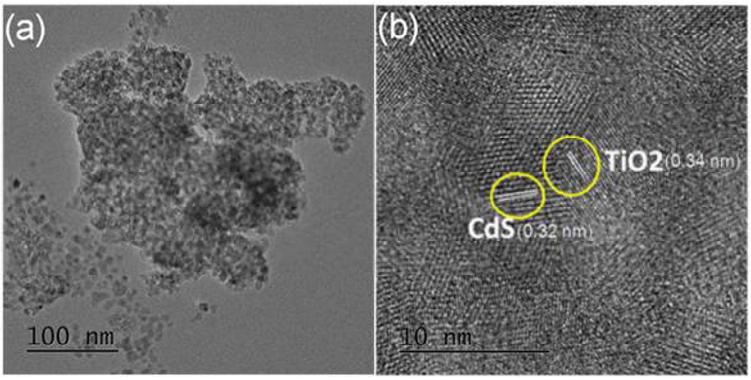

Figure 7. 2. TEM image of (a) TiO_2-CdS10 and (b) HRTEM image of TiO_2-CdS10.

7. 2. 3. Raman Spectroscopy

Figure. 7. 3 shows the room temperature Raman spectra of TiO_2 and TiO_2-CdS nanocrystals along with the spectra of CdS. According to factor group analysis tetragonal anatase TiO_2 exhibits four Raman active vibration modes $A_{1g}+B_{1g}+B_{2g}+E_g$. The peak at 144 cm^{-1} corresponds to E_g mode and the peak at 396 cm^{-1} is due to B_{1g} vibration modes of anatase TiO_2.[28] The peak at 516 cm^{-1} is resulted from the B_{1g} and A_{1g} modes of anatase TiO_2 and the Raman band at 639 cm^{-1} can be attributed to E_g vibration of anatase phase.[29] Raman spectra of CdS is dominated by well-defined broad peaks at 296, 593 and 890 cm^{-1} which are ascribed to the first order longitudinal optic (LO) vibration mode (E1), second order LO (E2) and third order LO of CdS unit cell respectively.[30,31] Relatively broad band for CdS is due to the reduced crystallinity of CdS phase as evidenced from the XRD studies. Raman spectra of composite TiO_2-CdS10 is dominant with its

component phases, which shows excellent dispersion of CdS over TiO_2 matrix.

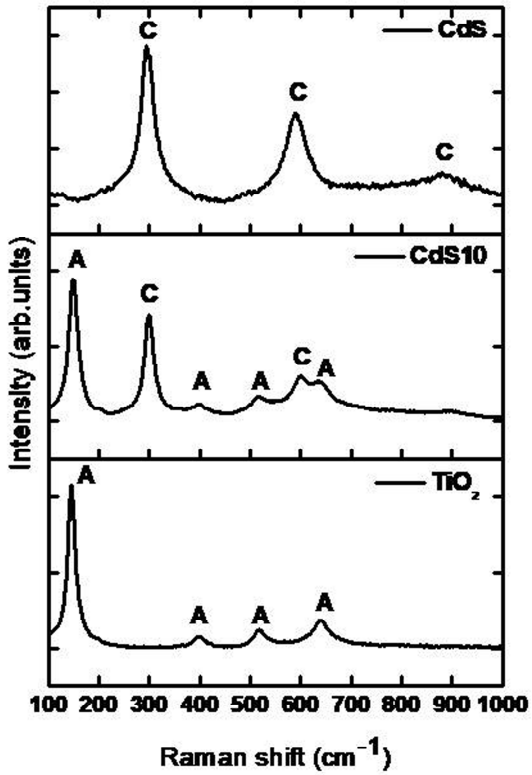

Figure 7. 3. Raman spectra of TiO_2, TiO_2-CdS10 and CdS

7. 2. 4. X-ray photoelectron spectroscopy (XPS)

Surface probe technique was used to determine the surface chemical state and composition of the materials. As depicted in the survey XPS spectrum in **Figure 7. 4(a)**, the elemental composition on the surface of the composite, TiO_2-CdS10 was found to be composed of Ti, Cd, S and O elements. Peaks at 464.05 and 458.35 eV in **Figure 7. 4(b)** is the

characteristic peaks corresponding to $Ti2p_{3/2}$ and $Ti2p_{1/2}$ binding energies. The difference between the two peaks was found to be 5.7 eV which is a characteristic of the abundance of Ti^{4+} on the surface of the catalyst.[32] XPS spectrum in **Figure 7. 4(c)** at 529.6 eV is obtained from O1s binding energy and the shoulder peak of O1s spectra is due to the contribution from CO_3^{2-} species (530-531 eV) present in the low temperature processed samples.[33] Two sharp peaks observed in **Figure 7. 4(d)** at binding energies 405 and 412 eV can be assigned to $Cd3d_{3/2}$ and $Cd3d_{5/2}$ respectively. Moreover a spin orbit separation of 6.7 between these two peaks confirms the presence of Cd^{2+} on the surface of the material.[24] The doublet peak in **Figure 7. 4(e)** at 160.5 and 161.9 eV indicates the presence of S^{2-} ions on the surface of the heterostructure, which corresponds to $S2p_{1/2}$ and $S2p_{3/2}$ states.[24] The shoulder peak in S2p at 162-163 eV can be attributed to the contribution from R-S-H groups at the surface of the TiO_2-CdS nanocomposite sample which is originated from the partial decomposition of organic groups in the catalyst.[34,35] XPS spectral data further confirms the formation of heterostructure between TiO_2 and CdS.

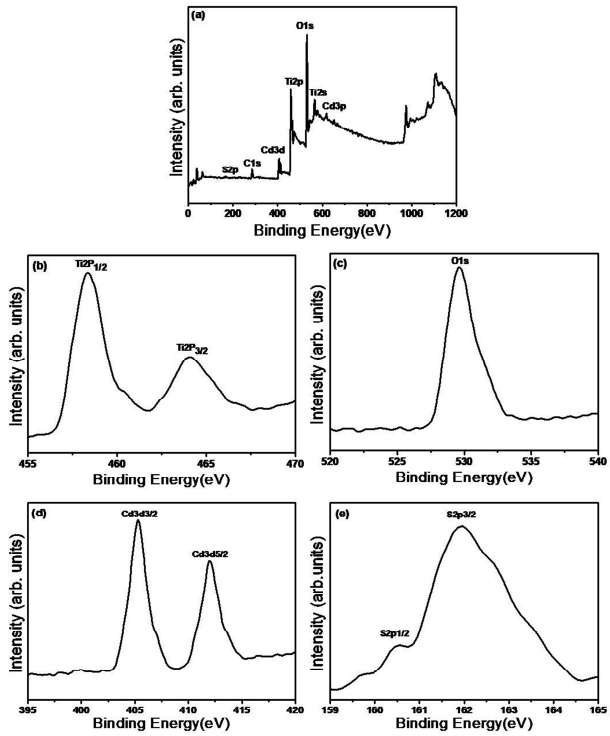

Figure 7. 4. XPS spectra of TiO_2-CdS10 nanocomposites: (a) The whole survey spectrum; (b) Ti2p XPS spectrum; (c) O1s XPS spectrum; (d) Cd3d XPS spectrum and (e) S2p XPS spectrum.

7. 2. 5. BET Surface area

Photocatalytic activity of a material is greatly influenced by the change in surface property of the material. BET-N_2 gas adsorption studies were normally used for determining the surface area, and pore size distribution of the solid materials. The N_2 adsorption-desorption isotherms in **Figure 7. 5** and BJH pore-size distribution curves of different catalyst materials were given as inset of **Figure 7. 5**. BET surface area, pore sizes and pore volumes were summarized in **Table 7. 1**. Adsorption isotherm indicates a type IV physisorption curve with

H3 hysteresis loop, which is the characteristic feature of a mesoporous material with pore size between 2-50 nm.[36] It was observed from **Figure 7. 5** that compared to other samples, capillary condensation or hysteresis closure was observed at low pressure region for CdS10 and CdS. This difference in adsorption isotherms may be due to wide range of pore size distribution in these samples as evident from inset **Figure 7. 5**. In addition to crystallinity and rate of electron-hole pair recombination, surface area of the catalyst play a key role in photocatalysis. It is clearly observable from **Table 7. 1** that the surface area of TiO_2-CdS10 composite is greater than that of other catalysts. The significant increase in photoactivity for TiO_2-CdS10 was attributed to its high surface area which can provide more reactive sites during photodegradation.

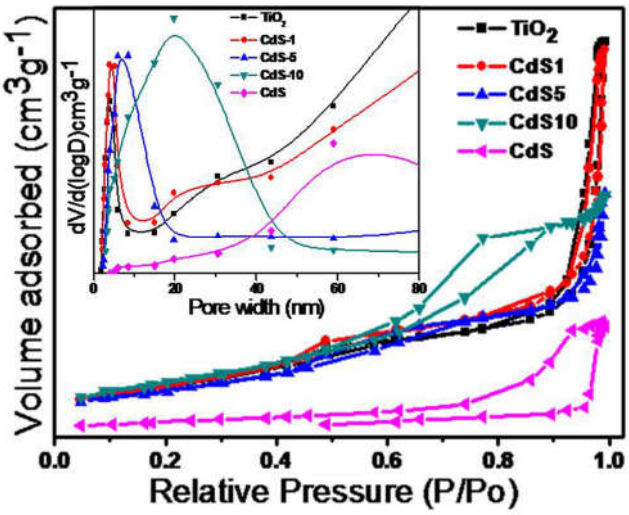

Figure 7. 5. BET N_2 adsorption isotherm of various catalysts and the inset shows their pore size distribution curves.

Table 7. 1. BET surface area and pore size measurements.

Catalyst	BET surface area/m^2g^{-1}	Pore volume/cm^3g^{-1}	BJH desorption pore size/nm
TiO_2	134	0.48	12.6
TiO_2-CdS1	140	0.47	11.2
TiO_2-CdS5	126	0.29	8.2
TiO_2-CdS10	153	0.31	6.8
CdS	39	0.14	11.4

7. 2. 6. UV-Visible Absorption Spectra and Tauc Plot

UV-visible absorption spectra and the Tauc plot of all samples were given in **Figure 7. 6**. Two distinct absorption edges possessed by the composite samples strongly support the sensitization of TiO_2 by the chromaphoric CdS semiconductor. It can be seen from **Figure 7. 6(a)** that the light absorption capability of bare TiO_2 is limited to ultraviolet region due to its wide band gap (3.24 eV) and the band edge is around 400 nm. While introducing the CdS phase in TiO_2 the light absorption shifted to visible light due to the influence of narrow band gap CdS which act as a sensitizer to harvest visible region of the spectra. The light absorption of the composites; CdS1, CdS5, CdS10 were shifted to 405, 565 and 574 nm which corresponds to a band gap of 3.20, 2.15 and 2.12 eV respectively (**Figure 7. 6b**).

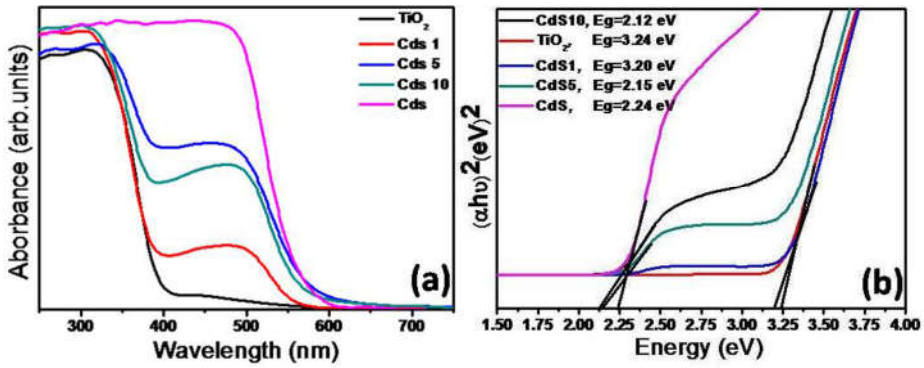

Figure 7. 6. (a) UV-visible absorption spectra and (b) Tauc plot of the catalyst samples.

7. 2. 7. Photoluminescence spectra

Photoluminescence (PL) spectroscopy is a powerful technique to determine the fate of photo excited charge carriers in semiconductors.[37] To correlate the photocatalytic efficiency with the charge separation efficiency of the catalysts, fluorescence quenching of the materials where analyzed at an excitation wavelength of 280 nm (**Figure. 7. 7**). The obtained peak at 573 nm for all the samples arises due to the recombination of excited charge carriers at the band edge.[38] Compared to other samples PL intensity is weaker for TiO_2-CdS10, this lower intensity is ascribed to the lower rate of electron-hole recombination and effective separation of charge carriers in this particular system.[39] Photocatalytic study showed that among the studied samples, TiO_2-CdS10 exhibit greater photocatalytic efficiency and the results are in agreement with the fluorescence quenching data. Even though the PL intensity of bare TiO_2 is very low, the photocatalytic efficiency was

found to lesser than TiO_2-CdS10 because of the reduced surface area possessed by bare TiO_2 catalyst as described in Table 7. 1.

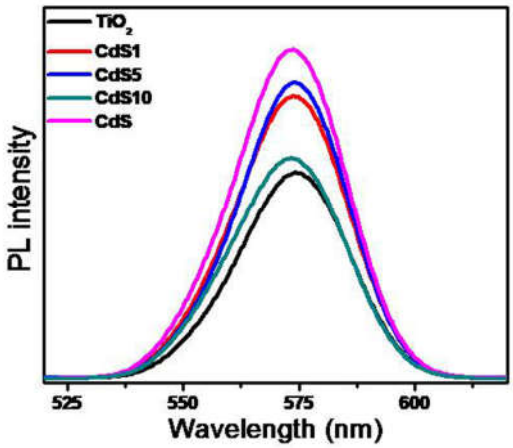

Figure. 7. 7. Photoluminescence (PL) Spectra of the various catalysts.

7. 2. 8 Photocatalysis

The degradation curve, C/Co *Vs* time of MO degradation in presence of various catalysts is shown in **Figure 7. 8(a)**. TiO_2-CdS10 nano hybrid systems have exhibited an excellent catalytic activity among the various catalysts and almost complete degradation of the dye solution was occurred in 40 minutes of sunlight illumination. The photocatalytic results are in agreement with fluorescence spectral studies. PL results show a decrease in intensity for the particular hybrid material TiO_2-CdS10 which indicates an effective charge transfer between the two phases.

Dye degradation kinetics obeys Langmuir-Hinshelwood first order equation *ln* (Co/C)=kt, where Co and C are the concentrations of the dye solutions before and after exposure to sunlight. Slope of the straight line obtained by plotting *ln* (Co/C) *Vs* time t gives the value of k (min^{-1}). Calculated rate constant of the disintegration reaction for different catalytic reactions are arranged as bar diagram in **Figure 7. 8(b)**. The rate of the reaction is dramatically enhanced by incorporating 10 wt% CdS nano crystals in anatase TiO_2 (TiO_2-CdS10). Highest rate constant of $2.8x10^{-2}$ min^{-1}, which is about 3.5 times that of bare TiO_2 unequivocally supports the superior catalytic performance of 10 wt % CdS sensitized TiO_2 nano heterostructure photocatalyst.

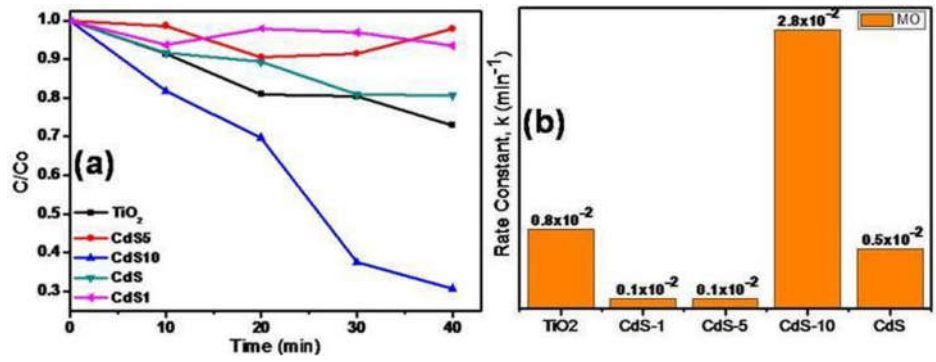

Figure 7. 8. (a) Photodegradation curve and (b) First order rate constant (k, min^{-1}) value of methyl orange degradation in presence of TiO_2, TiO_2-CdS1, TiO_2-CdS5, TiO_2-CdS10 and CdS.

7. 2. 9. Mechanism for MO degradation in presence of CdS sensitized TiO_2

Based on the above results and discussions, a plausible mechanism was proposed for the sunlight driven photo catalytic degradation of MO dye over TiO_2-CdS nano heterostructure photo catalyst. As depicted in **scheme 7 .1**, on illumination with solar radiation, electrons were ejected from the VB to CB of CdS due to its narrow energy gap of around 2.2 eV. Since the CB of CdS is about 0.5 eV more positive than the conduction band (CB) of TiO_2, photogenerated electrons are transferred from the CB of CdS to that of TiO_2 whereas the valence band (VB) of CdS acts as hole centers.[34] This charge delocalization remarkably reduces the rate of electron-hole recombination and thereby facilitates oxidation-reduction process. The CB electrons are trapped by O_2 to form reactive oxygen species ($O2^{-\cdot}$) and H_2O_2. These intermediates react together to form hydroxyl radical ($OH^{\cdot}$) which is a powerful oxidizing agent capable of degrading dissolved organic pollutants.[40-44] The possible reactions for the photocatalytic MO degradation are given as follows:

$TiO_2/CdS + h\gamma\ (visible) \rightarrow e^-_{CB} + h^+_{VB}$

$e^-_{CB} + O_2 \rightarrow O_2^{\cdot -}$

$h^+_{VB} + OH^- \rightarrow OH^{\cdot}$

$O_2^{\cdot -} + 2H^+ + 2e^- \rightarrow O_2 + H_2O_2$

$O_2^{\cdot -} + H_2O \rightarrow H_2O^{\cdot} + OH^-$

$H_2O^{\cdot} + H_2O \rightarrow H_2O_2 + OH^{\cdot}$

$H_2O_2 \rightarrow 2OH^{\cdot}$

$OH^{\cdot} + MO\ dye \rightarrow CO_2 + H_2O$

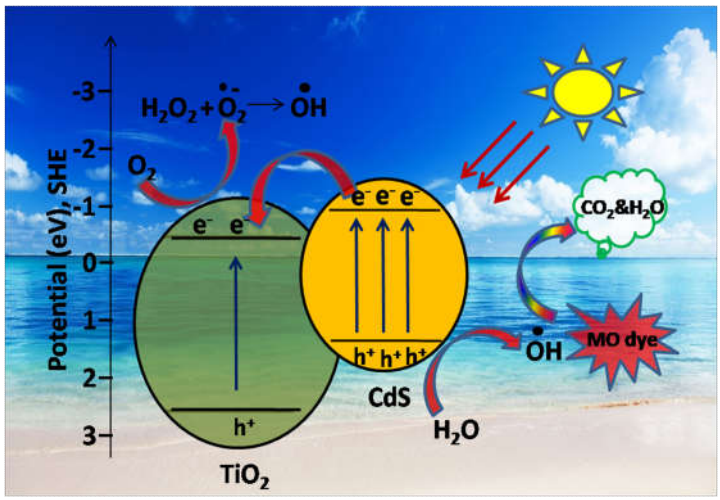

Scheme 7. 1. Schematic illustration of the mechanism of sunlight driven photocatalysis.

7. 3. Conclusions

In summary, nano crystalline TiO_2-CdS nano-hybrid systems were synthesized by hydrothermal method and the visible light absorption capability of the bare TiO_2 nanoparticles were found to be dramatically improved by CdS incorporation. XRD, Raman studies and TEM analysis strongly supported the coupling between two heterogeneous phases. Among the synthesized catalysts, TiO_2 assembled with 10 wt% CdS (TiO_2-CdS10) shows excellent sunlight driven photocatalytic activity towards the degradation of methyl orange, with a degradation rate of 2.8×10^{-2} min^{-1}, which is about 3.5 times faster than that of bare TiO_2. From the fluorescence quenching studies and BET results, it can be concluded that the effective charge separation efficiency, high surface area and the synergetic action of all these factors are responsible for the remarkable enhancement in the photocatalytic

activity of TiO_2-CdS10 photocatalyst. The present work may be a good reference for the development of sunlight harvesting nano heterostructured photocatalytic materials for energy and environmental applications.

References

1. K. Hashimoto, H. Irie, A. Fujishima, *Jpn. J. Appl. Phys*., 2005, 44, 8269.
2. J. Schneider, M. Matsuoka, M. Takeuchi, J. Zhang, Y. Horiuchi, M. Anpo, D. W. Bahnemann, *Chem. Rev*., 2014, 114, 9919.
3. O. Amiri, N. Mir, F. Ansari, M. S. Niasari, *Electrochim. Acta*, 2017, 252, 315.
4. P. Periyat, S. C. Pillai, D. E. Mc Cormack, J. Colreavy, S. J. Hinder, *J. Phys. Chem. C*, 2008, 112, 7644.
5. S. G. Kumar, L. G. Devi, *J. Phys. Chem*., 2011, A115, 13211.
6. N. Zhang, S. Liu, Y. J. Xu, *Nanoscale*, 2012, 4, 2227.
7. X. Jie, N. Bao, B. Gong, S. Zhou, *Nano-Structures & Nano-Objects*, 2017, 12, 98.
8. X. Chen, C. Burda, *J. Am. Chem. Soc*., 2008, 130, 5018.
9. H. Choi, P. K. Santra, P. V. Kamat, *ACS Nano*, 2012, 6, 5718.
10. Y. Zhao, Q. Sun, J. Luo, H. Chen, W. Cai, X. Su, *Nano-Structures & Nano-Objects*, 2018, 13, 93.
11. H. Wang, L. Zhang, Z. Chen, J. Hu, S. Li, Z. Wang, J. Liu, X. Wang, *Chem. Soc. Rev*., 2014, 43, 5234.
12. G. S. Li, D. Q. Zhang, J. C. Yu, *Environ. Sci. Technol*., 2009, 43, 7018.
13. R. G. Solanki, P. Rajaram, *Nano-Structures & Nano-Objects*, 2017, 12, 157.
14. K. Das, S. K. De, *J. Phys. Chem. C*, 2009, 113, 3494.
15. J. Fang, L. Xu, Z. Zhang, Y. Yuan, S. Cao, Z. Wang, L. Yin, Y. Liao, C. Xue, *ACS Appl. Mater. Interfaces*, 2013, 5, 8088.
16. J. S. Jang, H. G. Kim, U. A. Joshi, J. W. Jang, J. S. Lee, *Int. J. Hydrogen Energy*, 2008, 33, 5975.
17. W. T. Sun , Y. Yu , H. Y. Pan , X. F. Gao , Q. Chen, L. M. Peng, *J. Am. Chem. Soc*., 2008, 130, 1124.

18. M. Shalom, S. Dor, S. Rühle, L. Grinis, A. Zaban, *J. Phys. Chem. C*, 2009, 113, 3895.

19. J. Luo, L. Ma, T. He, C. F. Ng, S. Wang, H. Sun, H. J. Fan, *J. Phys. Chem. C*, 2012, 116, 11956.

20. P. Zhou, Z. Le , Y. Xie , J. Fang, J. Xu, *J. Alloys Compd*., 2017, 692, 170.

21. S. Bai, H. Li, Y. Guan, S. Jiang, *Appl. Surf. Sci*., 2011, 257, 6406.

22. G. S. Li, D. Q. Zhang, J. C. Yu, *Environ. Sci. Technol*., 2009, 43, 7079.

23. S. Liu, N. Zhang, Z. R. Tang, Y. J. Xu, *ACS Appl. Mater. Interfaces*, 2012, 4, 6378.

24. R. Dang, X. J. Ma, *Mater. Sci. Mater. Electron*., 2017, 28, 8818.

25. Z. Tian, N. Yu, Y. Cheng, Z. Wang, Z. Chen, L. Zhang, *Mater. Lett*., 2017, 194, 172.

26. Z. Chen, Y. J. Xu, *ACS Appl. Mater. Interfaces*, 2013, 5, 13353.

27. K. T. Chung, C. E. Cerniglia, *Mutat. Res*., 1992, 277, 201.

28. R. Fagan, D. W. Synnott, D. E. McCormack, S. C Pillai, *Appl. Surf. Sci*., 2016, 371, 447.

29. T. Ohsaka, F. Izumi, Y. Fujiki, J. *Raman. Spectrosc*., 1978, 7, 321.

30. S. S. Mali, S. K Desai, D. S. Dalavi, C. A. Betty, P. N. Bhosalea and P. S. Patil, *Photochem. Photobiol. Sci*., 2011, 10, 1652.

31. J. C. Tristao, F. Magalhaes, P. Corio, M. Terezinha, C. J. Sansiviero, *J. Photochem. Photobiol. A*, 2006, 181, 152.

32. Y. C. Zhang, J. Li, H. Y. Xu, *Appl. Catal. B-Environ*., 2012, 123, 18.

33. F. H. Scholes, A. E. Hughes, S. G. Hardin, P. Lynch, P. R. Miller, *Chem. Mater*., 2007, 19, 2321.

34. C. Xue, T. Wang, G. Yang, B. Yang, S. Ding, *J. Mater. Chem. A*, 2014, 2, 7674.

35. M. Fantauzzi, B. Elsener, D. Atzei, A. Rigoldi, A. Rossi, *RSC Adv*., 2015, 5, 75953.

36. K. S. W. Sing, D. H. Everett, R. A. W. Haul, L. Moscou, R. A. Pierotti. J. Rouquerol, T. Siemieniewska, *Pure Appl. Chem*., 1985, 57, 603.

37. B. Lin, H. An, X. Yan, T. Zhang, J. Wei, G. Yang, *Appl. Catal. B-Environ*., 2017, 210, 173.

38. J. Shi, J. Chen, Z. Feng, T. Chen, Y. Lian, X. Wang, C. Li, *J. Phys. Chem. C*, 2007, 111, 6939.

39. J. Liqiang, Q. Yichun, W. Baiqi, L. Shudan, J. Baojiang, Y. Libin, F. Wei, F. Honggang, S. Jiazhong, *Sol. Energy Mater. C*, 2006, 90, 1773.

40. N. Kalithasan, H. C. Bajaj, R. J. Tayade, *Sol. Energy*, 2017, 148, 87.

41. P. Suyana, K. R. Sneha, B. N. Nair, V. Karunakaran, A. P. Mohamed, K. G. K. Warrier, U. S. Hareesh, *RSC Adv*., 2016, 6, 17800.

42. M. Ghanbari, F. Ansari, M. S. Niasari, *Inorganica Chim. Acta*, 2017, 455, 88.

43. H. Huang, X. Li, J. Wang, F. Dong, P. K. Chu, T. Zhang, Y. Zhang, *ACS Catalysis*, 2015, 5, 4094.

44. L. Yuan, B. Weng, J. C. Colmenares, Y. Sun, Y. J. Xu, *Small*, 2017, 13, 48.

Chapter Eight

Overall Conclusions and Future Outlook

Contents

8. 1. Overall Conclusions

The population explosion and industrial revolution have a direct consequence on energy crisis and environmental pollution. A clean energy and a green environment are inevitable for the sustainable development of the society.[1] Keeping this aspect, the objectives of the present thesis work have divided in to energy objectives and environmental objectives. The aim of the present research was to develop nano semiconductor hybrid materials that can be employed in energy applications as supercapacitor electrodes and/or environmental remediation applications as photocatalyst and adsorbent materials. Graphitic carbon nitride (g-C_3N_4), TiO_2, Fe_2O_3 based nano-hetero structures were selected for the investigations. Chapter 1 of the thesis deals with the introduction and literature reviews. The experimental methods and the characterization techniques adopted were discussed in Chapter 2. The major findings of the research works were included in Chapter 3 to Chapter 7.

In Chapter 3, attempts were made to improve the electrochemical properties of 2D graphitic carbon nitride (g-C_3N_4) by suitable addition of 1D TiO_2 nanotubes to develop g-C_3N_4/TiO_2 nano hybrid materials. The different composition of the materials were prepared by keeping g-C_3N_4/ TiO_2 ratio as 1:0, 1:1, 1:2, 1:4. The composite sample with 1:4 compositions has shown excellent electrochemical properties than the other samples with a specific capacitance of 79.62 F g^{-1} which is much higher than the specific capacitance of bare g-C_3N_4 electrode (50.22 F g^{-1}).

In Chapter 4, pseudocapaitive metal oxide nanoparticles(MnO_2 and SnO_2) were introduced in to the 2D layers of g-C_3N_4 and fabricated heterostructures of g-C_3N_4/MnO_2 and g-C_3N_4/SnO_2. The materials were employed as electrodes in symmetric supercapacitor devices and the properties were compared with bare g-C_3N_4. g-C_3N_4/MnO_2 electrode exhibited specific capacitance (Csp) of 174 Fg^{-1} which is higher than the Csp of g-C_3N_4/SnO_2 (64 Fg^{-1}) and g-C_3N_4 (50 Fg^{-1}). At a constant power density of 1 $kWkg^{-1}$ the symmetric supercapacitors based on g-C_3N_4, g-C_3N_4/SnO_2, and g-C_3N_4/MnO_2 electrodes exhibited energy densities of 6.9, 8.8 and 24.1 $Whkg^{-1}$ respectively.

In Chapter 5, pseudocapacitive Co_3O_4 and CuO nanoparticles were anchored on the surface of g-C_3N_4 by direct precipitation method. g-C_3N_4/Co_3O_4 and g-C_3N_4/CuO nano hybrid materials were used as a cost effective electrodes in symmetric supercapacitor devices. The electrochemical performance of g-C_3N_4 have shown significant enhancement by coupling with Co_3O_4 and CuO with a specific capacitance of 201 Fg^{-1} and 95 Fg^{-1} for g-C_3N_4/Co_3O_4 and g-C_3N_4/CuO

composite materials respectively. The enhancement in electrochemical properties in composite sample can be attributed to the presence of pseudocapacitive phases. The g-C_3N_4/Co_3O_4 exhibited a cyclic stability of 97 % even after 6000 cycles with an energy density of 27.9 $Whkg^{-1}$.

In Chapter 6, Fe_2O_3@carbon nano-hetero structures were prepared from discarded razor blades and glucose solution *via* hydrothermal method by considering the concept of 'regenerative economy'. The material was used as electrode in symmetric supercapacitor device and also as an adsorbent for the removal of oil-spills from water. At a constant current density of 1 Ag^{-1}; the Fe_2O_3@carbon electrode exhibited a highest specific capacitance of 285.6 Fg^{-1} which is almost two-fold the specific capacitance of the as-synthesized Fe_2O_3 sample (122.7 Fg^{-1}). At a constant power density of 1 $kWkg^{-1}$, Fe_2O_3 and Fe_2O_3@carbon samples have the energy density values of 22.52 $Whkg^{-1}$and 37.88 $Whkg^{-1}$, respectively.

In Chapter 7, attempts were made to enhance the sunlight absorption capability of TiO_2 by fabricating a nano hetero structure with low band gap cadmium sulphide (CdS). Different weight percentage (0, 1, 2 and 10) of CdS was introduced into TiO_2 matrix *via* hydrothermal method. The light absorption of TiO_2 get shifted from UV region to visible region of the solar spectrum due to the presence of CdS nanoparticles. The photocatalytic activity of TiO_2 loaded with 10 weight percentage of CdS (TiO_2-CdS10) have shown excellent photocatalytic activity for the degradation of methyl orange dye. The degradation rate of the active material was found to be $2.8x10^{-2}$ min^{-1} which is about 3.5 times

faster than the rate of bare TiO_2 catalyst. The photoactivity results are in good agreement with BET and PL spectral studies.

8. 2. Future Outlook

The innovations in the area of new advanced materials for renewable energy conversion, storage and also for environmental remediation is moving forward at a faster rate.[2] A massive research in newer and newer functional materials is needed for the sustainable development of the society with a very low carbon footprint.[3] The present research work may be a reference for the material scientists working in the area of functional materials for energy storage and environmental cleaning applications. The current research work may lead the way for the evolution of the following areas of research.

1. Development of composite materials based on g-C_3N_4 and MoS_2 (conducting and semiconducting) for energy storage and H_2 evolution applications.

2. Enhancing the conductivity of g-C_3N_4 by incorporating activated carbon (derived from natural source) for supercapacitor applications.

3. Fabrication of new electrode materials based on carbon allotropes and micro fibrillated cellulose (MFC) for energy storage applications.

References

1. M. D. Stoller, R. S. Ruoff, *Energy. Envir. Sci*., 2010, 3, 1294.

2. Press Information Bureau, *Govt. of India, Ministry of new and renewable energy*, 2017.

3. B. Babu, S. G. Ullattil, R. Prasannachandran, J. Kavil, P. Periyat, M. M. Shaijumon, *ACS Sustain. Chem. Eng*., 2018, 6, 5401.

Publications by the Author

Journal Articles

Jithesh Kavil, P. M. Anjana, P. Periyat, R. B. Rakhi, TiO_2 nanotubes dispersed graphitic carbon nitride nanosheets as efficient electrode materials for supercapacitors, J. Mater. Science Mater. Electron., 2018, 29, 16598.

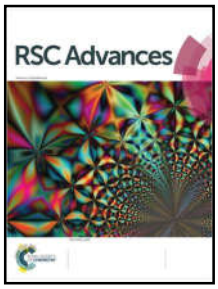

Jithesh Kavil, P. M. Anjana, Deepak Joshy, Ameya Babu, Govind Raj, P. Periyat, R. B. Rakhi, g-C_3N_4/CuO and g-C_3N_4/Co_3O_4 nanohybrid structures as efficient electrode materials in symmetric supercapacitors (RSC Adv. 2019, 9, 38430).

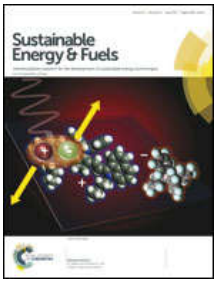

Jithesh Kavil, P. M. Anjana, P. Periyat, R. B. Rakhi, One-pot synthesis of g-C_3N_4/MnO_2, g-C_3N_4/SnO_2 hybrid nanocomposites for supercapacitor applications, Sustainable Energy & Fuels, 2018, 10, 2244.

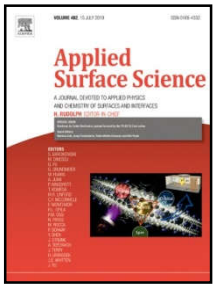

Jithesh Kavil, P. M. Anjana, C. P. Roshni, P. Periyat, K. Govind Raj, R.B. Rakhi, Multifunctional nanohybrid material from discarded razor blades as cost-effective supercapacitor electrodes and oil-spill cleaners, Appl. Surf. Sci., 2019, 487, 109.

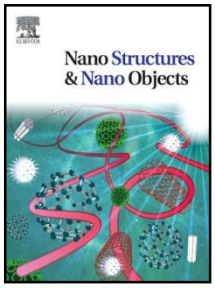

Jithesh Kavil, A. Alshahrie, P. Periyat, CdS sensitized TiO_2 nano heterostructures as sunlight driven photocatalyst, Nano-Structures & Nano-Objects, 2018, 16, 24.

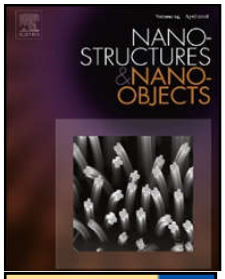

Jithesh Kavil, P. Shabeeba, M. S. Thayyil, P. Periyat, Development of 2D nano heterostructures based on g-C_3N_4 and flower shaped MoS_2 as electrode in symmetric supercapacitor device, Nano-Structures & Nano-Objects, 2019, 18, 100317.

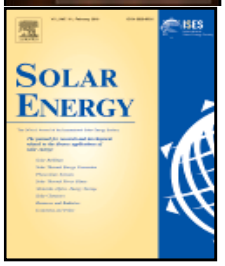

Jithesh Kavil, S. G. Ullattil, A. Alshahrie, P. Periyat, Polyaniline as photocatalytic promoter in black anatase TiO_2, Solar Energy, 2017, 158, 792.

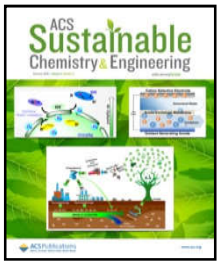

B. Babu, S. G. Ullattil, R. Prasannachandran, **Jithesh Kavil**, P. Periyat, M. M. Shaijumon, Ti^{3+} induced brown TiO_2 nanotubes for high performance sodium-ion hybrid capacitors, ACS Sustain. Chem. Eng., 2018, 6, 5401.

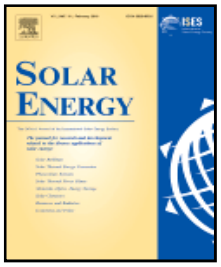

S. G. Ullattil, A. V. Thelappurath, S. N. Tadka, **Jithesh Kavil**, B. K. Vijayan, P. Periyat, A Sol-solvothermal processed 'Black TiO_2'as photoanode material in dye sensitized solar cells, Solar Energy, 2017, 155, 490.

Conference/Seminars

1. National Seminar on Recent Advances in Chemistry (UGC), Sunlight driven Photoactivity of ZnO Nanoparticles, KMM Govt. College, Kannur-2015.
2. National Seminar on Advanced Topics in Chemistry (UGC), Photocatalytic activity of S, N doped TiO_2, Sree Narayana College, Nattika, Trissur-2015.
3. International Conference on Advances in Biological, Chemical and Physical Sciences (ABCPS-2017), A dual function platform using polyaniline as photo-corrosion inhibitor and photocatalyst promoter in black anatase TiO_2, Anna University, Thiruchirappalli-2017.
4. IISc, INUP Hands on Training Workshop (10 days) on "Nanofabrication Technologies", Centre for Nano Science and Engineering, IISc, Bangalore-2017.
5. National Seminar on Frontiers in Chemical Sciences (KSCSTE), University of Calicut-2018.
6. International Conference on Supercapacitors, Energy Storage & Applications (ICSEA), Centre for materials for Electronics Technology (C-MET), Thrissur-2019.
7. International Conference on Nanoscience and Nanotechnology (ICONN 2019), Multifunctional Nanohybrid Material from Discarded Blades as Cost-Effective Supercapacitor Electrodes, SRM Institute of Science and Technology, Chennai-2019.

Journal of Materials Science: Materials in Electronics
https://doi.org/10.1007/s10854-018-9753-1

Titania nanotubes dispersed graphitic carbon nitride nanosheets as efficient electrode materials for supercapacitors

Jithesh Kavil[1] · P. M. Anjana[2] · Pradeepan Periyat[1] · R. B. Rakhi[2]

Received: 2 February 2018 / Accepted: 25 July 2018

Abstract
Herein, we report the synthesis of a hybrid nanocomposite containing one dimensional (1D) TiO_2 nanotube supported over a two dimensional (2D) network of conducting graphitic carbon nitride (g-C_3N_4) nanosheets by a facile hydrothermal strategy. Symmetric supercapacitors based on the hybrid composite electrodes were fabricated and their electrochemical energy storage performances were evaluated and the results were compared with individual component based supercapacitors. The symmetric supercapacitor based on the composite with 1:4 weight ratios of TiO_2 and g-C_3N_4 exhibited a remarkable increase in the specific capacitance in comparison with the individual components. The improvement in electrochemical behavior of the composite sample was attributed to the increase in surface area of the composite due to the spacer effect of titania nanotubes in the 2D g-C_3N_4 nanosheets.

1 Introduction

In the event of the glaring problem of depletion of conventional non renewable energy sources staring at us in the eye, not to mention the huge amounts of pollution caused by such sources, the question of global energy demand for a clean and abundant energy source needs to be solved and requires an imminent solution. With solar energy being at present the best promising alternative, the problem associated with this technology that of storing the energy harvested requires urgent and detailed attention. It is due to this, energy storage devices such as supercapacitors hold the present day researcher's interest. Supercapacitors store energy by incorporating high surface area electrodes and thinner dielectrics rather than chemicals, unlike conventional batteries, and has been considered as an alternative power source because of their durability and ability to charge and discharge within a short period of time [1–3]. Transition metal oxide based pseudocapacitors which store energy via faradaic mechanism are having superior electrochemical capacitance as compared to the carbon based electrical double layer capacitor, as in the latter, the capacitance purely depends on the limited accumulation of charge at electrode–electrolyte interface [4–9]. So far reported successful candidates among the various metal oxides used in supercapacitors, like the ruthenium oxides, has the disadvantage of being expensive and are also toxic [10]. Among the low-cost transition metal oxides, TiO_2 nanotubes (TNT) has shown promise in electrochemical applications recently [5]. TiO_2 holds particular interest due to its environmentally benign chemical nature, stability and low cost [11–14]. Ramadoss et al. reported the use of TiO_2 nanorod arrays prepared on the fluorine doped tin oxide substrates using a facile hydrothermal method and the nanostructures were employed as the electrode materials for supercapacitors with a specific capacitance of f 85 μF cm^{-2} at a scan rate of 5 Mv s^{-1} in the three electrode configuration [15]. Zhou et al. reported the fabrication of supercapacitor electrode using three-dimensional (3D) nanoporous hydrogenated TiO_2 network film on titanium substrate by a controllable method, exhibiting a specific capacitance of 1.07 mF cm^{-2} at a scanrate of 50 mV s^{-1} in the three electrode configuration [16]. Unfortunately, specific capacitance of TiO_2 nanotube supercapacitors are very small and it drops continuously on increasing the scan rate due to its low electrochemical activity and poor conductivity [17–19]. In order to overcome these limitations, several attempts have

✉ Pradeepan Periyat
pperiyat@uoc.ac.in

✉ R. B. Rakhi
rakhiraghavanbaby@niist.res.in

[1] Department of Chemistry, University of Calicut, Malappuram, Kerala 673635, India

[2] Chemical Sciences and Technology Division, CSIR- National Institute of Interdisciplinary Sciences (CSIR-NIIST), Thiruvananthapuram, Kerala 695019, India

Published online: 03 August 2018

Sustainable Energy & Fuels

PAPER

View Article Online
View Journal | View Issue

Cite this: *Sustainable Energy Fuels*, 2018, **2**, 2244

One-pot synthesis of g-C_3N_4/MnO_2 and g-C_3N_4/SnO_2 hybrid nanocomposites for supercapacitor applications

Jithesh Kavil,[a] P. M. Anjana,[b] Pradeepan Periyat*[a] and R. B. Rakhi *[b]

Received 14th June 2018
Accepted 27th July 2018

DOI: 10.1039/c8se00279g

rsc.li/sustainable-energy

Carbon materials with layered structures with their unique surface area and charge transport properties have been attracting significant attention as electrode materials in renewable energy storage devices. The rapid agglomeration of layered materials during electrochemical processes reduces their shelf life and specific capacitance, which can be prevented by the introduction of suitable spacers between the layers. Herein, we report the electrochemical performance of MnO_2 and SnO_2 metal oxide spacers incorporated layered graphitic carbon nitride g-C_3N_4 in a symmetric two electrode configuration. The as-prepared g-C_3N_4/MnO_2 and g-C_3N_4/SnO_2 hybrid nanocomposites act as efficient electrode materials for symmetric supercapacitors. The performance of the electrode materials is compared with that of bare g-C_3N_4. A remarkable increase in specific capacitance was obtained for the g-C_3N_4/MnO_2 composite electrode (174 F g^{-1}) when compared to the bare g-C_3N_4 electrode (50 F g^{-1}) and g-C_3N_4/SnO_2 electrode (64 F g^{-1}). At a constant power density of 1 kW kg^{-1} the symmetric supercapacitors based on g-C_3N_4, g-C_3N_4/SnO_2, and g-C_3N_4/MnO_2 electrodes exhibited energy densities of 6.9, 8.8 and 24.1 W h kg^{-1} respectively.

1. Introduction

The storage of renewable energy and its release upon demand has been a significant technological matter of contention in recent years.[1,2] Lithium-ion (Li-ion) batteries have been successful for the storage of renewable energy with high energy density.[3,4] However, next generation hybrid vehicles, regenerative braking systems, and high power electronic devices demand high power density, large cycle life, and remarkably high safety and low cost. Supercapacitors have been widely employed as an alternative or in support of Li-ion batteries to address these demands.[5,6] Supercapacitors possess much higher power density, excellent cycle stability, a wide temperature range of performance, intrinsically safe charge storage mechanism and they can be charged and discharged in seconds.[7,8] Supercapacitors store charges either non-faradaically (EDLC capacitors) or faradaically (pseudocapacitors).[9]

Nanocarbon materials such as activated carbon, carbon nanotubes, reduced graphene oxide and graphene oxide are widely used as electrode materials in EDLCs due to their high surface area and electronic conductivity.[10] Nitrogen or sulphur doping in carbon-based materials is usually carried out to increase the wettability of the electrode surface with the electrolyte.[11,12] However, nonmetal doping creates chemical inhomogeneity and thereby reduces the shelf life of the electrode material.

Graphitic carbon nitride g-C_3N_4 has emerged as an alternative for purely carbon-based EDLC electrode materials owing to its low cost, chemical and mechanical stability and intrinsically high nitrogen content.[13] The lone pair of electrons present in the N atom of the ring structure of g-C_3N_4 induces more polarity in the molecule and enhances the wettability and the charge carrier mobility of the material.[14]

Bulk g-C_3N_4 exhibits a very low EDLC specific capacitance of 71 F g^{-1} and 81 F g^{-1} at a current density of 0.5 A g^{-1} and 0.2 A g^{-1} respectively due to its inherently low specific surface area and conductivity.[15] Reports suggest that the electrochemical properties of bulk g-C_3N_4 can be enhanced dramatically by the incorporation of pseudocapacitive phases into the matrix of bare g-C_3N_4 which will facilitate the charge transport by a synergistic effect between faradaic and non-faradaic processes of electron transport.[13,14]

Transition metal oxides (TMOs) such as, RuO_2, MnO_2, V_2O_5, TiO_2, SnO_2 *etc.* and Prussian blue (PB) are widely used as pseudocapacitive electrode materials. An ultralong V_2O_5@-conducting polypyrrole composite exhibited enhanced supercapacitor performance along with superior rate capability and improved cycling stability.[16] A challenging fabrication technique was reported on the synthesis of PB and its analogues

[a]*Department of Chemistry, University of Calicut, Kerala, India-673635. E-mail: rakhiraghavanbaby@niist.res.in*

[b]*Chemical Sciences and Technology Division, CSIR-National Institute of Interdisciplinary Sciences (CSIR-NIIST), Thiruvananthapuram, 695019, Kerala, India. E-mail: pperiyat@uoc.ac.in*

Applied Surface Science 487 (2019) 109–115

Contents lists available at ScienceDirect

Applied Surface Science

journal homepage: www.elsevier.com/locate/apsusc

Full length article

Multifunctional nanohybrid material from discarded razor blades as cost-effective supercapacitor electrodes and oil-spill cleaners

Jithesh Kavil[a], P.M. Anjana[b], C.P. Roshni[c], Pradeepan Periyat[a], K. Govind Raj[c,*], R.B. Rakhi[b,*]

[a] Department of Chemistry, University of Calicut, Kerala 673635, India
[b] Chemical Sciences and Technology Division, CSIR-National Institute of Interdisciplinary Sciences (CSIR-NIIST), Thiruvananthapuram, Kerala 695019, India
[c] Department of Chemistry, Malabar Christian College, Calicut, Kerala 673635, India

ARTICLE INFO

Keywords:
Fe_2O_3@carbon core-shell
Supercapacitor
Specific capacitance
Energy density
Oil-spill removal

ABSTRACT

Fe_2O_3@carbon core-shell nanoparticles were prepared via hydrothermal carbonization method by using discarded razor blade and glucose solution as precursors. The material was employed as electrode in symmetric supercapacitor device. At a constant current density of 1 A g^{-1}; the Fe_2O_3@carbon samples exhibit a highest specific capacitance of 285.6 F g^{-1} which is almost two-fold the specific capacitance of the as-synthesized Iron oxide sample (122.7 F g^{-1}). At a constant power density of 1 kW kg^{-1}, Iron oxide and Fe_2O_3@carbon samples have the energy density values of 22.52 Wh kg^{-1} and 37.88 Wh kg^{-1}, respectively. The Fe_2O_3@carbon sample has also been applied for the removal of oil from an artificial oil spill. One gram of the material is capable of the instantaneous removal of 5 g of oil from the spillage with the assistance of an external magnet.

1. Introduction

The industrialization and the population explosion have to lead to an unparallel explosion and diversity in the generation of waste materials. The waste management demands an immediate and scientific approach for socio-economic development and environmental protection. The concept of "closed economy production model" or regenerative economy contemplates the garbages as the resource that promotes a novel and sustainable developmental strategy by minimizing the landfills [1]. Closed economy minimizes the environmental pollution and depletion of resources by reducing, reusing and recycling of the waste material. Clean energy technology and a clean environment are inevitable for the sustainable development of society [2]. Since last few decades, the researchers and policymakers have been searching for functional materials that can be used for the renewable energy conversion, storage and simultaneously for environmental remediation.

In recent years, supercapacitors have been received increasing interest in energy storage technology owing to its superior electrochemical properties than the conventional batteries [3,4]. As evidenced from the 'Ragon-plot' supercapacitors provide much higher power density than conventional batteries and energy density than dielectric capacitors. Supercapacitor technology has been explored tremendously as an environmentally benign energy resource in recent years surely due to the development of a wide range of nanostructured materials from researchers all over the world [5]. Recently attempts were reported to fabricate supercapacitor electrodes from waste materials as a green approach to attain the global goal of sustainable development. Garbages such as tires, biomass, plastic wastes were used as the prospective source of activated carbon for supercapacitor applications [6–9]. However, to the best our knowledge, there are no reports for the fabrication of nanosemiconductor hybrid materials from discarded materials with multifunctional utility in energy storage and environmental applications.

The contamination of water by different chemical substances is one of the lethal issues faced around the globe. Among the various contaminants, oil spills generated from damaged pipelines, tankers, and rigs are considered as the one of the worst environmental concern caused by human activity. Oil spills are known to cause severe long-term damages to the aquatic environment by which the entire aquatic ecosystem gets destabilized [10]. The conventional methods for the clean-up process such as skimming, hot water spraying and burning cause damage to the aquatic organisms. Due to the simplicity in application, the organophilic sorbent materials like organic polymers, zeolites, and graphenes have received considerable attention recently. To make the process viable, large quantities of oil have to be removed from the spillage quite instantaneously using a low-cost sorbent. The most common strategy is to employ magnetic adsorbents which can instantaneously remove oil from spills utilizing the hydrophobic interactions with oil molecules followed by magnetic separation [11].

* Corresponding authors.
E-mail addresses: govind@mccclt.ac.in (K.G. Raj), rakhiraghavanbaby@niist.res.in (R.B. Rakhi).

https://doi.org/10.1016/j.apsusc.2019.05.055
Received 28 January 2019; Received in revised form 22 April 2019; Accepted 6 May 2019
Available online 07 May 2019
0169-4332/

Nano-Structures & Nano-Objects 16 (2018) 24–30

Contents lists available at ScienceDirect

Nano-Structures & Nano-Objects

journal homepage: www.elsevier.com/locate/nanoso

CdS sensitized TiO_2 nano heterostructures as sunlight driven photocatalyst

Jithesh Kavil [a], Ahmed Alshahrie [b], Pradeepan Periyat [a,*]

[a] Department of Chemistry, University of Calicut, Kerala, 673635, India
[b] Centre of Nanotechnology, King Abdul Aziz University, Jeddah, 21589, Saudi Arabia

GRAPHICAL ABSTRACT

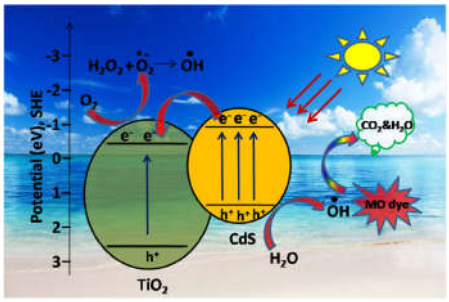

ARTICLE INFO

Article history:
Received 10 January 2018
Received in revised form 12 March 2018
Accepted 27 March 2018

Keywords:
Photocatalyst
Nano heterostructure
Nanomaterials
CdS
TiO_2

ABSTRACT

Sunlight harvesting nano heterostructure materials with excellent photocatalytic activity has received considerable attention in recent years. Here we meticulously investigated the effect of CdS nano crystal loading on the light absorption capacity and the photocatalytic activity of TiO_2 nanomaterials by assembling TiO_2-CdS heterostructures. A distinct heterostructure was established in the presently reported hybrid system with 10 wt% CdS incorporation into TiO_2 and the photocatalytic study showed that TiO_2-CdS10 has 3.5 times higher catalytic activity than bare TiO_2. This superior photocatalytic performance is attributed to the excellent light absorption, high surface area and the slow rate of recombination of photogenerated charge carriers of TiO_2-CdS10 hetero structures. A mechanism was also proposed for the CdS sensitized sunlight driven photocatalytic degradation of methyl orange dye in presence of CdS–TiO_2 nano heterostructure.

1. Introduction

TiO_2 based heterogeneous catalysis becomes an efficient technique for the photocatalytic oxidative removal of dissolved organic and inorganic contaminants in water due to its cost effectiveness, and the distinctive photocatalytic activity [1–4]. It is the bandgap energy of TiO_2 (3.2 eV) that limits its application as solar harvesting photocatalyst [5,6]. Visible light response of TiO_2 has been modified by various approaches such as metal and nonmetal doping in an attempt to tailor the band gap [7,8], photosensitization by anchoring organic chromospheres [9] etc. In recent years heterojunction photocatalyst fabrication *via* hybridizing TiO_2 with suitable narrow band gap semiconductors such as CdS, Cu_2O, ZnO, *etc.* had received considerable attention among the scientific community due to its excellent light absorption ability, improved photocatalysis and also photo stability [10–12].

* Corresponding author.
E-mail address: pperiyat@uoc.ac.in (P. Periyat).

https://doi.org/10.1016/j.nanoso.2018.03.011
2352-507X/

Nano-Structures & Nano-Objects 18 (2019) 100317

Contents lists available at ScienceDirect

Nano-Structures & Nano-Objects

journal homepage: www.elsevier.com/locate/nanoso

Development of 2D nano heterostructures based on g-C_3N_4 and flower shaped MoS_2 as electrode in symmetric supercapacitor device

Jithesh Kavil [a,1], Shabeeba Pilathottathil [b,1], Mohamed Shahin Thayyil [b], Pradeepan Periyat [a,*]

[a] Department of Chemistry, University of Calicut, Kerala, 673635, Inida
[b] Department of Physics, University of Calicut, Kerala, 673635, Inida

GRAPHICAL ABSTRACT

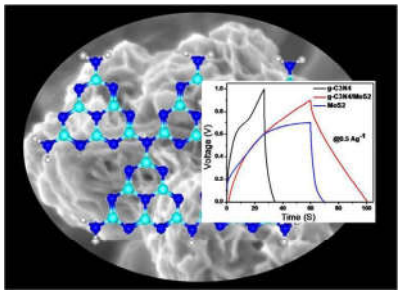

ARTICLE INFO

Article history:
Received 6 September 2018
Received in revised form 12 March 2019
Accepted 21 April 2019

ABSTRACT

g-C_3N_4 with plenty of lone pair electrons on the two dimensional (2D) lamellar structures have attracted remarkable attention as an electrical double layer (EDLC) supercapacitor electrodes due to their surface polarity and wettability with electrolyte molecule. However, the agglomeration of the exfoliated g-C_3N_4 sheets during the electrochemical process curtails their accessible electroactive surface area so that specific capacitance get reduces considerably. Here in for the first time in the literature, we report a 2D nanohybrid structure of g-C_3N_4/MoS_2 having attractive electrochemical properties than bare g-C_3N_4 and MoS_2, owing to the wonderful flower shaped morphology of the synthesized pseudocapacitive semiconducting MoS_2 phase which acts as spacers in between the layers of g-C_3N_4. The specific capacitance of bare g-C_3N_4 and $MoS_2$is 10 Fg^{-1} and 14 Fg^{-1} respectively however hybrid material g-C_3N_4/MoS_2 exhibits a specific capacitance value of 45.5 Fg^{-1}. This remarkable hike in specific capacitance can be attributed to the synergistic effect of both faradaic and non-faradaic process of energy storage.

1. Introduction

As the demand for renewable energy sources for fulfilling the future energy needs of the world is urgently on the rise, the energy storage has been a bottleneck in the renewable energy market and there is a global search for technically viable energy storage devices. Although Lithium-ion batteries have been used as an excellent energy storage device it is unsuitable for catering the huge power needs of modern electronic devices and hybrid vehicles [1,2]. The development of novel materials with high energy density as batteries and power densities as supercapacitors is the present-day challenge among the scientific

* Corresponding author.
E-mail address: pperiyat@uoc.ac.in (P. Periyat).
[1] These authors have contributed equally.

https://doi.org/10.1016/j.nanoso.2019.100317
2352-507X/

Solar Energy 158 (2017) 792–796

Contents lists available at ScienceDirect

Solar Energy

journal homepage: www.elsevier.com/locate/solener

Polyaniline as Photocatalytic Promoter in Black Anatase TiO_2

Jithesh Kavil[a], Sanjay Gopal Ullattil[b], Ahmed Alshahrie[c], Pradeepan Periyat[a,*]

[a] Department of Chemistry, University of Calicut, Kerala 673635, India
[b] Department of Nanoscience & Technology, University of Calicut, Kerala 673635, India
[c] Centre of Nanotechnology, King Abdul Aziz University, Jeddah 21589, Saudi Arabia

ARTICLE INFO

Keywords:
Photocatalyst
Heterojunction
PANI
Black TiO_2

ABSTRACT

The effect of conducting polymer matrix, polyaniline (PANI) on the photocorrosion and photochemical activities of Black Anatase Titania (BAT) has been systematically investigated. PANI-BAT composite has been fabricated by a modified hydrothermal method and successive *in situ* polymerization of aniline. This hybrid material has shown excellent photo catalytic activity than BAT under visible light. The rate constant value of dye degradation in presence of the PANI-BAT composite was found 2.4×10^{-2} min^{-1}, which is 1.5 times greater than that of the commercially available photocatalyst Degussa P25 and BAT. The study unveils the strong correlation between electrochemical impedance measurements and the photochemical results.

1. Introduction

Coloured semiconductors with defective structure have been pioneered as a promising material for enhanced solar absorption, photoactivity and hydrogen generation owing to its narrow band gap energy (Chen et al., 2011; Zheng et al., 2015a, 2015b; Zhu et al., 2014; Qiu et al., 2014). Recently TiO_{2-x} nanoparticles with black colour that are capable of absorbing IR radiation in addition to UV and Visible radiation have attracted the energy and environmental scientists to develop such material with crowning properties for various applications (Chen et al., 2011; Ullattil and Periyat, 2017; Zheng et al., 2015a, 2015b; Wang et al., 2016). A defective black material arises due to destruction in the periodicity of the lattice. These imperfections are formed due to the band tailing created by oxygen vacancies (Vo) and surface hydrogenation. Such defects are also responsible for the narrowed band gap energy in TiO_{2-x} (Chen et al., 2015; Qingli et al., 2015). However, the higher probability of photo excited electron-hole recombination is an innate shortcoming of tapered band gap semiconductors that limits their practical utilization. Attempts have been made to overcome this photocorrosion effect in wide band gap semiconductors using various methods such as metal doping, non-metal doping (Khan and Berk, 2014; Pelaez et al., 2012; Asahi et al., 2001; Chen and Burda, 2008), heterojunction catalysis based on narrow band gap semiconductors (Kalithasan et al., 2017; Suyana et al., 2016; Bessekhouad et al., 2005) and π conjugated conducting polymer matrices (Ghosh et al., 2015; Zhang and Wan, 2003). Among the conducting polymers poly aniline (PANI) is a popular candidate because of its easy fabrication, cost effectiveness and environmental stability (Syed and Dinesan, 1991) besides its excellent charge transport properties along with the p-type semiconducting nature (Shirota and Kageyama, 2007; Min et al., 2007; Chen et al., 2016; Zhang et al., 2008). Herein for the first time we report the polyaniline black TiO_2 (PANI-BAT) composite with improved photoactivity than black TiO_2 and Degussa P25. The electrochemical characteristics of the materials were determined in order to analyze the electron transport properties and these results were in correct agreement with the photocatalytic performance of the PANI-BAT nano composite.

2. Experimental

2.1. Preparation of black TiO_2 (BAT)

Black anatase titania (BAT) nanoparticles were synthesized by a modified hydrothermal method using titanium tertiary butoxide (Sigma Aldrich), 2-propanol (Merck) and manganese acetate (Merck) as the only precursors (Ullattil and Periyat, 2015). In a typical experiment 0.2 M Titania precursor was dissolved in 2-propanol with continuous stirring. 0.02 M solution of manganese acetate in 50 ml hydrogen peroxide was added dropwise to the above solution for simultaneous doping and hydrolysis. Stirring was continued for another 2 h and the solution was transferred to 100 ml stainless steel autoclave and kept at a temperature of 160 °C for 24 h. The grey colored sol so obtained was calcined at 250 °C for 1 h and the resulting black TiO_2 nanoparticles were washed with ethyl alcohol and acetone.

* Corresponding author.
E-mail address: pperiyat@uoc.ac.in (P. Periyat).

http://dx.doi.org/10.1016/j.solener.2017.10.049
Received 15 July 2017; Received in revised form 10 October 2017; Accepted 13 October 2017

Solar Energy 155 (2017) 490–495

Contents lists available at ScienceDirect

Solar Energy

journal homepage: www.elsevier.com/locate/solener

A Sol-solvothermal Processed 'Black TiO_2' as Photoanode Material in Dye Sensitized Solar Cells

Sanjay Gopal Ullattil [a], Aiswarya Vijayakumar Thelappurath [a,b], Sriman Narayana Tadka [b], Jithesh Kavil [a], Baiju Kizhakkekilikoodayil Vijayan [b,c], Pradeepan Periyat [a,d,*]

[a] Department of Chemistry, University of Calicut, Kerala 673 635, India
[b] Centre for Materials for Electronics and Technology, Thrissur, Kerala, India
[c] Department of Nanoscience, Kannur University, Kerala, India
[d] Department of Chemistry, Central University of Kerala, Kasaragod, 671314, India

ARTICLE INFO

Article history:
Received 18 March 2017
Received in revised form 17 May 2017
Accepted 24 June 2017

Keywords:
Black TiO_2
Sol-solvothermal strategy
NIR absorption
Photoanode
DSSC
EIS

ABSTRACT

A sol-solvothermal synthetic strategy has been designed and executed for the preparation of black TiO_2 nanoparticles and has been implemented as photoanode in dye sensitized solar cell (DSSC) for the first time. As synthesized yellow anatase titania (YAT) possessed visible light absorption and the black anatase titania (BAT) exhibited a longer wavelength absorption even at the IR region of the solar spectrum. These visible light absorbing YAT and the IR absorbing BAT nanoparticles have been employed as photoanode in dye sensitized solar cell (DSSC) and performance have been compared with DSSC fabricated using commercially available titania, P25. Distinctly, the efficiency of the IR absorbing black anatase TiO_2 has been found 50% greater than the yellow anatase TiO_2 (YAT) and 79% greater than the commercially available P25.

1. Introduction

One of the most investigated material TiO_2 has made wonders in wide variety of applications such as in photocatalysis (Schneider et al., 2014), self-cleaning devices (Banerjee et al., 2015), electrochromic displays (Periyat et al., 2010), supercapacitors (Kim et al., 2013) and in dye sensitized solar cells (Ullattil and Periyat, 2017). Among these striking applications of TiO_2, as a photoanode in DSSC have found impetus in enhancing the solar to electrical energy conversion by utilizing the solar energy (Mohamed and Rohani, 2011). The solar spectrum consists of 5% of UV (200–400 nm), 43% of visible light (400–700 nm) and 52% of IR (700–2500 nm) energy (Ullattil and Periyat, 2015). Due to the wide band gap energy of anatase TiO_2 (3.2 eV) the utilization of solar spectrum has limited to the UV region wavelength (≤388 nm) Periyat et al., 2016. Thus extending its absorption cut-off and thereby inducing maximum absorption have been introduced by metal doping and non-metal doping (Daghrir et al., 2013; Chen and Burda, 2008). However, still the visible light absorption has only been achieved and the higher wavelength absorption *viz* the IR absorption remained as a challenge to the contemporary science.

Nowadays colored materials have got supreme importance in the area of light harvesting (Tan et al., 2014). If a materials is colored it can obviously absorb energy from the visible region of the solar spectrum. In this way yellow (Sakthivel et al., 2004), blue (Qiu et al., 2014) and red (Liu et al., 2012). TiO_2 materials have been synthesized and were found highly light responsive for harvesting the visible light energy. A black colored material can utilize maximum solar energy since its absorption onset lies in the IR region. As we all know TiO_2 is the most investigated materials because of its tremendous photoactivity, the discovery of black TiO_2 by Chen et al. led the researchers towards facile strategies for the synthesis of black TiO_2 nanomaterial that can culminate the maximum efficiency as a sunlight harvester (Chen et al., 2011). To date, black TiO_2 nanostructures with wide area absorption have been synthesized by hydrogenation (Leshuk et al., 1892), pulsed laser ablation (Chen et al., 2015), sol-microwave treatment (Ullattil and Periyat, 2015), one pot gel combustion (Ullattil and Periyat, 2016), etc. and have been used in photocatalysis (Xin et al., 2015), self-cleaning (Kim et al., 2016), Li ion batteries (Eom et al., 2015), super capacitors (Zhi et al., 2016) and in photothermal therapy (Ren et al., 2015). Among the two synthetic strategies one pot gel combustion (Ullattil and Periyat, 2016) and sol-microwave treatment

* Corresponding author at: Department of Chemistry, Central University of Kerala, Kasaragod 671314, India.
E-mail addresses: pperiyat@uoc.ac.in, pperiyat@cukerala.ac.in (P. Periyat).

http://dx.doi.org/10.1016/j.solener.2017.06.059
0038-092X/

ACS Sustainable Chemistry & Engineering

Research Article

Cite This: ACS Sustainable Chem. Eng. 2018, 6, 5401−5412

pubs.acs.org/journal/ascecg

Ti^{3+} Induced Brown TiO_2 Nanotubes for High Performance Sodium-Ion Hybrid Capacitors

Binson Babu,[†,∥] Sanjay Gopal Ullattil,[‡,∥,§] Ranjith Prasannachandran,[†] Jithesh Kavil,[‡] Pradeepan Periyat,*[,‡] and Manikoth M. Shaijumon*[,†]

[†]School of Physics, Indian Institute of Science Education and Research Thiruvananthapuram, Maruthamala PO, Vithura, Thiruvananthapuram, Kerala 695551, India

[‡]Department of Chemistry, University of Calicut, Thenhipalam, Kerala 673635, India

Supporting Information

ABSTRACT: Sodium-ion hybrid capacitors are attracting great attention and are emerging as promising energy storage devices, with their remarkable footsteps in energy and power densities. However, the development of efficient electrode materials that result in a minimum trade-off between their energy and power densities, and that allow long-term cycling stability, still remains a challenge for realizing their full potential as an alternate energy storage system for commercial applications. Herein, for the first time, we study the sodium-ion intercalation pseudocapacitance behavior of brown TiO_2 nanotubes for their application as an efficient anode material for Na-ion hybrid capacitors. We synthesized semicrystalline and crystalline anatase brown TiO_2 nanotubes, aggregated in a flowerlike morphology, through a hydrothermal route, and performed detailed electrochemical studies. The kinetic studies reveal that semicrystalline brown TiO_2 exhibits a Na-ion intercalation pseudocapacitive behavior with 57% of capacitive storage at 1.0 mV s^{-1}, whereas crystalline brown TiO_2 is more faradaic in nature. Further, hybrid Na-ion capacitors are fabricated with brown TiO_2 materials as an anode and activated carbon as a cathode, and the fabricated device showed an excellent electrochemical performance with a high energy density of ∼68 Wh kg^{-1} and a high power density of ∼12.5 kW kg^{-1} and with a good cycling stability up to 10 000 cycles with ∼80% capacitive retention. The obtained results represent a promising approach toward developing efficient electrodes for hybrid Na-ion capacitors.

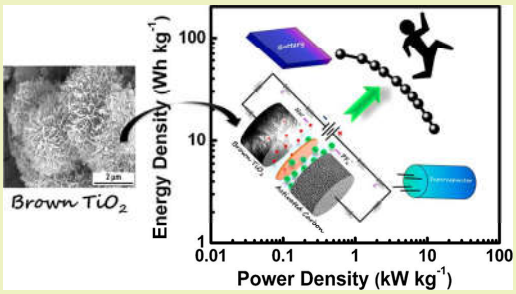

KEYWORDS: *Energy storage, Semicrystalline brown TiO_2 nanotubes, Pseudocapacitance, Hybrid sodium-ion capacitor*

INTRODUCTION

Energy is one of the biggest challenges of this century, and with the development of renewable energy sources, tremendous efforts are being devoted to design efficient energy storage systems. Electrochemical storage of energy by using batteries and supercapacitors is a mature technology; however, this approach still needs improvement in terms of energy and power densities and long-term cycling stability.[1−3] The concept of hybrid Li/Na-ion capacitors that combine the virtue of faradaic and double layer processes is quite promising and results in an improved electrochemical performance in terms of both energy and power densities. Amatucci et al.[4] integrated the high surface area carbonaceous material as a cathode and the crystalline Li-intercalating material as an anode in a Li-based nonaqueous electrolyte. Here the cathode provides a high power density by virtue of the double layer capacitive behavior, while the intercalation behavior of the anode results in a higher energy density. Such a hybrid energy storage device achieves a higher energy density than a supercapacitor and achieves a higher power density than a lithium-ion battery (LIB), thus placing it at the upper right position in the Ragone plot.[5−7]

With the ongoing thrust on sodium chemistry, owing to their huge abundance over lithium and similar electrochemical property with that of lithium,[8−10] the hybrid ion capacitor based on a Na-ion intercalation/redox anode electrode with a double layer capacitive cathode is gaining increasing interest among the energy storage research community.[11−16] Several sodium-based oxide materials have been initially studied for a Na-ion battery, expecting a direct translation of lithium chemistry. However, developing efficient sodium storage materials for the development of high performance Na-ion capacitor systems still remains a challenge. Though hard carbonaceous materials are reported to be a decent anode candidate, its random structure inhibits the Na-insertion capacity at high rates.[17] Several conversions as well as alloying electrodes, for example, tin- and antimony-based materials, have

Received: January 16, 2018
Published: February 17, 2018

DOI: 10.1021/acssuschemeng.8b00236
ACS Sustainable Chem. Eng. 2018, 6, 5401−5412